ARMY RESEARCH LABORATORY

Interface Defeat of Long-Rod Projectiles by Ceramic Armor

by George E. Hauver, Edward J. Rapacki, Jr., Paul H. Netherwood, and Ralph F. Benck

ARL-TR-3590 **September 2005**

NOTICES

Disclaimers

The findings in this report are not to be construed as an official Department of the Army position unless so designated by other authorized documents.

Citation of manufacturer's or trade names does not constitute an official endorsement or approval of the use thereof.

Destroy this report when it is no longer needed. Do not return it to the originator.

Army Research Laboratory
Aberdeen Proving Ground, MD 21005-5066

ARL-TR-3590 **September 2005**

Interface Defeat of Long-Rod Projectiles by Ceramic Armor

George E. Hauver, Edward J. Rapacki, Jr., Paul H. Netherwood, and Ralph F. Benck
Weapons and Materials Research Directorate, ARL

REPORT DOCUMENTATION PAGE

Form Approved
OMB No. 0704-0188

1. REPORT DATE *(DD-MM-YYYY)*	2. REPORT TYPE	3. DATES COVERED (From - To)
September 2005	Final	October 1985–September 2004

4. TITLE AND SUBTITLE
Interface Defeat of Long-Rod Projectiles by Ceramic Armor

5a. CONTRACT NUMBER

5b. GRANT NUMBER

5c. PROGRAM ELEMENT NUMBER

6. AUTHOR(S)
George E. Hauver, Edward J. Rapacki, Jr., Paul Netherwood, and Ralph Benck

5d. PROJECT NUMBER
611102H4311

5e. TASK NUMBER

5f. WORK UNIT NUMBER

7. PERFORMING ORGANIZATION NAME(S) AND ADDRESS(ES)
U.S. Army Research Laboratory
ATTN: AMSRD-ARL-WM-TD
Aberdeen Proving Ground, MD 21005-5066

8. PERFORMING ORGANIZATION REPORT NUMBER
ARL-TR-3590

9. SPONSORING/MONITORING AGENCY NAME(S) AND ADDRESS(ES)

10. SPONSOR/MONITOR'S ACRONYM(S)

11. SPONSOR/MONITOR'S REPORT NUMBER(S)

12. DISTRIBUTION/AVAILABILITY STATEMENT
Approved for public release; distribution is unlimited.

13. SUPPLEMENTARY NOTES

14. ABSTRACT
An investigation has been conducted to guide the development of ceramic armor that protects against long-rod projectiles launched at ballistic-ordnance velocities. Studies have concentrated on protection by diverting the projectile, but have also considered protection by maintaining a high resistance to penetration. A projectile is diverted by promoting a lateral flow of projectile erosion products at the ceramic, which minimizes stress and microdamage in the impinged area of the ceramic. Some resistance to lateral flow provides dynamic frontal support for the ceramic, and the projectile is fully consumed by lateral flow even though marginal rear support permits moderate macrodamage. The first part of the investigation has examined ceramic damage and the influences of materials, dimensions, target designs, and other factors, such as impact velocity and target obliquity. The second part of the investigation has briefly considered layered target designs that achieve protection by maintaining the ceramic element's high resistance to penetration. The interplay of material properties and characteristics and target designs must be further investigated to determine the potential for future ballistic armor designs.

15. SUBJECT TERMS
ceramic armor, long-rod projectiles, ceramic damage, damage suppression

16. SECURITY CLASSIFICATION OF:			17. LIMITATION OF ABSTRACT	18. NUMBER OF PAGES	19a. NAME OF RESPONSIBLE PERSON
a. REPORT	b. ABSTRACT	c. THIS PAGE			Edward J. Rapacki, Jr.
UNCLASSIFIED	UNCLASSIFIED	UNCLASSIFIED	UL	98	19b. TELEPHONE NUMBER (*Include area code*) (410) 306-0801

Contents

List of Figures

Acknowledgments

The second author acknowledges the very strong technical contributions and long time mentorship and friendship of the co-authors: Messrs. George Hauver, Paul Netherwood, and Ralph Benck. Sadly Mr. Benck passed away on 16 November 2002. Their keen observational and analytical capabilities were the key to identifying the unique phenomenon known as ceramic interface defeat. The technical efforts of Angelo Melani, Michael Blount, and C. Austin Standiford are also gratefully acknowledged. Their test article fabrication and experimental conduct skills were critical to these efforts. Technical discussions with other scientists, engineers, and technical support staff, too numerous to list here explicitly, were also beneficial as the work evolved. Lastly, the support and encouragement of the management and leadership of the U.S. Army Ballistic Research laboratory, and subsequently the U.S. Army Research Laboratory, are gratefully acknowledged.

1. Introduction

Structural ceramics, with high compressive strengths and low densities, have been considered promising candidates for armor to defeat long-rod kinetic-energy projectiles. However, most experimental ceramic armors have not approached their full potential for ballistic protection because damage occurs ahead of the attacking projectile. Damaged ceramic is displaced, reducing the resistance to penetration. This investigation has demonstrated that the ability of a ceramic to resist penetration can be improved by addressing three factors: (1) characteristics of the attack, (2) dynamic response of the ceramic, and (3) characteristics of the system components that protect and support the ceramic. By considering these factors, it has been possible to prevent penetration into ceramics attacked by high-density, long-rod projectiles launched at 1600 m/s and somewhat higher velocities.

Initial experiments in the investigation were conducted by a reverse-ballistic procedure in which a small ceramic target with steel confinement was launched against a long, stationary rod of tungsten (W) heavy alloy (WHA). The long rod was observed by flash radiography as it interacted with the confined ceramic target at normal incidence. Measurements and observations indicated that a ceramic had no specific resistance to penetration. By modifying the target system, a ceramic could be penetrated immediately, or only after an initial delay, which was referred to as "dwell." With some ceramics, the duration of dwell could be extended to produce total defeat of the long rod with no penetration into the ceramic. This highly resistant mode of behavior was referred to as "interface defeat" (Hauver and Melani, 1988; Hauver et al., 1993, 1994), and it was attributed to accumulating erosion products from the long-rod projectile which compressed and supported the ceramic, minimizing damage and preventing the displacement of damaged ceramic. This dynamic control of ceramic damage was considered promising, but small-scale studies were discontinued because of concern that interface defeat at a ceramic might be possible only at a small scale. Later, this concern about scale was found to be unjustified.

Subsequent studies were conducted by the conventional forward ballistic impact procedure in which a stationary ceramic target is attacked at normal incidence by a long-rod projectile. Conventional experiments permitted the use of larger projectiles, larger targets, and higher projectile velocities. Initially, larger targets achieved only a delay in the onset of penetration, as previously observed in early experiments with smaller-scale targets. However, when all critical features of the small targets were identified and scaled correctly, interface defeat was also achieved at larger scale. Interface defeat in larger ceramic targets with heavy steel confinement could not be observed by flash radiography, so the investigation depended on examinations of recovered target components. Recovered ceramic was sectioned to expose the interior damage which consisted of distributed macrocracking and a small volume of microdamage caused by shear stress under the impingement area. Ceramics were ranked according to damage and the

flow pattern of erosion products at their front surface. It was evident that the displacement of microdamaged ceramic located under the impingement area, and/or macrodamaged ceramic immediately surrounding the impingement area, could misdirect the lateral flow of eroded projectile material. Severely misdirected flow impeded the lateral movement of erosion products and caused increased stress in the impingement area. Higher stress aided the displacement of microdamaged ceramic and could cause an abrupt transition from lateral flow at the interface to penetration of the ceramic.

The investigation of ceramic targets with heavy steel confinement was discontinued because the heavy-target configuration was impractical for armor, and there was concern that the information it provided about interface defeat might not be relevant to practical ceramic-armor configurations. With heavy targets, the emphasis was on complete suppression of penetration. For more practical configurations, ceramic support must be reduced for significant weight reduction, and the investigation must emphasize control of ceramic damage rather than complete suppression of damage. It became apparent that flash-radiographic observations were necessary to provide time-resolved information about the internal flow of erosion products and its relationship to the increased level of damage.

Ceramic targets with aluminum (Al) alloy confinement were introduced briefly to confirm the benefit of radiography. These initial flash-radiographic observations provided valuable insight into the influence of damage, but the low strength of Al-alloy severely limited the time duration of relevant flow behavior. The introduction of titanium (Ti) alloy confinement provided the strength necessary to support a ceramic during full-term interface defeat, and this permitted flash-radiographic observations of behavior during attacks at both normal and oblique incidence. Flash radiography confirmed that interface flow is related to the stability of damaged ceramic, and that interface defeat depends on characteristics of the projectile, the attack, the ceramic, and the supporting system.

The investigation confirmed the importance of minimizing stress within the impingement area and controlling stress outside of the impingement area. Minimum stress within the impingement area aids in maintaining the stability of microdamaged ceramic. Controlled stress outside of the impingement area contributes to deformation of the weakened supporting structure and damages the ceramic, but it simultaneously aids the projectile defeat process by providing dynamic support for the damaged ceramic. The next objective is to optimize the system, reducing the target weight closer to the failure threshold. An attack at normal incidence presents the greatest challenge because microdamage under the impingement area is a maximum. Defending against oblique attack is less demanding because microdamage diminishes as the normal component of velocity decreases with obliquity. In effect, higher obliquity should tend to compensate for a higher attack velocity, and ballistic protection should benefit from mounting ceramic armor panels with an orientation that increases the probability of an oblique attack.

The following sections of the report describe different phases of the investigation. The primary theme of the report is that ballistic performance depends on damage to the ceramic, and that improved performance is achieved by the suppression or control of damage. The secondary theme of the report is that real-time, flash-radiographic observations provide information which is critical for the correct interpretation of dynamic behavior. It is difficult to infer dynamic behavior reliably by only an examination of recovered target components, and the difficulty increases with elevated damage levels of more practical ceramic-armor configurations. From the beginning of the investigation, the goal has been the effective use of ceramics for practical armor to protect against long-rod threats. This goal has not yet been fully attained, but the studies have contributed insight and solutions in major problem areas.

2. Small-Scale Reverse-Ballistic Experiments

2.1 Procedure for Reverse-Ballistic Experiments

Reverse-ballistic experiments at normal incidence were conducted by supporting a small ceramic target in a plastic sabot that was launched from a light-gas gun. The target impacted a long, stationary WHA rod that was supported by fine wire threads and axially aligned in front of the gun muzzle. In the earliest experiments, two 450-kV flash x-ray pulsers provided orthogonal radiographs at selected times during penetration. Megavolt pulsers, containing demountable x-ray tubes with 2-mm-diameter anodes, were introduced later for greater resolution of detail. A tungsten wire fiducial in the moving target and an evaluation of magnification factors permitted measurement of penetration depth. Reverse ballistics offered nearly perfect alignment of the small, long-rod projectiles that were considered difficult to launch by conventional means. A major disadvantage of reverse ballistics was the target launch mass, which, with steel confinement, limited the maximum impact velocity to ~1450 m/s.

Different projectile and target configurations were used to provide specific data and observations. The primary projectile was a blunt-nose rod of WHA composed of 90W-7Ni-3Fe. These rods were machined from full-scale projectiles, 33 mm in diameter, that had been swaged to reduce their cross-sectional area by 24%. The rods were 1.58 mm in diameter, and had length-to-diameter (L/D) ratios between 15 and 40. Targets had mild steel side confinement, which had a hardness of 220 BHN. This confinement initially had a 25.4 mm × 25.4 mm cross section, but corners were rounded to reduce the launch mass, leaving four 13.4-mm-wide faces through which the interior was observed by flash radiography. The confinement was machined to accept a target core, 13.4 mm in diameter. A complete core usually consisted of a steel front plate, the ceramic and rear support which contained the fiducial. The front plate was Type S7 tool steel hardened to 285 BHN. The rear support was Al-alloy in early experiments, but was later changed to the same steel used for the front plate. Epoxy, with a typical thickness of 0.05 to

0.08 mm, filled all interfaces. The core was retained in the lateral confinement by a threaded steel plug. Sketches of small scale reverse ballistic targets are shown in figures 1–4.

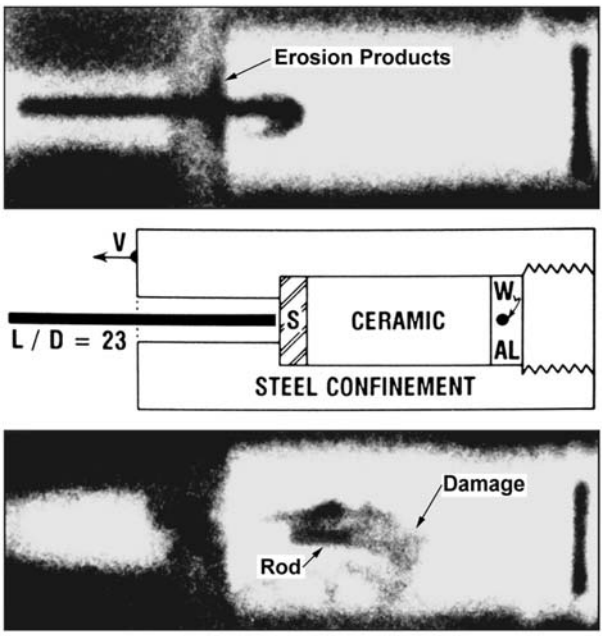

Figure 1. Radiographs of a target configuration that produced penetrator "dwell" at the ceramic surface and damage ahead of the penetrating rod.

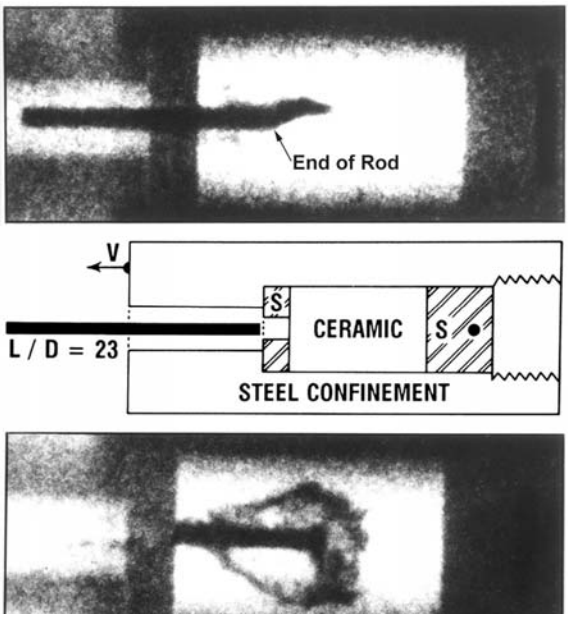

Figure 2. Radiographs of a target configuration that eliminated dwell at the ceramic surface and produced well-defined damage ahead of the long-rod projectile.

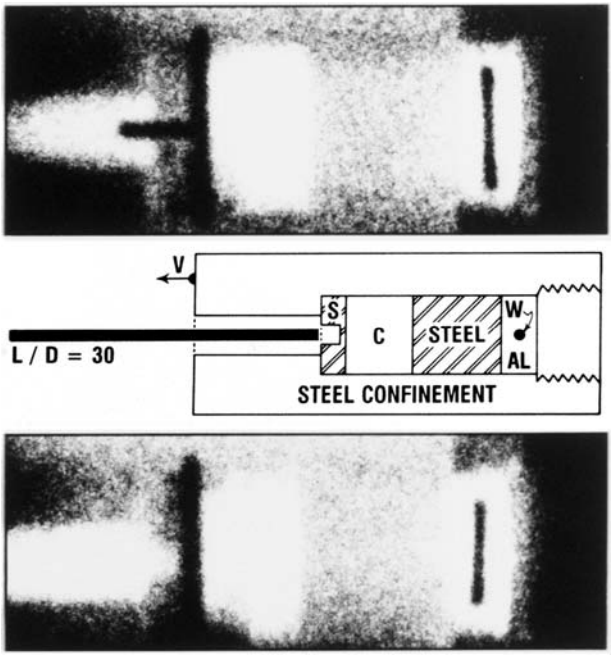

Figure 3. Radiographs of a target configuration that produced interface defeat of a long-rod projectile by a modification to the front confinement of the TiC ceramic.

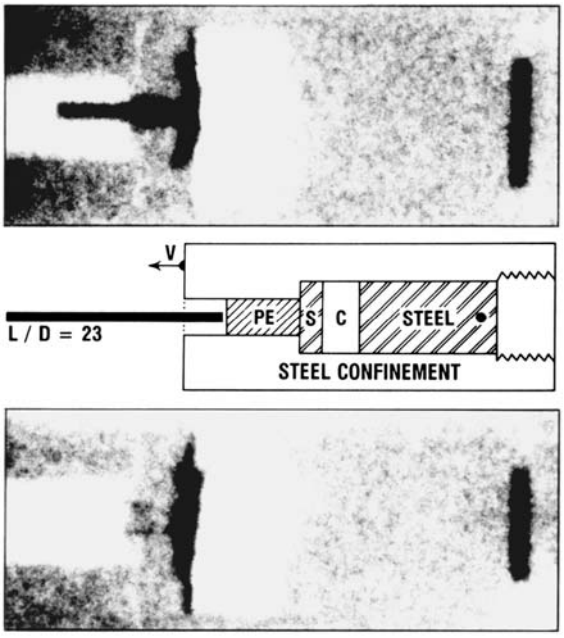

Figure 4. Radiographs of a target configuration that produced interface defeat of a long-rod projectile by attenuating the impact-induced shock wave.

2.2 Dwell and Ceramic Damage

The target configuration for an early experiment, and the radiographs recorded during penetration, are shown in figure 1. Ceramic in this experiment was aluminum oxide (Al_2O_3) with a purity that exceeded 99%. The radiographs reveal two features of penetration behavior that commonly influence the ballistic performance of ceramics: (1) a delay in the onset of penetration, referred to as dwell, and (2) damage to the ceramic. In the upper radiograph, eroded penetrator material has accumulated at the interface between the front confinement and the ceramic. This accumulation indicates a delay between the initial impingement of the penetrator onto the ceramic and the onset of penetration. A dwell time of ~5–7 μs was estimated by using the Tate penetration model (Tate 1967, 1969; Hauver et al., 1992) to examine penetration data. Uncertainty about the duration of dwell came from two sources: (1) the necessary assumption of constant penetration resistance after the onset of penetration and (2) the depth of penetration (DOP) at the time of the earlier (upper) radiograph. In the later (lower) radiograph, erosion products have propagated into damaged ceramic ahead of the penetrating rod, identifying the presence of damage in that area. Erosion products also appear to lead the penetrator in the earlier radiograph, but they have not yet dispersed enough for the tip of the rod to be precisely located.

2.3 Elimination of Dwell at the Ceramic Surface

The evaluation of ballistic performance during penetration was influenced by uncertainty about the delay before penetration. In an attempt to prevent dwell, a hole was drilled through the front confinement to admit the long-rod projectile for direct impact against the ceramic. The blunt nose of the rod produced severe shock loading upon direct impact. In experiments with high-purity Al_2O_3, direct impact eliminated the delay. As shown in figure 2, no erosion products accumulated at the surface of the ceramic. This observation is consistent with the results of a study (Dandekar and Bartkowski, 1994) which found that a WHA rod, impacting AD-995 Al_2O_3 at a velocity of 1500 m/s, produces an impact stress of 35 GPa and causes the ceramic to suffer nearly a complete loss of shear strength. Figure 2 also shows erosion products ahead of the penetrator. However, the orthogonal radiographs in figure 2 clearly show that the erosion products are confined to a thin plane of damage. The view in the upper radiograph is parallel to the plane; the view in the lower radiograph is normal to the plane. The plane of damage also is parallel to one pair of flat surfaces at the outside of the confinement. This relationship of the damage plane to the outside boundary of the confinement was observed repeatedly in subsequent experiments with high-purity Al_2O_3, and it indicated that unloading waves return from the free boundary of the confinement and interact to produce tensile damage near the center of the ceramic. Similar damage was also encountered in later experiments at a larger scale.

The damage with a planar signature results from unloading waves which originate at the planar portion of the outside boundary, and the distinctive signature alerts an investigator to behavior with a probable influence on the resistance of the ceramic to penetration. However, the planar portion represents only 64% of the lateral surface area. Rounded areas, where corner material

was removed, represent the remaining 36% of the lateral surface. Unloading waves from these rounded areas should focus to the axis of the ceramic, where damage should be enhanced. There should be no distinctive signature by which to identify the presence of this damage, and it is conceivable that such damage could introduce scattered performance that depends on the location of impact.

2.4 Discovery of Interface Defeat at the Ceramic

Direct impact did not cause immediate penetration into all ceramics. In the case of hot-pressed titanium carbide (TiC), the delay with steel front confinement was determined to be 5.5 μs, corresponding closely to the delay observed with high-purity Al_2O_3 and steel front confinement. However, when a hole was drilled through the front confinement to allow direct impact against TiC, the delay before penetration was increased to ~15 μs. This behavior suggested that TiC retains strength, and possibly strengthens, under shock-wave loading. This result also led to the hypothesis that there might be a relationship between the delay before penetration and the development of damage in the ceramic. For example, with direct impact, the ceramic experiences the peak impact stress, but erosion products have longer to accumulate at the interface before unloading waves return to initiate tensile damage. The greater accumulation of erosion products results in a compressive interface stress which tends to suppress tensile damage. The hypothesis suggested that by varying the thickness of front confinement under the impacted area, it might be possible to find a set of conditions (shock-wave attenuation and accumulation of erosion products) that would permit the interface stress to suppress damage and prevent any penetration into the ceramic. To evaluate the hypothesis, thickness under the impacted area was reduced to approximately one-quarter of the original thickness of the front confinement. As shown in figure 3, this modification prevented penetration and totally defeated the penetrator by a sustained lateral flow of erosion products into the interface between the front confinement and the TiC.

After interface defeat was produced by modifying the front confinement of TiC, it was also produced in other ways. In figure 4, for example, interface defeat by high-purity Al_2O_3 resulted from placing a 12.7-mm thickness of polyethylene against the outside of the steel front confinement. This modification moved the source of the impact shock further from the ceramic and allowed attenuation by divergence during the additional travel. The upper (earlier) radiograph in figure 4 displays improved detail that resulted from the use of 2-mm-diameter anodes in the x-ray tubes of megavolt systems. Compression of ceramic under the impingement area, as well as a displacement of material that results when flow from the impingement area invades surrounding ring cracks, is evident. The resulting surface contour of the ceramic misdirects the flow of erosion products into the back of the front steel plate. The impeded flow should cause increased stress in the central region, and the initial 90° flow might change to 180° flow, doubling stress in the impingement area. However, an analysis of penetration through the steel front plate indicates that the erosion products should have been nearly stationary in laboratory coordinates and could easily masquerade as later 180° flow from the impingement

area. In any case, the interface stress is apparently sufficient to support the front surface of the ceramic, preventing ceramic displacement and penetration.

In a different approach, full-term interface defeat by titanium diboride (TiB_2) resulted from drilling a hole through the front confinement to allow direct impact against the ceramic. For this experiment, the stationary rod consisted of a 5 mm-long segment of WHA, a 7-mm-long segment of zinc (Zn), and a final 36-mm-long segment of WHA, all in direct contact. The 5-mm WHA segment was consumed during the expected dwell. The following Zn segment had little ability to penetrate, and its primary function was to flow laterally into the interface. This additional flow apparently contributed to the compressive interface stress, which helped to suppress damage, allowing the final 36-mm-long segment of WHA to be defeated at the interface. A study by Dandekar and Benfanti (1993) supports such high ballistic performance by TiB_2 subjected to direct impact. They found that this ceramic sustains increasing shear strength with increasing compressive stress to values of at least 60 GPa.

2.5 Concerns About the Small-Scale Experiments

Although reverse-ballistic experiments contributed insight into damage, suppression of damage, and the resistance of ceramics to penetration, they introduced two areas of major concern. First, despite successful interface defeat, there was concern that there might be a finite time-to-failure, and that this might allow high ballistic performance by ceramics only in small-scale experiments. Second, the mass of the target was a major concern because it limited the light-gas gun experiments to a maximum velocity near 1450 m/s. This limiting velocity is below velocities of primary interest in current ballistic studies. As a consequence of these concerns, the small-scale, reverse-ballistic experiments were discontinued. Later experimental results failed to provide support for the first area of concern. However, the velocity limitation remained a concern, so small-scale reverse ballistic experiments were not resumed.

3. Ceramic Behavior in Larger-Scale Experiments

3.1 Larger-Scale Experiments With Flash Radiography

Targets for conventional, larger-scale experiments were initially three times the size of targets used in reverse-ballistic experiments. The confinement was changed from steel to titanium alloy (Ti-6Al-4V, 330 BHN), which permitted flash-radiographic observations and measurements within the larger target. The confinement had a 76 mm × 76 mm cross section and was machined to accept a ceramic core with a diameter of 38 mm. Front confinement and back support for the ceramic were made of the same titanium alloy. The back support contained fiducial rods of W, which, as in the reverse-ballistic experiments, provided a reference for radiographic measurements. For some measurements early in the penetration, side confinement was eliminated and the diameter of the ceramic was increased to 102 mm. The larger tile

diameter prevented a lateral unloading wave from returning to the penetration path during the time interval of measurements. That is, the ceramic was inertially confined.

3.1.1 Experimental Procedure

In conventional experiments, long-rod projectiles with a hemispherical nose were launched at stationary ceramic targets. Different projectiles were used during the investigation. Initially, projectiles were made of the 90W-7Ni-3Fe alloy previously used for projectiles in the reverse-ballistic experiments. However, the diameter was increased from 1.58 to 4.93 mm, and the L/D ratio was limited to 20. Later, projectiles were made of the Teledyne 93% W alloy, X21. The standard X21 projectile also had a diameter of 4.93 mm, an L/D ratio of 20, and a mass of ~32.5 g. Projectiles were initially launched at 1500 m/s, but the velocity was increased to 1600 m/s as the ballistic performance of ceramic targets was improved. A velocity of 1600 m/s was close to the upper limit available with the single-stage light-gas gun.

In conventional experiments, as in reverse-ballistic experiments, the target configuration was modified frequently to determine influences on the ballistic performance. Most of the experiments were conducted with high-purity Al_2O_3 ceramics. These ceramics were primarily sintered AD-995, made by the Coors Ceramics Company, or hot-pressed Ebon A, made by CERCOM, Inc. For a given type of ceramic, material variations were found to have less influence on the ballistic performance than characteristics of the target system. For example, Ebon A was slightly superior to AD-995 in most of the comparisons, but different target configurations produced major changes in the penetration resistance of both ceramics.

3.1.2 Variable Ballistic Performance of Al_2O_3

The three targets depicted schematically in figure 5 provide an initial example of how the target configuration can influence ballistic performance. The ceramic in these targets was Ebon A. Each target was attacked by a long-rod projectile launched at a velocity of 1500 or 1600 m/s. In target A, the ceramic was 6 mm thick and was bonded to the steel backing by ~1 mm of epoxy. The average resistance to penetration, interpreted by the penetration model, was 2.3 GPa. In target B, the ceramic was much thicker and flash radiography was necessary to measure the time required for penetration to a depth of 6 mm. From this measurement, the average resistance to penetration was determined to be 6.0 GPa. In target C, a 6-mm thickness of steel was bonded to the front of thick Ebon A, and flash radiography was again used to measure the time required for 6 mm of penetration into the ceramic. For target C, the average resistance to penetration was determined to be 12.1 GPa.

Average resistances from 2.3 to 12.1 GPa, for penetration through 6 mm thicknesses of Ebon A, can be explained in terms of ceramic damage. In the case of target A, impact against bare Ebon A produced a peak shock stress of ~36 GPa. Measurements by Dandekar and Bartkowski (1994), using a comparable Al_2O_3 ceramic, showed an almost complete loss of shear strength

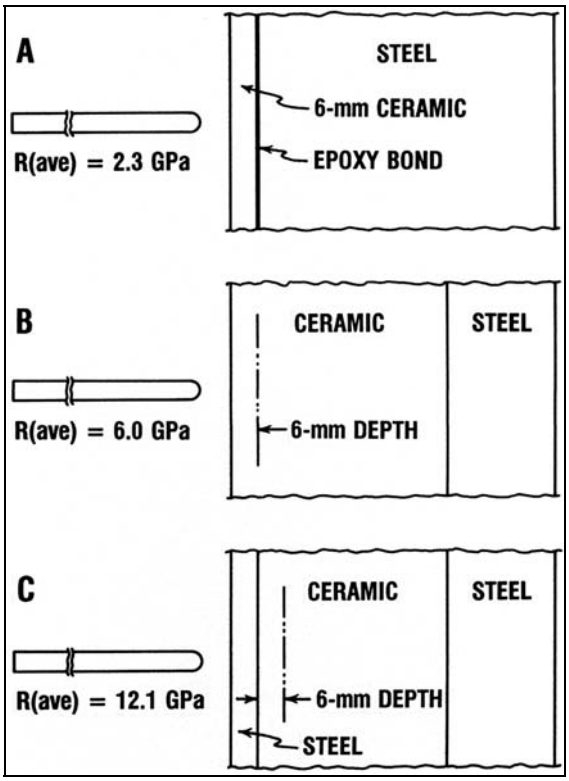

Figure 5. Targets that demonstrate the influence of the configuration on ballistic performance.

at this impact stress. This result suggests that the resistance to penetration should initially be low. Based on the guidance of stress-wave measurements by Franz and Leighton (1992), the shock wave arriving at the low-impedance epoxy interface should retain a stress level well above the measured spall strength of AD-995 (Dandekar and Bartkowski, 1994), so tensile damage should occur near the interface and contribute further to a loss of performance by the ceramic. This assessment of performance is supported by the performance of target B. Here, the absence of an interface with a low-impedance bond eliminated one source of damage to the ceramic. The average resistance to penetration was then degraded only by impact damage, so the performance of the ceramic increased from 2.3 to 6.0 GPa. In the case of target C, front steel confinement permitted some attenuation of the diverging impact shock before it arrived at the ceramic. Later, it will be shown that the ceramic in this target resisted penetration for a time interval of ~4 μs. This delay (dwell), followed by an average resistance of 7.7 GPa after the onset of penetration, produced an apparent average resistance of 12.1 GPa.

Figure 6 contains three radiographs that show features of penetration that are related to the behavior of the targets in figure 5. Panel A shows features of the penetration after a long rod impacted bare Al_2O_3 ceramic. Damaged ceramic has been expelled from around the area of impact, and there is evidence of major fractures around the penetration path. It is reasonable to assume that such damage contributed to the lower ballistic performance determined for targets A

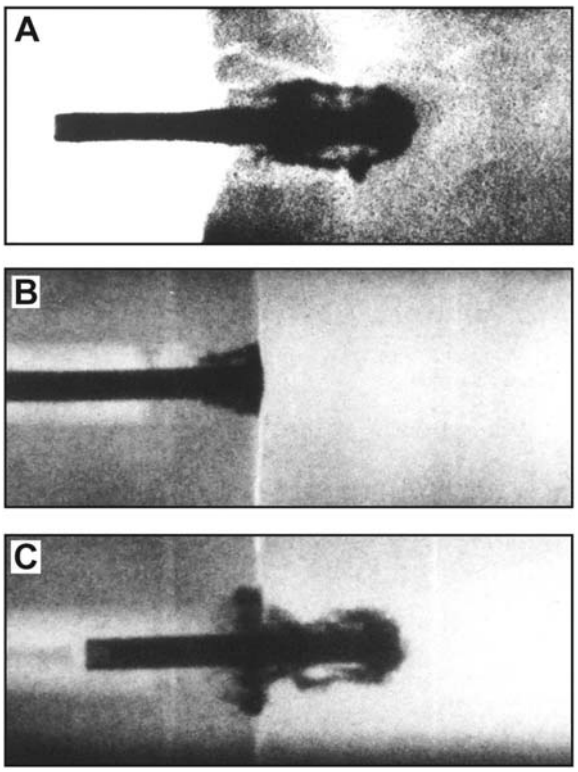

Figure 6. Radiographs that show features of penetration which are related to the performance of targets shown in figure 5.

and B in figure 5. Panel B of figure 6 shows a long rod during the delay (dwell) before penetration into Al_2O_3. Here, and in panel C, the front confinement was a 12.7-mm thickness of titanium alloy. At an impact velocity of 1500 m/s, erosion products produced during penetration through the front confinement should flow forward in laboratory coordinates and contribute to the accumulation at the interface.

The tip of the penetrating rod cannot always be located reliably after the onset of penetration into Al_2O_3. Such uncertainty could influence a measurement on panel C of figure 6, but the problem is illustrated more clearly by the radiographs in figure 7. Damage from the interaction of unloading waves occurs ahead of the rod. Erosion products migrate forward into the damaged region, and this is most clearly evident in panel B of figure 7. These erosion products can obscure the tip of the rod, and an analysis based on the leading edge of erosion products gives a low resistance to penetration.

Figure 8 shows a recovered tile of Al_2O_3 with the front confinement removed. When the damage is viewed from this perspective, it is evident that damage is initially concentrated in orthogonal zones. Referring to figure 7, it becomes evident that one zone degenerates while the other zone develops and dominates, producing the planar damage that is observed in aluminum oxide targets at later times during the penetration.

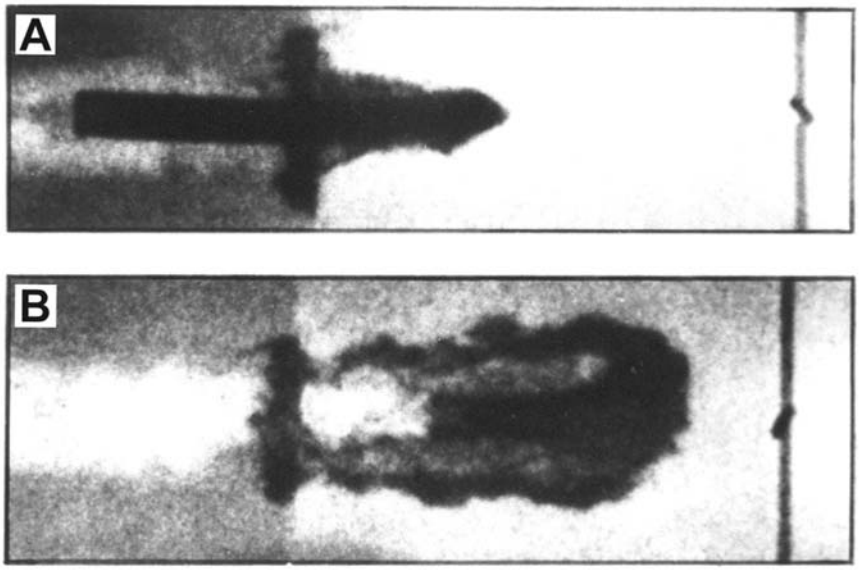

Figure 7. Radiographs which show that the forward migration of erosion products into damaged ceramic can obscure the location of the tip of the penetrator.

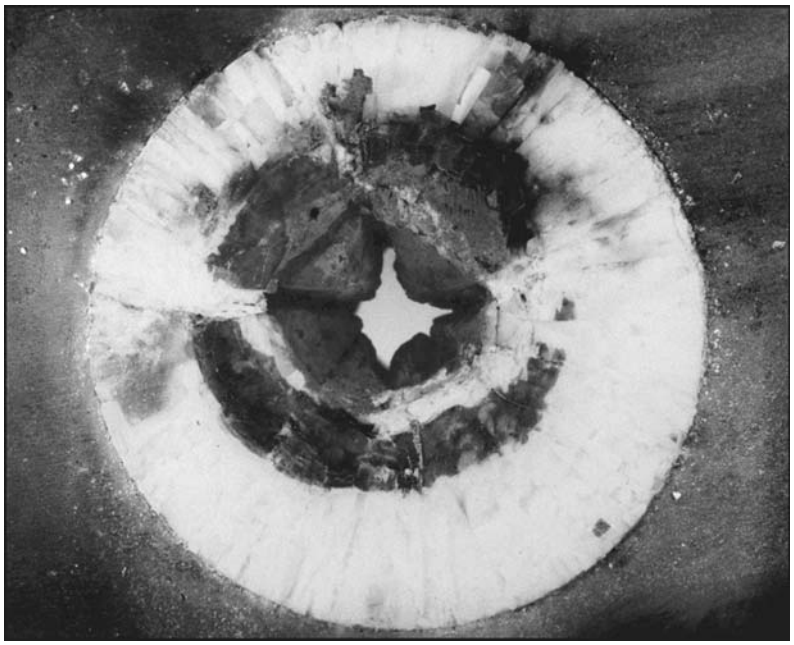

Figure 8. Recovered ceramic with orthogonal damage planes caused by unloading waves from the square outside boundary of the target.

3.1.3 Control of Wave Damage in Al_2O_3

The wave damage that occurs in Al_2O_3 targets can be modified by modifying the target configuration. Panels A and B in figure 9 show radiographs of the complete penetration path in the target of figure 7. Panels C and D in figure 9 show the modified penetration path produced

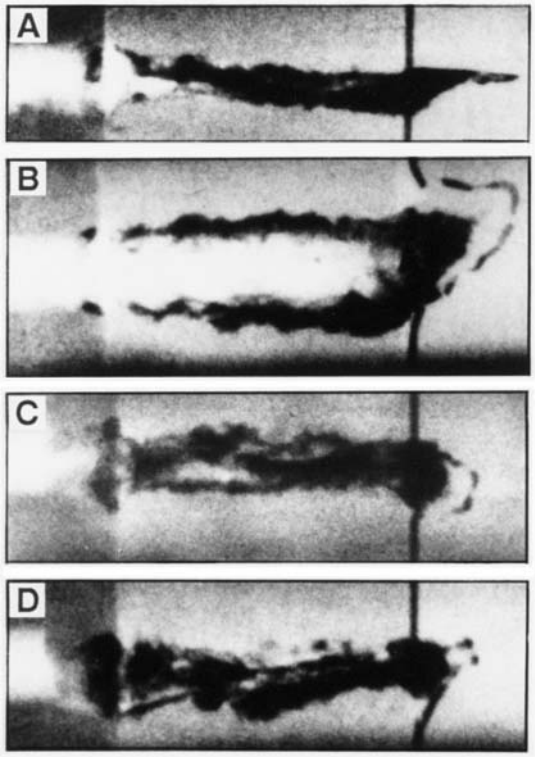

Figure 9. Radiographs that show that ceramic damage can be modified by boundary treatments.

by installing wave traps on the four side faces of a similar ceramic target. The wave traps were 6-mm-thick plates of titanium, weakly coupled to the side surfaces. Interfaces transmitted the compressional wave, but had negligible strength in tension. The interfaces separated when the reflected wave arrived, trapping part of the wave in the plates. Despite the nonplanar nature of the incident wave, these traps were sufficiently effective to eliminate planar failure and restore symmetry to the penetration path. However, an unloading wave should also occur as a result of impedance mismatch at the cylindrical boundary between the aluminum oxide and the titanium confinement. This cylindrical interface should focus the unloading wave to the vicinity of the penetration path. There should be no distinctive signature, as in the case of a square outside boundary, to indicate damage from the focused wave interaction. Wave damage, in the absence of penetration, was examined in transparent target configurations, and this study is discussed in the next section of the report.

3.2 Wave Damage in a Transparent Ceramic Surrogate

Damage from wave interactions, without the complicating presence of penetration, was produced by using small explosive charges to generate shock waves in acrylic targets. Similar studies were initially conducted by Kolsky and his associates (1963). Figure 10 shows the orthogonal damage produced in an acrylic target with a square cross section. One crack dominates, while

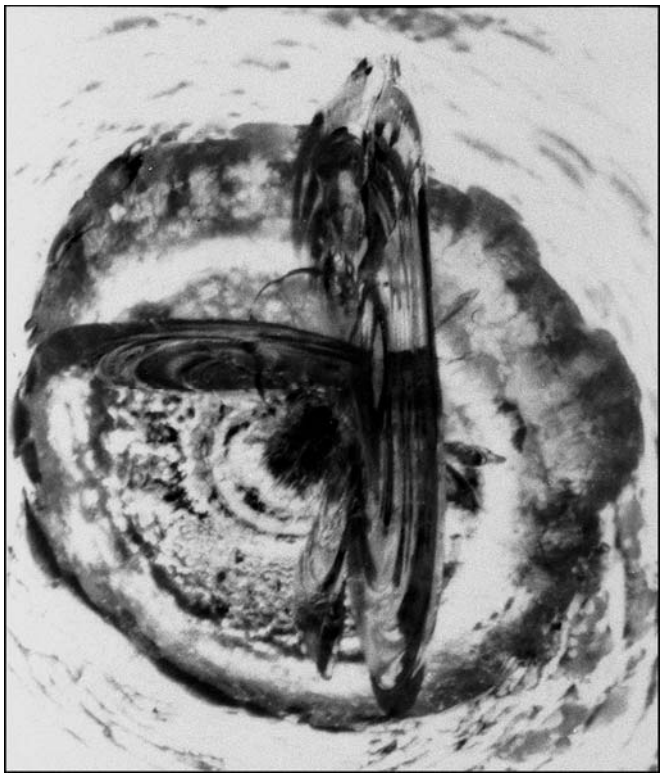

Figure 10. Photograph of orthogonal planes of wave damage in an acrylic block with a square boundary.

the other does not form completely. This behavior is analogous to the behavior observed in targets of Al_2O_3 ceramic where orthogonal zones of damage were present just under the front confinement, although only one zone of damage persisted to produce the planar failure in panels A and B of figure 9.

Damage in targets with a circular cross section is a special concern because the reflected wave converges to the central region of the ceramic. In a penetration experiment, convergence should not leave the distinctive damage signature observed in a ceramic target with a square cross section. With convergence, there is nothing in radiographs to distinguish the zone of damage from the penetration path, and penetration probably destroys the evidence of damage responsible for a low resistance to penetration.

Acrylic targets, with right-cylindrical shapes, were shock loaded by small explosive charges which were detonated to simulate projectile impacts. After the experiments, each target was machined to produce parallel faces which were polished to give an undistorted view of internal damage. Three targets are shown in figure 11. Target A in the figure was shocked at the axis, so the reflected unloading wave converged to the axis where a zone of damage developed. The onset of this damage corresponds closely to the arrival time of a wave propagated at the longitudinal velocity (Netherwood, 1972). Target B was shocked 10 mm away from the axis, so the reflected wave converged to a zone of damage diametrically displaced by nearly 20 mm.

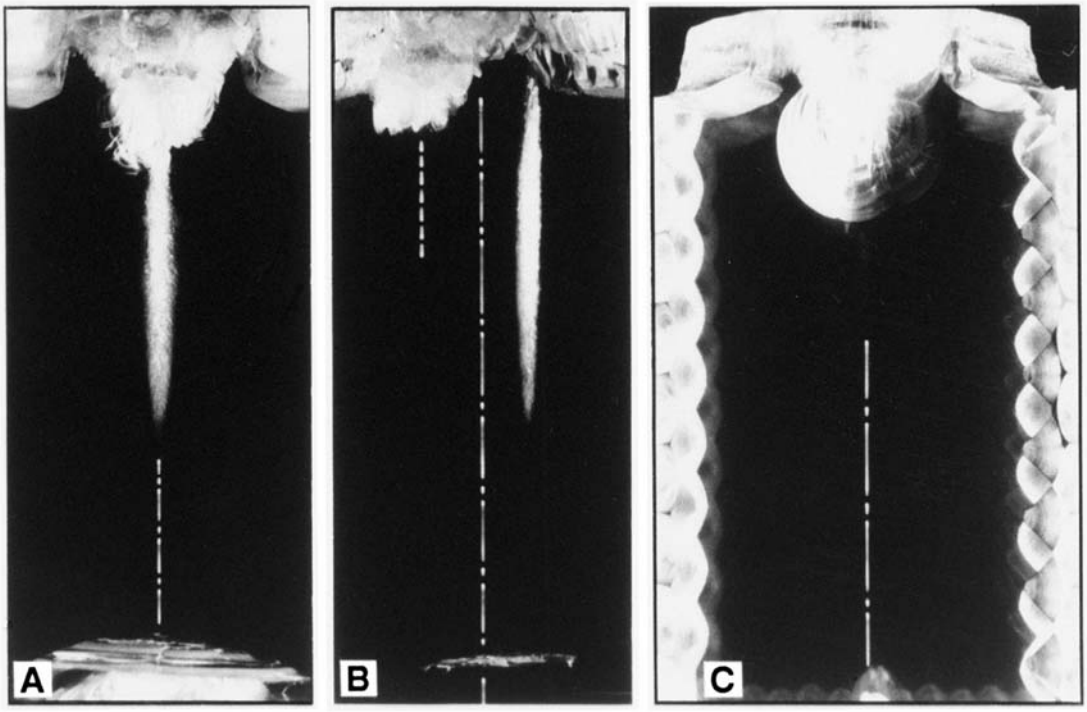

Figure 11. Photographs that show wave damage in acrylic targets and suppression of damage by a boundary configuration that defocuses the unloading wave.

These observations suggest that the scatter of performance data from penetration experiments with ceramics may depend on the target geometry and the location of impact. The cylindrical and back surfaces of target C were configured with close-packed arrays of 118° included angle conical depressions. Although this target was shocked at the axis, the surface configuration effectively defocused the reflected unloading wave and an axial zone of damage is barely detectable. In the absence of other damage, one radial crack has become dominant near the top of the target.

The Kolsky-type studies provide a visual confirmation of damage found in opaque ceramic targets during and after penetration experiments. Targets with a square cross section are especially informative because the distinctive signature provides a direct comparison of visual evidence and radiographic evidence. The use of defocusing surface configurations is equally informative because tests demonstrate a reduction of damage which should relate directly to increases in the ballistic performance found in penetration experiments. The main difference between experiments with only shock and experiments with combined penetration and shock may be the presence of a stress field around the advancing penetrator. The presence of a stress field may alter both the magnitude and extent of wave damage produced in a ceramic target.

3.3 Larger-Scale Experiments Without Flash Radiography

Flash-radiographic observations and measurements provided helpful insight into ceramic damage and its influence on penetration, but the compromises necessary for radiography were excessive.

The use of titanium alloy for lateral confinement became a major concern because of an impedance mismatch with the confined ceramic. A reflected wave should converge to the vicinity of the penetration path where damage might be significant. In addition, expansion of the confinement indicated that the titanium alloy provided only marginal support for the ceramic. Consequently, radiographic studies of damage were discontinued, and larger ceramic tiles with more substantial confinement were introduced.

3.3.1 Experimental Procedure

Targets for larger-scale experiments without radiography were initially built with the general configuration shown in figure 12. Experiments were conducted with either AD-995 or Ebon A, and the larger-scale target underwent a series of modifications to determine the influence on performance. Modifications included (1) the thickness and characteristics of the front confinement, (2) the dimensions of the ceramic, (3) the support for the ceramic, (4) the boundary configuration to disperse unloading waves, and (5) the method of clamping to minimize a separation of target layers. Ballistic performance was evaluated by a DOP procedure (Woolsey et al., 1989) which was modified to include front confinement. Data were again analyzed by the Tate penetration model to interpret performance in terms of average resistance to penetration. With the general configuration in figure 12, the performance of AD-995 or Ebon A could be varied from the lower limit of scatter in standard DOP tests to a value ~50% above the upper limit of standard DOP data (Hauver et al., 1992, 1993). The highest levels of performance were obtained with a 12.7 mm thickness of rolled homogeneous armor (RHA) (330 BHN) as front confinement, and with the ceramic prestressed by a shrink fit of the side confinement. The side surfaces were configured to disperse reflected waves, and layers of the target were well-clamped to minimize separation at interfaces.

The highest levels of performance were later achieved with the modified larger-scale target shown in figure 13. RHA confinement with an inside diameter of 74.11 mm was heated to 480 °C to accept a core with a diameter of 74.26 mm. The layered core consisted of a 12.70-mm thickness of RHA, a 24.90-mm thickness of Ebon A, and RHA backing. The shrink fit minimized separation of the core during penetration. A configured boundary was added to disperse reflected waves, and both square and circular boundaries were tested. With a configured boundary, the shape of the outer boundary could not be detected to influence the ballistic performance.

3.3.2 Target Data and Analysis

Selected performance data for Ebon A are plotted in figure 14 and are identified by numbers of the experiments. In this plot, performance is expressed as average resistance to penetration and is plotted as a function of time after the penetrator arrives at the ceramic. Data for Ebon A from other experiments with thinner, 6.35-mm-thick, front steel confinement are included for comparison. A reference curve for Ebon A was obtained by using the Tate model to analyze data

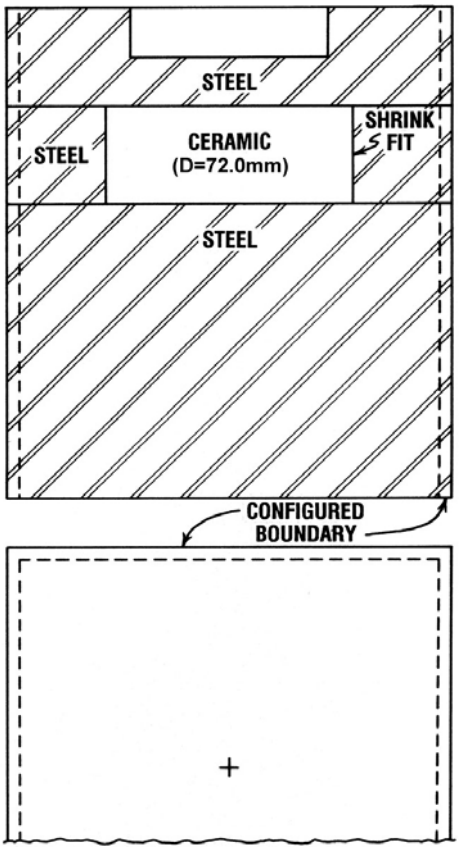

Figure 12. Larger-scale target used to evaluate the ballistic performance of ceramics without the aid of radiographic observation during penetration.

from standard DOP tests (Woolsey et al., 1989). A casual inspection of data suggests that adding front confinement, and increasing its thickness, improves the average resistance to penetration. However, more detailed inspections of targets and data provided additional insight.

Steel (RHA) front confinements from Experiments 280 and 286 were sectioned, and surface profiles on one side of the penetration path are shown in figure 15. These profiles show the cavity produced in the front steel confinement during the delay in penetration (dwell). Each cavity still contains some of the eroded penetrator material. By measuring the contour of each cavity, assuming symmetry, and taking into account the presence of an incoming rod, the volume of rod material eroded during dwell was estimated. Approximately 28% of the L/D = 20 rod was eroded during dwell in Experiment 286 and ~31% of the rod was eroded during dwell in Experiment 280. Using the penetration model, the duration of each delay was estimated. With this correction for the penetration time, the average performance of Ebon A was reevaluated after the onset of penetration.

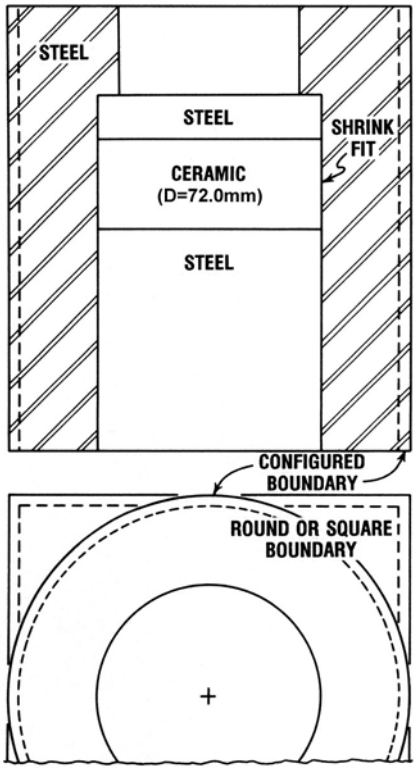

Figure 13. Modified larger-scale target used to evaluate the ballistic performance of ceramics without the aid of radiographic observation during penetration.

Experiment 277 could not be reevaluated using an estimate of delay time based on a measurement of cavity volume. The thin, 6.35-mm-thick, front steel confinement in this test bulged and failed almost catastrophically, preventing a reliable estimate of eroded volume. However, Experiments 276 and 279 provided flash-radiographic measurements of depth just after the onset of penetration, and these early data were extrapolated to the onset of penetration to obtain a delay time of ~4 μs. Using this delay time, the average performance in Experiment 277 was also reevaluated after the onset of penetration.

Reevaluated data from figure 14 are plotted in figure 16. These data suggest that the ceramic displays two levels of performance. It either resists penetration completely or it permits penetration at a level of performance which lies within the scatter of ballistic performance defined by standard DOP tests. There appears to be a rapid transition from one level of performance to the other. An area of uncertainty in figure 16 is the level of performance before the onset of penetration. In order to evaluate dwell time by the penetration model, it was necessary to introduce a value of target resistance no lower than 24.4 GPa. However, flow

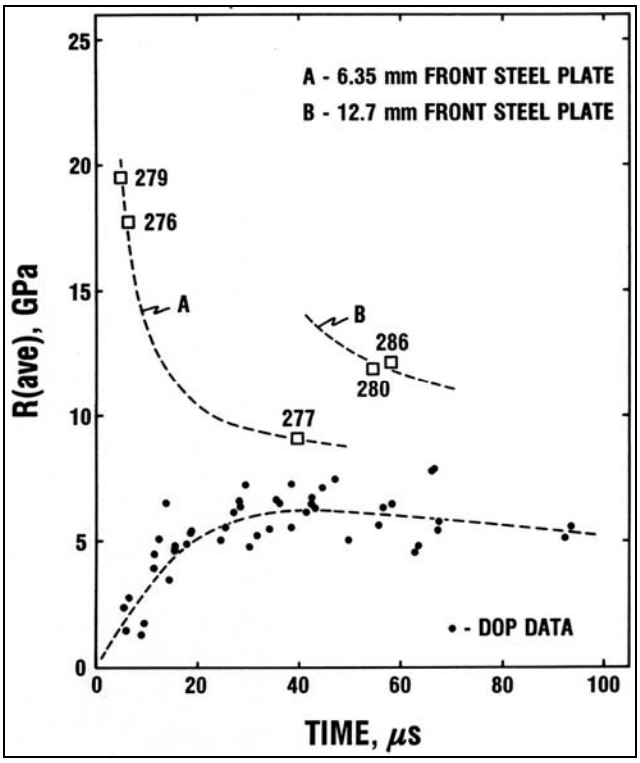

Figure 14. Data that represent the ballistic performance of Ebon A Al_2O_3 ceramic.

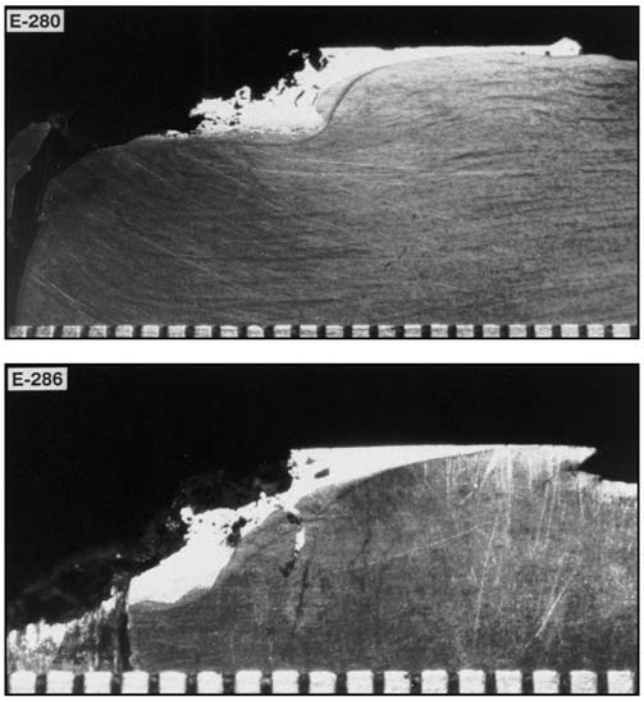

Figure 15. Cavities produced in steel front confinement by the accumulation of erosion products during penetration delay at the ceramic surface.

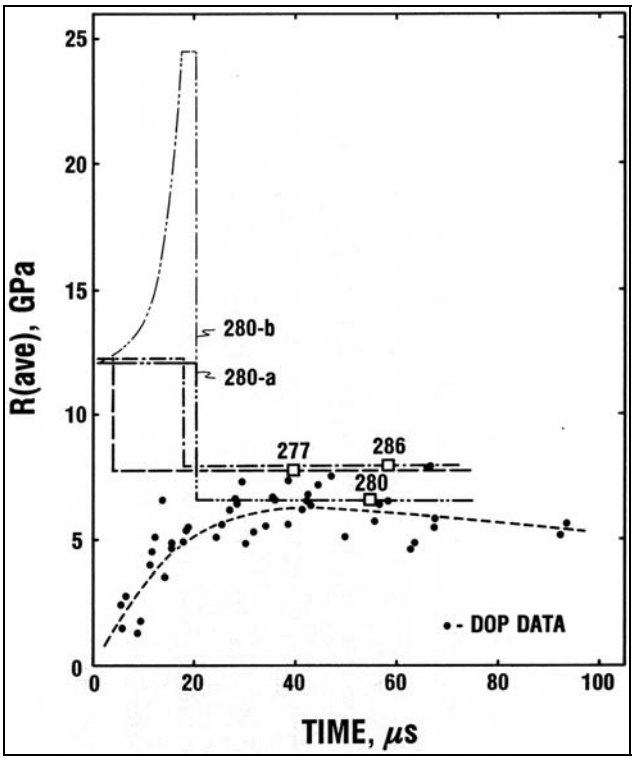

Figure 16. Reevaluated data that suggest that the ceramic displays two levels of ballistic performance.

inherent in the model is different from flow actually encountered during dwell. In the model, the consequence of zero penetration velocity (u = 0) is a reverse flow of projectile material with a velocity change (2v). If u = 0 because the eroded projectile material undergoes unimpeded lateral flow, the change in velocity at the ceramic is v, not 2v. Consequently, figure 16 initially depicts a dwell stress which is half the value calculated by the model. Actually, the sectioned targets in figure 15 show that the lateral flow became impeded, causing an increase in stress. A complete reversal of flow would have allowed a stress increase to 24.4 GPa. As an example, an arbitrary curve (280-b) has been indicated in figure 16. Curve 280-a, equally arbitrary, assumes unimpeded lateral flow until the onset of penetration. In reality, the actual stress-time history during dwell is presently unknown.

3.3.3 Impeded Radial Flow

The front confinements shown in figure 15 were examined further for evidence of behavior that might be related to the ballistic performance. In both panels of figure 15, eroded material has attempted to flow radially from the cavity and into the interface between the front confinement and the ceramic. In the upper panel, incipient shear failure is present and probably helped to impede the radial flow. In the lower panel of figure 15, there is well-developed shear failure, and a block of steel has become wedged in the interface to prevent the radial flow of erosion products. When extremities of the flow were examined microscopically, W grains were found to

pile up and deform, displacing matrix material. Such behavior, shown in figure 17, is further evidence of impeded flow. If front confinement is changed to heat-treatable AISI 4340 steel, hardened to 450 BHN, enhanced shear failure drastically impedes the radial flow as shown in figure 18. Such behavior strongly supports an increase in interface stress during the delay before penetration. This higher stress, alone, may not initiate penetration; it may only establish a favorable condition which awaits the development of damage. Damage might be associated with the propagation of radial cracks to the lateral boundary of the ceramic tile or with the propagation of unloading waves which return to the axial region from interfaces with poor coupling. Later studies, for example, established a correlation between damage to the ceramic and the interface surface roughness of confinement applied by a shrink fit.

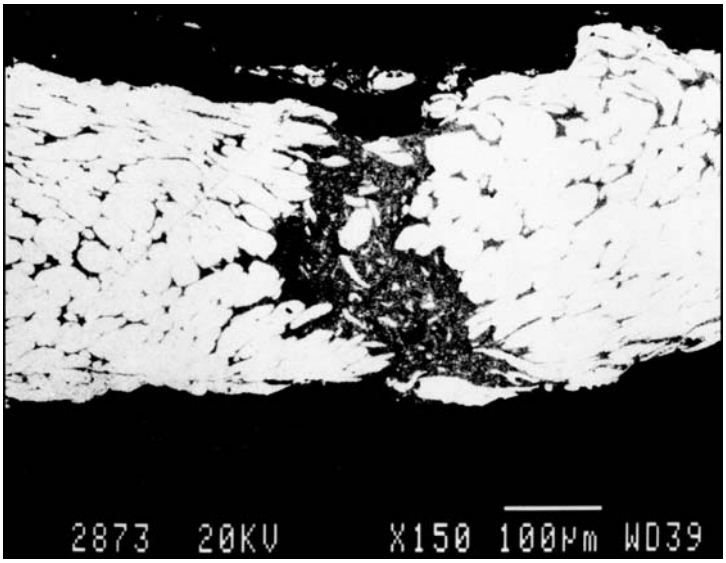

Figure 17. Extremity of impeded radial flow that shows the pile-up of W grains and the displacement of matrix material from the penetrator.

A two-fold benefit should result from eliminating impediments to radial flow. First, the average interface stress over the impingement area should be minimized. Second, if erosion products could continue to flow laterally into a confined interface, they should produce a compressive stress which would support the front surface of the ceramic around the impingement area. Such interface stress should tend to suppress damage and/or support any damaged ceramic.

4. Interface Defeat in Heavy-Target Configurations

4.1 Initial Heavy-Target Configuration

The initial heavy-target configuration is shown in figure 19. This target was introduced in an attempt to produce interface defeat in conventional experiments. New target features were the additions of a shock-wave attenuator at the front of the target and a weak interface layer between

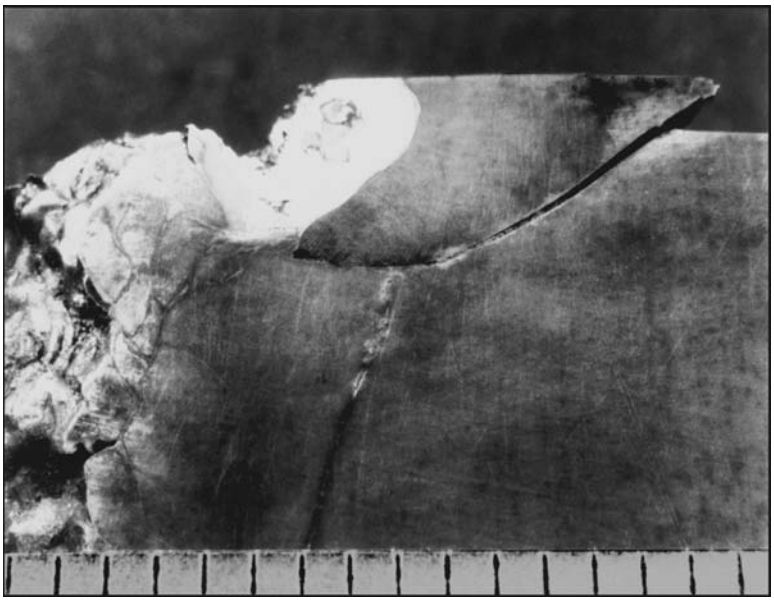

Figure 18. Enhanced shear failure and impeded radial flow caused by front confinement of steel of higher hardness (450 BHN).

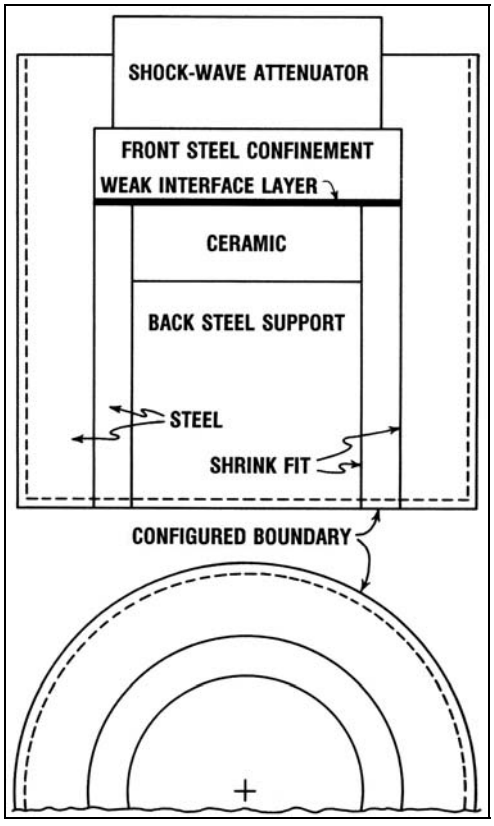

Figure 19. Initial heavy-target configuration that promoted a flow of erosion products at the front surface of the ceramic.

the front confinement and the ceramic. The attenuator was a 38-mm thickness of acrylic. Its function was to move the source of the impact shock farther from the ceramic and allow divergence to reduce the amplitude of stress at the shock front. The initial interface layer was a 0.25-mm thickness of polytetrafluoroethylene (PTFE). This thickness of PTFE was selected as a scaled substitute for the epoxy bond present in reverse-ballistic tests which produced the first interface defeat. Hot-pressed TiC was used because this ceramic sustained interface defeat most effectively in the small-scale, reverse-ballistic experiments. A shrink fit which prestressed the ceramic was retained as beneficial, and a configured boundary was retained as a redundant feature to suppress damage from weak unloading waves.

4.2 Interface Defeat by the Initial Heavy Target

In the first experiment with the heavy-target configuration, a standard X21 projectile, launched at 1600 m/s, was successfully defeated by radial flow, with no penetration into the TiC. Components of the target were recovered after the experiment and are shown in figure 20. Panel A shows the interface side of the front confinement. Erosion products abraded the plate surface as they flowed radially away from the entrance hole. Some erosion products are fused to the surface of the plate near the periphery, but, with the exception of this peripheral deposit, the interface side of the plate is nearly bare. Panel B shows the corresponding surface of the ceramic. The central region exhibits damage to a maximum depth of 2.5 mm. However, the absence of flow lines where material is missing from the ceramic surface suggests that most of the damaged material was separated from the surface after the penetrator was consumed and the radial flow had ceased. Such behavior was confirmed when the target from the next experiment was opened more carefully to reveal most of the ceramic still in place. Substantial areas of shallow damage (0.25- to 0.50-mm flaking) were suspected to result from thermal shock. Panel C shows the inside of the outer confinement and the circumferential slot cut by erosion products which flowed laterally through the interface. Panel D shows the configured surface of the outer confinement, with conical depressions to disperse the unloading wave.

Erosion products, fused near the periphery of the cover plate in a target from a similar test, exhibited much of the microstructure identified by Bless et al. (1992). In particular, the examination of a fragment revealed heavily-deformed W grains, intermixed with ceramic debris retained in the Ni-Fe matrix. However, an additional feature of the tungsten grains should be noted. What appears as an agglomeration of submicron tungsten particles in figure 21 is believed to result from the dissolution of W into the molten matrix and the subsequent reprecipitation during rapid cooling. Although some of this W appears to coat undissolved W grains, a significant fraction appears as fine precipitates. If this interpretation is correct, it provides evidence of elevated temperatures during interface flow and could explain the large areas of ceramic flaking which are attributed to thermal shock.

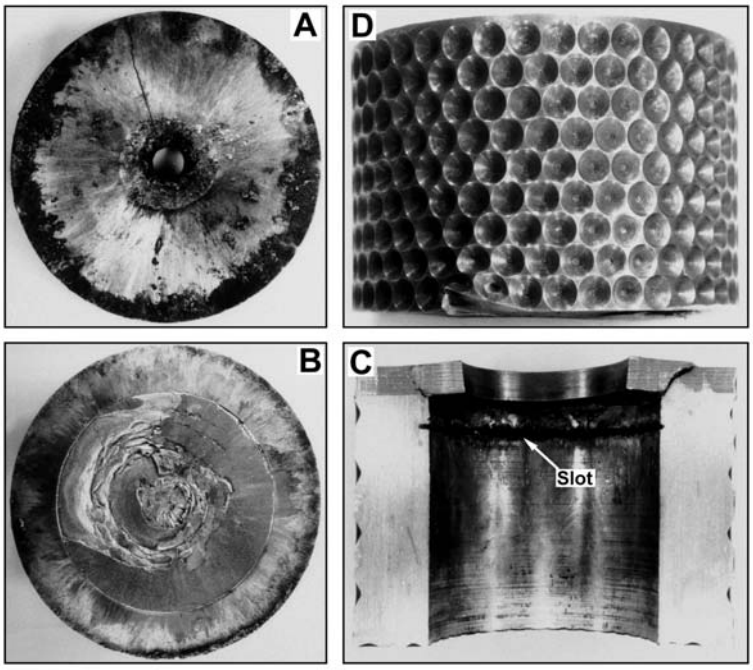

Figure 20. Heavy-target components recovered after an experiment in which the attacking projectile was defeated by radial flow at the surface of the TiC ceramic.

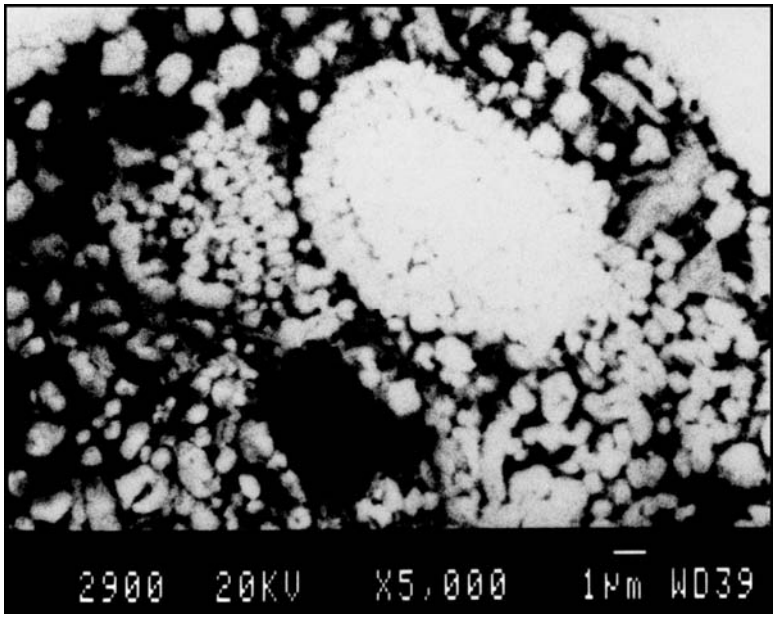

Figure 21. Erosion products with submicron W particles believed to result from dissolution into the molten matrix followed by reprecipitation during rapid cooling.

The TiC ceramic, shown in panel B of figure 20, was removed from its lateral confinement, sectioned, and examined. The cross-sectioned tile is shown in figure 22. Typical macrocracks, as described by Shockey et al. (1990), are present. These macrocracks did not prevent interface defeat, although later experiments established that such damage seriously reduces the ability of a ceramic to resist penetration in a subsequent attack. The cross section reveals, in addition to macrocracks, part of a small region of microdamage under the surface area where the projectile impinged on the ceramic. As target performance was improved, localized microdamage under the impingement area became better defined. Later, well-defined microdamage was found in all but one of the ceramics recovered after interface defeat by heavy-target configurations.

The heavy-target configuration in figure 19 did not perform well, despite its ability to produce interface defeat in a number of experiments. The weak interface layer of PTFE offered little resistance to the flow of erosion products, and the amplitude of interface stress beyond the impingement area may not have provided the support necessary to suppress damage effectively. Damage to the ceramic, as shown in figure 22, was considered excessive. Insufficient shock attenuation also became a concern. The boundary configuration was initially believed to be a redundant feature, but when it was eliminated in two experiments, there was penetration into the ceramic. Studies were conducted to improve the shock-wave attenuator, the effectiveness of the interface layer, and general support for the ceramic. These studies resulted in an improved heavy target for investigating interface defeat.

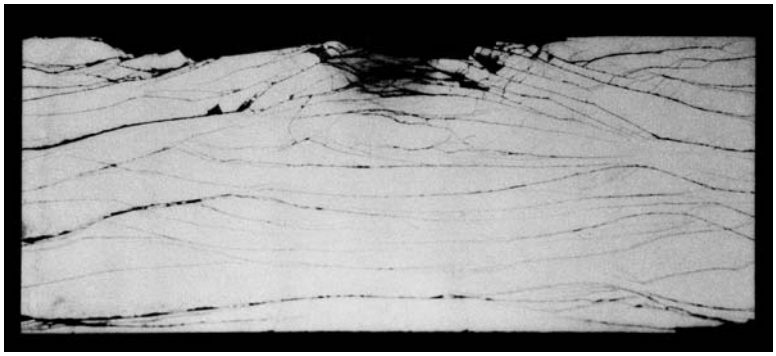

Figure 22. Recovered TiC ceramic, removed from its lateral confinement and sectioned to reveal macrocracking.

4.3 Improved Heavy-Target Configuration

An improved heavy target for the investigation of interface defeat is shown in figure 23. The attenuator converts the impact shock into a ramp wave with reduced amplitude, and measurements at the toe of the emerging wave indicated that it is nearly an order of magnitude more effective than the attenuator in figure 19. The first layer of this attenuator is a 6 mm thickness of porous ceramic. Magnesium oxide (MgO) sputtering plate with a porosity of 33% was the most effective material tested, but Coors Porous Plate (Al_2O_3), with a porosity of about

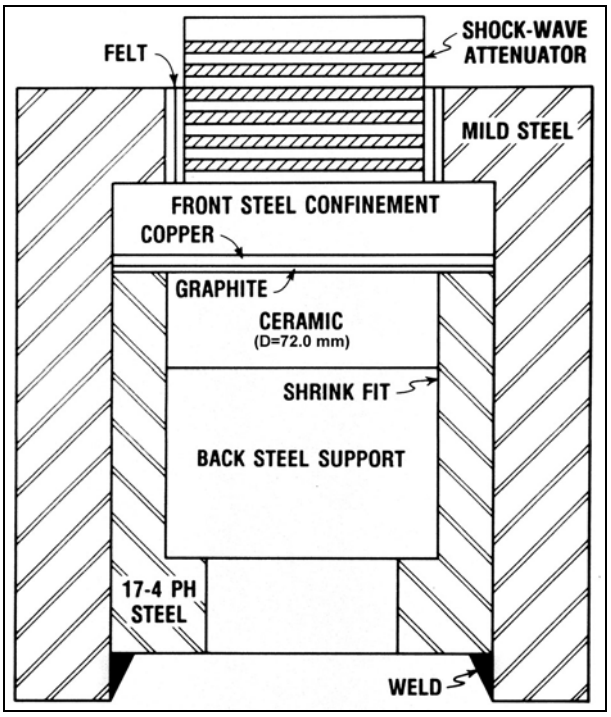

Figure 23. Improved heavy-target configuration for the investigation of interface defeat of projectiles at a ceramic surface.

50%, was routinely used because it was readily available and less expensive. The underlying twelve layers of the attenuator were alternating 3-mm thicknesses of acrylic and aluminum. The front confinement was a 19-mm thickness of AISI 4340 steel, hardened to 415 BHN. This thickness prevented significant bulging and suppressed damage to the ceramic more effectively than 9.5- and 12.7-mm thicknesses of AISI 4340 steel which were tested initially. A 3-mm thickness of copper (Cu) was introduced to suppress shear failure at the back of the front confinement. Finally, the weak layer that accommodates interface flow was changed from PTFE to a 1.5 mm thickness of hexagonal boron nitride (hBN). Later, the weak layer was changed to a 1.5 mm thickness of artificial graphite, with no apparent change in performance. With either hBN or graphite, interface flow seldom extended beyond the 72.01-mm diameter of the ceramic. Ceramic tiles were nominally 25 mm thick. The rear support was AISI 4340 steel, with a thickness of 50.8 mm and a hardness of 415 BHN. The ceramic and its backing were confined laterally by ARMCO 17−4 PH steel with an inside diameter initially 0.13 mm less than the core diameter. Heating this confinement to 480° C provided the clearance for assembly and left the confinement with a hardness of 405 BHN. The outer steel confinement held the core together and was installed using an additional shrink fit. A weld at the base of the target completed the assembly and minimized slippage between the core and the outer steel confinement as internal stress developed during an experiment.

A shrink fit was not used to prestress the ceramic in early reverse-ballistic experiments. Instead, all interfaces in those experiments were filled with epoxy resin. The benefit of a shrink fit in the current experiments was uncertain until two experiments were conducted with the Cu layer and the weak layer recessed, with the ceramic, into the confining tube of 17−4 PH steel. In this location, stress that developed in the weak layer was able to act against the interior of the tube and relieve the prestress provided by the shrink fit. In both experiments, the ceramic was damaged and displaced by the attacking projectile. Later, the improved heavy-target was assembled with epoxy interface bonds as in the earlier reverse-ballistic experiments, eliminating a shrink fit and prestress for the ceramic. In the absence of prestress, and with relatively weak epoxy in the interface at the side confinement, there was penetration through the entire thickness of one of the most resistant ceramics, and evidence of only limited interface flow into the weak layer. Complete interface defeat by the same ceramic in reverse-ballistic experiments, without the benefit of prestress, may have occurred because of the lower attack velocity with reverse ballistics. The value of prestress will be addressed again later in the report.

4.4 Interface Defeat in the Improved Heavy Target

Ceramic tiles were removed from targets after they defeated the standard X21 projectile launched at ~1600 m/s. A recovered tile of hot-pressed silicon carbide (SiC-N), made by CERCOM, Inc., is shown in figure 24. Panel A shows the surface of the tile where the projectile impinged, and a cross-sectional view of the tile is shown in panel B. A coating of fused projectile material highlights the impingement area and the pattern of lateral flow over the surface of the ceramic. Lateral flow extends beyond the ceramic in only a few locations. The circular impingement area is bounded by a ring crack which propagates outward as a shallow cone crack. Some of the projectile material invades these cracks and dislodges ceramic. The greatest loss of ceramic, as shown by the surface profile in panel C, does not exceed a depth of 0.8 mm. A region of microdamage, with a width of ~8 mm, lies beneath the impingement area. This region undoubtedly corresponds to the subsurface damage in SiC-N, produced by spherical indenters, and attributed to local shear-driven deformation (Lawn et al., 1994). The contour of this microdamaged region is similar to reported contours of indentation damage zones in Si_3N_4 (Fischer-Cripps and Lawn, 1996), observed experimentally and simulated by finite element modeling. Two lateral cracks are evident. One crack, which is a result of unloading, passes through the region of microdamage. Another crack is just visible at each side, but disappears within the microdamaged region.

The microdamage in hot-pressed SiC-N from a similar experiment was examined microscopically. Micrographs are shown in the four panels, A to D, of figure 25. The microdamaged region again has a width of ~8 mm. Panel A shows the full area of microdamage. Panel B shows a low level of damage close to the surface where the rod impinged on the ceramic. Panel C reveals mainly intergranular failure at ~0.5 mm beneath the surface. Panel D shows the region of maximum microdamage, located ~2 mm beneath the surface. Here, the

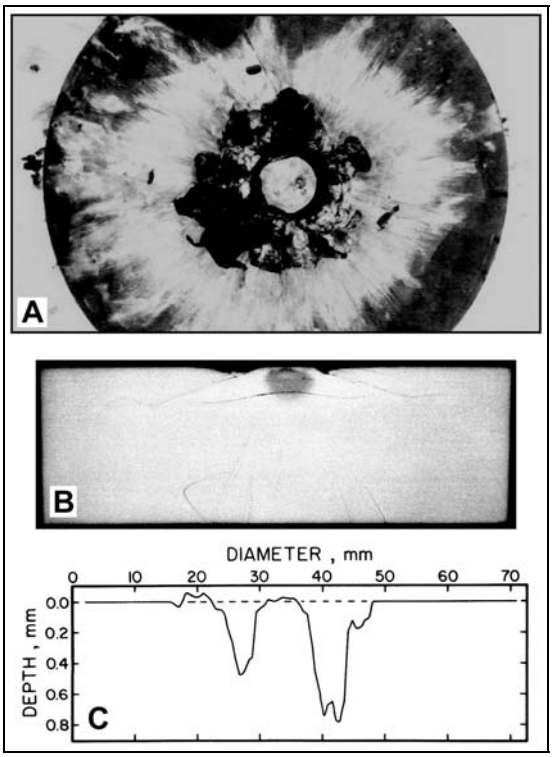

Figure 24. SiC-N ceramic recovered after interface defeat: (a) the impingement area and the pattern of lateral flow, (b) a cross-sectional view that reveals macrodamage and microdamage, and (c) the profile of the front surface.

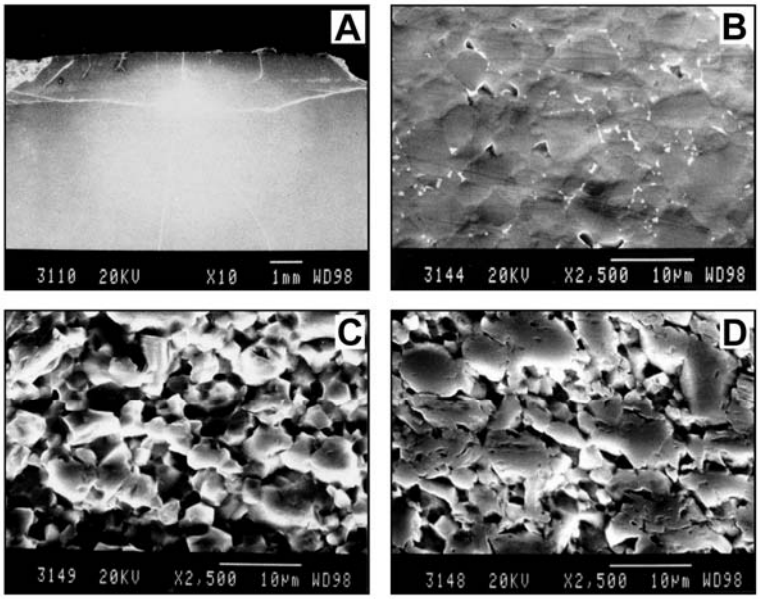

Figure 25. Microdamage under the impingement area in SiC-N ceramic recovered after interface defeat.

average particle size corresponds closely to the 4-μm average grain size of undamaged ceramic. Failure at grain boundaries is a characteristic of this SiC-N, and it contributes to the fracture toughness.

A tile of hot-pressed TiB_2 was also recovered from an improved target. A photograph of the sectioned tile is shown in figure 26. Major lateral cracks occurred in this ceramic, although they had no apparent influence on interface defeat. The source and timing of these lateral cracks is unknown, but they are suspected to have resulted either from small displacements (slippage of the core in the steel tube) or from secondary impacts after the conclusion of interface defeat. The other obvious difference between TiB_2 and SiC-N is the size of the microdamaged region. In TiB_2 , the microdamaged region has a width of ~10.5 mm, which is over 30% larger than the width in SiC-N.

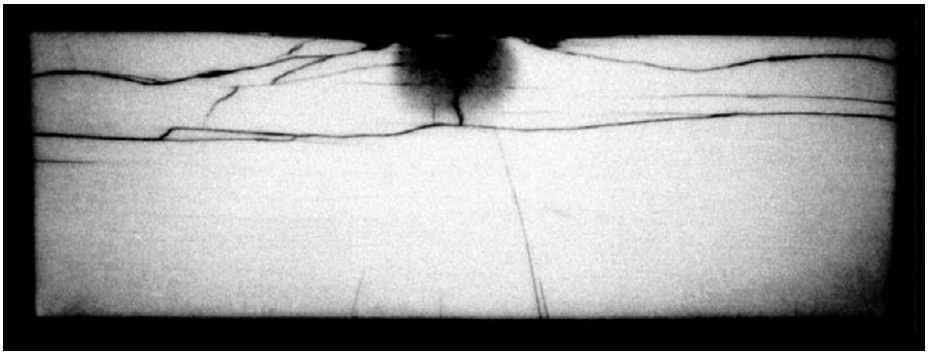

Figure 26. Recovered TiB_2 ceramic, cross-sectioned to show macrodamage and microdamage.

Microdamage in the recovered tile of TiB_2 is shown in the four panels, A to D, of figure 27. Panel A is an enlarged photographic view of the impingement area shown in figure 26. Panels B, C, and D are scanning electron microscope micrographs of the microdamage. Panel B is a view of the surface region where impingement occurred. Here, the surface is coated with projectile material which is almost completely devoid of the Ni-Fe matrix. Matrix metal may have been expelled during the pile-up and deformation of tungsten particles. Similar behavior was observed in figure 17, where radial flow was impeded. Panel C shows damage at 1 mm beneath the surface of the impingement area. Here, the porosity is predominantly associated with grain boundaries and triple points. Panel D, an observation at 5 mm beneath the surface, shows damage similar to that in panel C. Although the volume of microdamage in TiB_2 is relatively large, it is more uniform and less advanced than that observed in SiC-N.

One test with the hot-pressed Al_2O_3, type Ebon A, revealed damage more severe than that observed in either SiC-N or TiB_2. Unloading, at the conclusion of interface defeat, resulted in a large upward displacement of the impingement area. Lateral unloading cracks were primarily responsible for this displacement. However, the ceramic maintained interface flow which completely consumed the standard long-rod projectile launched at a velocity of 1606 m/s.

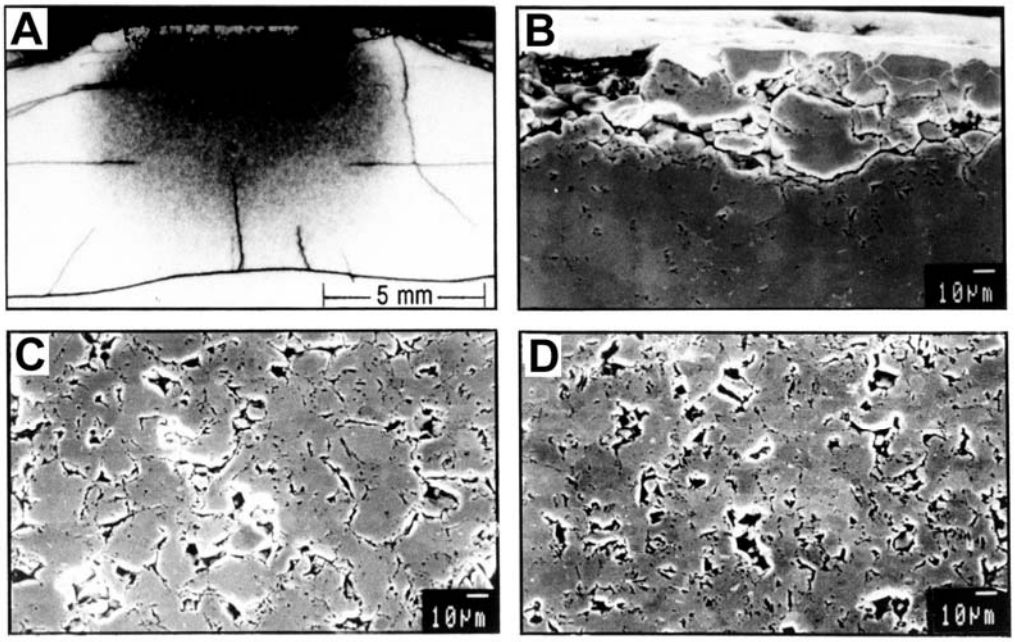

Figure 27. Microdamage in TiB_2 recovered after interface defeat.

Hot-pressed tungsten carbide (WC) with a purity exceeding 99%, made by CERCOM, Inc., was found to be the ceramic most resistant to damage during interface defeat. The recovered tile of WC is shown in figure 28. Panel A shows the tile surface. There is no obvious loss of material in the vicinity of the impingement area. However, a measurement of the surface profile in panel B reveals a 0.05-mm-deep depression in the impingement area, with a slightly deeper 0.10-mm depression around the margin. The cross-sectional view in panel C provides no evidence of the microdamage found under the impingement area in other ceramics. A few shallow ring cracks are the only evidence of impingement. The apparent absence of microdamage in WC is noteworthy. With other sources of damage effectively suppressed, there should be no mechanism for the displacement of WC and conventional penetration at a projectile velocity of 1600 m/s is prevented.

Hot-pressed boron carbide (B_4C) exhibited the worst ballistic performance of all ceramics tested at ordnance velocity conditions. An examination of the recovered target indicated only a brief interval of dwell and radial flow before the onset of penetration. A tile of B_4C, 25 mm thick, was easily perforated, with penetration well into the rear steel support.

4.5 Interface Flow Inferred From Recovered Heavy Targets

The improved heavy-target configuration for interface defeat was too massive to permit flash-radiographic observations of flow at the ceramic. However, scarring of the Cu interface layer provided indirect information about flow in the adjacent weak layer located at the front surface

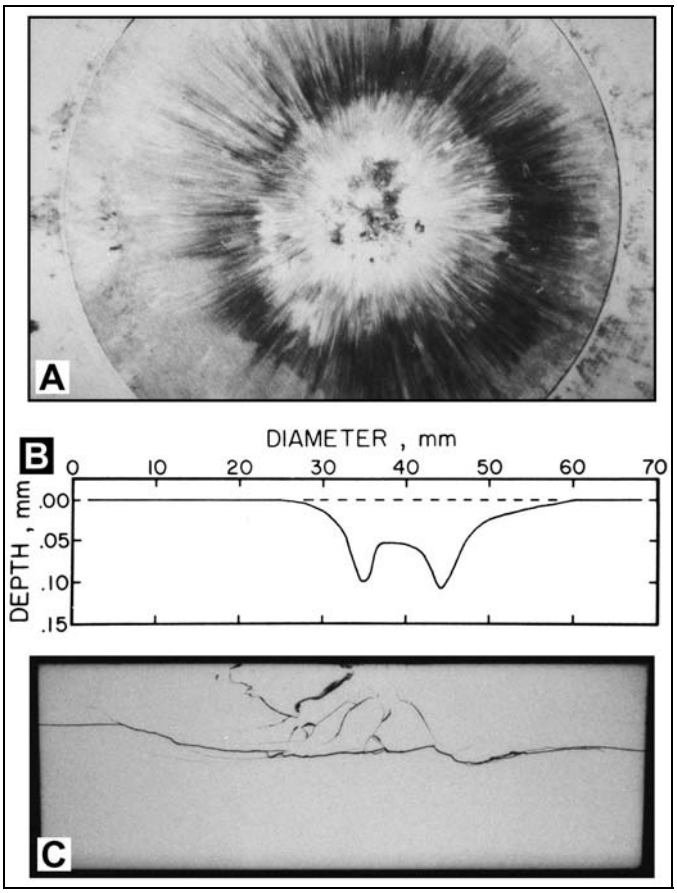

Figure 28. WC ceramic recovered after interface defeat: (a) the pattern of lateral flow, (b) the front surface profile, and (c) a cross-sectional view that shows macrodamage but no microdamage.

of the ceramic. Cu layers, recovered from targets with different ceramics, are shown in figure 29. These layers are ordered according to increasing quality of flow into the weak interface layer. In the top row, the ceramics were B_4C, Al_2O_3 (Ebon A), and SiC-N; in the lower row, the ceramics were TiB_2 , TiC, and WC. Flow into the weak interface layer improved in the listed order, from B_4C to WC.

Microdamaged material, under the impingement area in B_4C, must have been displaced quickly and easily. The resulting interface profile directed the flow of erosion products across the weak layer and into the Cu layer where flow was severely impeded. A resulting increase in stress should have contributed further to the displacement of microdamaged ceramic. Microdamage in TiB_2 was observed to be less advanced than microdamage in SiC-N, and this is consistent with the relative ordering of these two ceramics in figure 29. With the final ceramic, WC, flow was well-directed into the weak layer, leaving only grazing scars on the Cu plate. The direction of flow undoubtedly depends on both the compression of ceramic under the impingement area and

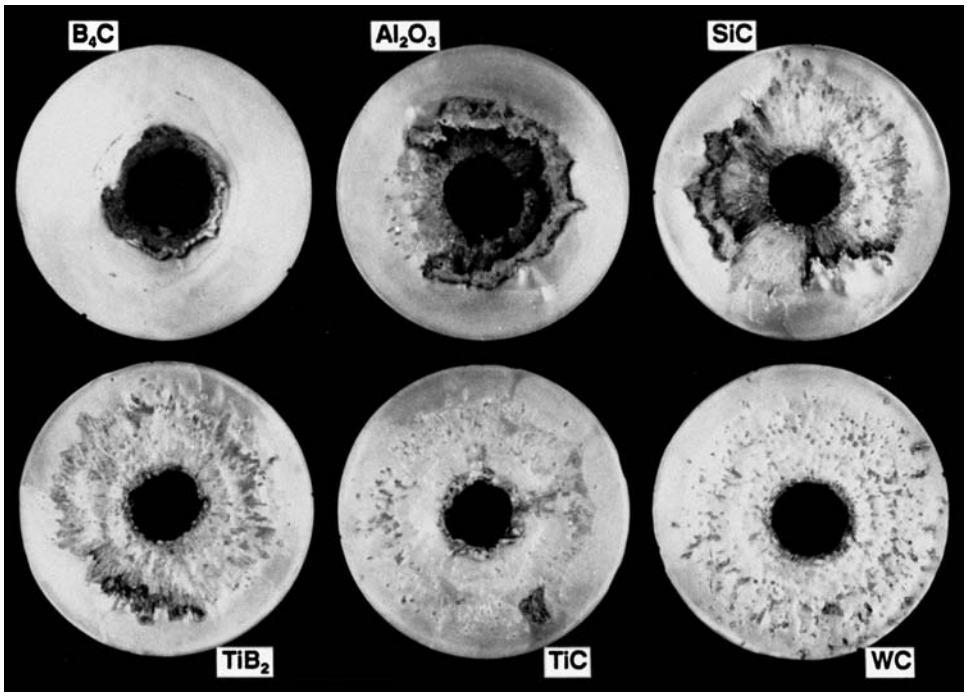

Figure 29. Cu layers recovered from targets that contained various ceramics, in order of increasing lateral flow of erosion products performance.

the displacement of damaged material. WC produced well-directed interface flow because it had the highest modulus of all ceramics which were evaluated, and also because it sustained no obvious microdamage. The available evidence suggests that stability of the microdamaged region is a major influence on interface flow and the resistance of the ceramic to penetration.

Some experiments were conducted to examine interface defeat of larger long-rod projectiles launched at velocities which exceeded 1600 m/s. Velocities from 1600 to 2000 m/s were achieved using a 40-mm powder gun which launched an X21 projectile with a diameter of 6.18 mm, an L/D ratio of 20, and a mass of ~65 g. The powder gun was also used for two series of experiments which compared behavior in ceramic targets attacked by 32.5-g long-rod projectiles of X21 tungsten alloy and depleted uranium (DU). These projectiles had an L/D ratio of 15 and diameters of 5.38 and 5.29 mm, respectively. The target design was the same as that shown in figure 23, but target dimensions were scaled to match the scale of the projectile. Experiments were conducted with both SiC-B and TiB_2 ceramics. A preliminary experiment with SiC-B, conducted at a velocity of 1626 m/s, closely duplicated the performance of SiC-N at the smaller scale. In the subsequent experiment with SiC-B, at a velocity of 1810 m/s, microdamaged ceramic was displaced and surrounding ceramic was excavated from an area that corresponded closely to the area of the hole through the Cu layer of the target. The ceramic, with a thickness of 38 mm, was not perforated, but damage was extensive. In experiments with TiB_2, interface defeat occurred at both 1781 m/s and 1970 m/s. However, as shown in figure 30, microdamaged ceramic was displaced along with surrounding material from an area which again

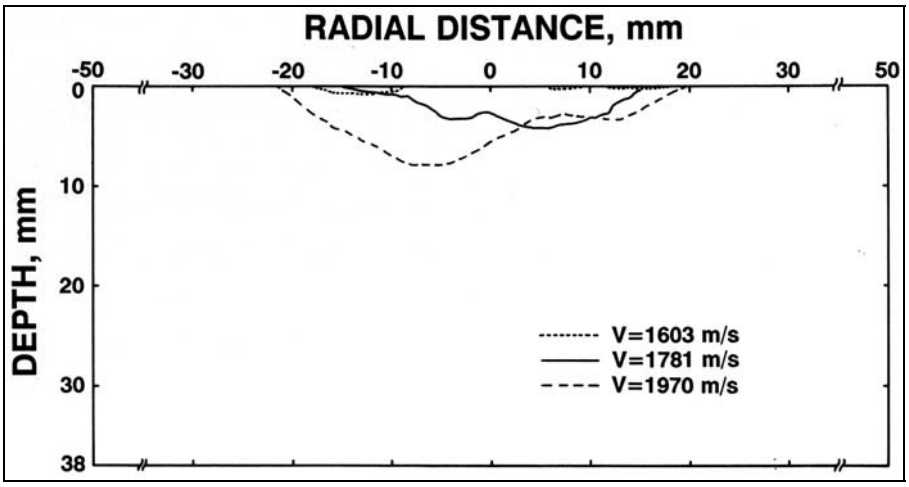

Figure 30. Damaged material displaced from TiB_2 ceramic by WHA long-rod projectiles impacting at velocities of 1603 m/s, 1781 m/s, and 1970 m/s.

corresponded closely to the area of the hole through the Cu layer of the target. The greatest displacement of material occurred at a velocity of 1970 m/s where the maximum depth was nearly 8 mm. Unlike SiC-B, the damage to TiB_2 was localized and flow returned to the weak interface layer of graphite at the front surface of the ceramic.

4.6 Summary of the Heavy-Target Results

The ordering in figure 29, and the behavior at velocities higher than 1600 m/s, suggested that the target in figure 23 might have a defect which has a pronounced influence on the performance of different ceramics, depending on their individual characteristics. Computer modeling suggests such a defect. Dehn (1995a) has reported computer modeling of interface defeat, and in a more recent study (Dehn 1995b), interface defeat was modeled in a target configuration similar to the one shown in figure 23. The resulting plot of pressure at the ceramic as a function of radial distance is shown in figure 31. This plot indicates a gap in support at the front surface of the ceramic. Central support extends only slightly beyond the radius of the impinging long-rod projectile, leaving a gap before pressure again increases in the weak layer. This gap suggests an interval where the ceramic is unsupported at the front surface. The performance of a particular ceramic probably depended on its ability to resist displacement at the gap in front-surface support. The radial extent of the gap in support, predicted by computer modeling, corresponds closely to the radius of the hole in Cu plates recovered from most targets. An obvious exception occurred with B_4C. However, with this ceramic, the hole in the Cu plate was enlarged by misdirected flow which was turned through an angle significantly larger than 90° as it left the impingement area. The need for a Cu layer to suppress shear failure was reevaluated. If a weak layer promotes radial flow at the surface of the ceramic, erosion products should never accumulate in a cavity, there is no cavity wall where shear failure can occur, so a layer of material (e.g., Cu) to suppress this mode of shear failure should be superfluous.

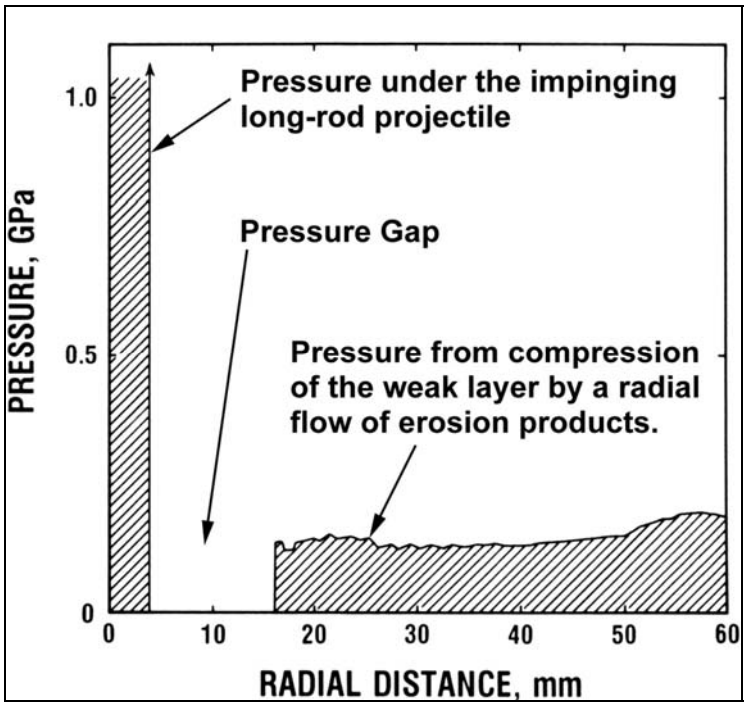

Figure 31. Computational modeling that reveals a gap in the interface pressure that supports the front of the ceramic.

The high mass of the heavy-target configuration was another concern. High mass was necessary to recover ceramic with minimal damage. However, high mass precluded a practical application as armor. Furthermore, there was concern that information about interface defeat in massive targets might not be relevant to applications of the interface defeat mechanism in lighter, more practical, armor configurations. High mass also precluded flash-radiographic observations which could provide time-resolved guidance to penetrator-target interactions. As a consequence of these concerns, the use of heavy targets was discontinued, with the exception of a few experiments when it was necessary to recover ceramic for special post-test evaluations.

5. Interface Defeat in Light-Target Configurations

5.1 Light Targets With Aluminum Confinement

The initial light-target configuration used confinement of high-strength aluminum alloy (AA7075-T6) and is shown in figure 32. TiB_2 was selected as the ceramic because earlier recovery experiments indicated superior interface flow, and static x-ray exposure tests confirmed that this ceramic was suitable for radiography. The target was assembled by two shrink fits, similar to the assembly of the target in figure 23. However, with AA7075-T6 alloy, the temperature for shrink fitting was limited to 300^{o} C. The target was attacked at 1600 m/s by an

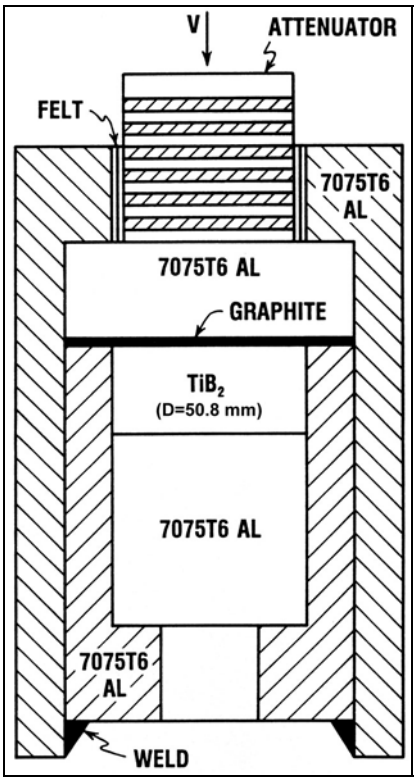

Figure 32. Light ceramic target utilizing Al confinement that was introduced for flash-radiographic studies of interface flow.

X21 WHA rod with a diameter of 4.93 mm and an L/D ratio of 20. The first radiograph from this experiment, recorded 6.8 μs after impingement on the ceramic, is shown in figure 33. Erosion products prevent a clear observation of the forward portion of the rod, except on the right side near the impingement area. Here, the radiograph shows a sharp turn as rod material flows into the interface layer, in agreement with the behavior implied by Dehn's computer modeling. Compression of ceramic under the impingement area tends to direct the flow at an angle slightly larger than 90°, but there is no evidence that the flow is impeded. At the time of this first radiograph, there also is no evidence that microdamaged ceramic is being displaced at the predicted gap in front-surface support. The second radiograph (not shown) was recorded 35 μs later. By the time of the second radiograph, the weak aluminum confinement had failed or sufficiently degraded, allowing a radial displacement of ceramic and the onset of penetration.

5.1.1 SiC-B Ceramic Attacked by WHA Rods

SiC-B was also used in aluminum confinement for flash-radiographic observations of interface flow. Tests were conducted with WHA long-rod projectiles which were launched from a powder gun at a nominal velocity of 1600 m/s. The flow patterns from earlier experiments with steel

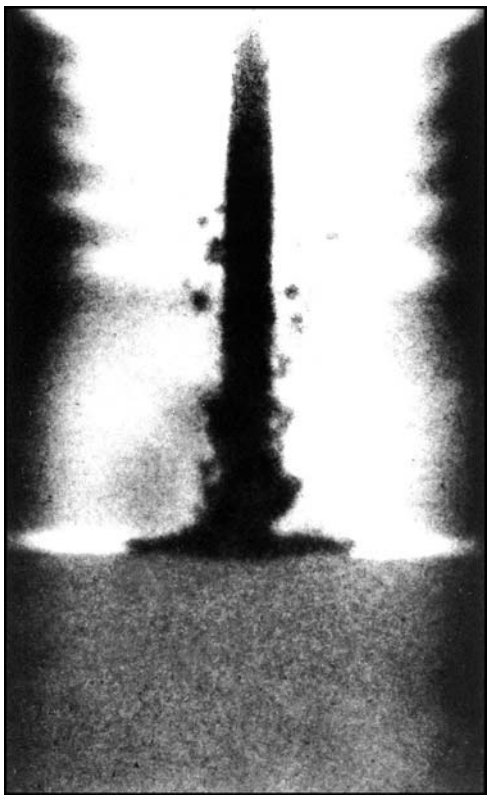

Figure 33. Flash-radiographic observations of the flow of a WHA rod projectile attacking a TiB_2 ceramic with Al confinement.

confinement, shown in figure 29, suggested that the interface flow at SiC-B is not as well-directed as the interface flow at TiB_2. This observation is supported by the radiographs from experiments with WHA projectiles, as shown in figure 34. Interface flow at SiC-B ceramic, which was marginal with steel confinement, has degraded further with aluminum confinement. At 5.5 μs after the rod arrives at the SiC-B, flow is directed across the weak layer of graphite and into the front confinement of aluminum. At 7.7 μs (in a subsequent experiment), the flow continues to be misdirected. In addition, microdamaged ceramic is being displaced, allowing the onset of penetration. Penetration is actually occurring at 5.5 μs, but it is more obvious at 7.7 μs. With the configuration in figure 23, and its steel confinement, penetration was not encountered with similar ceramic at the same projectile velocity. There is no computer modeling for a target with aluminum confinement, but the diameter of the penetration path through the front confinement of AA7075-T6 aluminum is 2.3 times the diameter of the penetrator, so a gap in the support at the front of the ceramic is inferred. In addition, the poorly directed and impeded interface flow should cause an increase of stress in the impingement area, and this should contribute to the displacement of microdamaged ceramic.

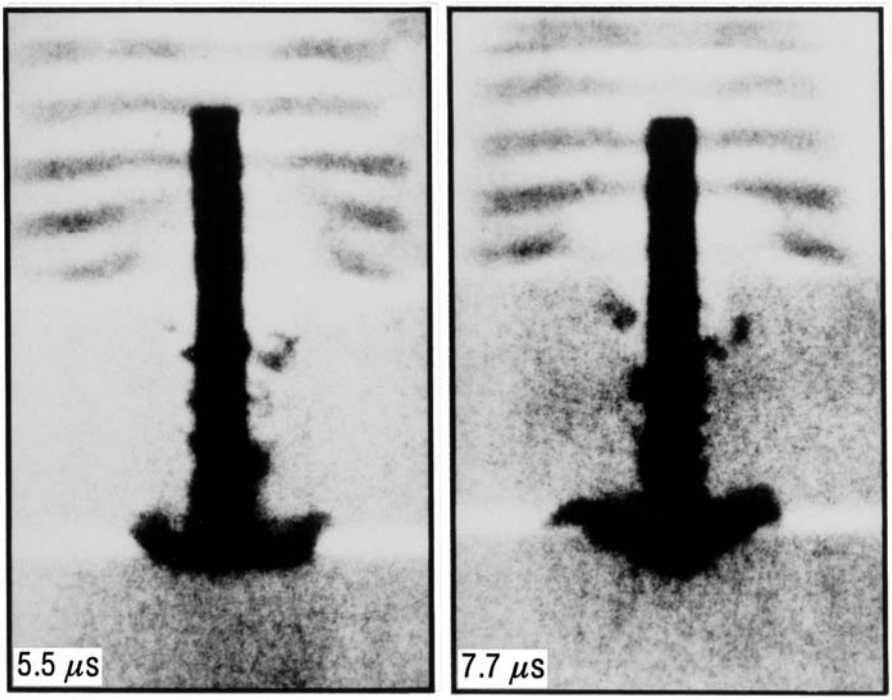

Figure 34. Flash-radiographic observations of the flow of a WHA rod projectile attacking a SiC-B ceramic with Al confinement.

5.1.2 Light-Gas Gun Experiments With SiC-B Ceramic

Experiments conducted with a light-gas gun also provided evidence of a support gap around the impingement area in targets with aluminum confinement. An experimental arrangement for launching WHA long-rod projectiles from a light-gas gun with a 100-mm bore is shown schematically in figure 35. During launch, the projectile is supported in the sabot by ceramic microballoons and epoxy with a density of 0.8 g/cm^3. Some of the low-density supporting material accompanies the rod through the inertial sabot stripper and onto the target. If clearance at the stripper hole is not minimized, the extraneous material provides critical support around the area where the projectile impinges on the ceramic. With a marginal ceramic such as SiC-B, this critical support prevents microdamaged ceramic from being displaced to allow penetration. However, if radial clearance at the stripper is reduced to ~1.0 mm, the reduced amount of extraneous material does not contribute enough support within the gap and SiC-B ceramic is penetrated. The gap in support, predicted by computer modeling, is a real factor which must be considered when selecting front confinement for a ceramic.

5.1.3 SiC-B Ceramic Attacked by DU Rods

Additional experiments with SiC-B in AA7075-T6 confinement were conducted with long-rod projectiles of DU launched at a nominal velocity of 1600 m/s. Radiographs from these experiments are shown in figure 36. At 6.3 μs after the DU rod arrives at the SiC-B, flow is

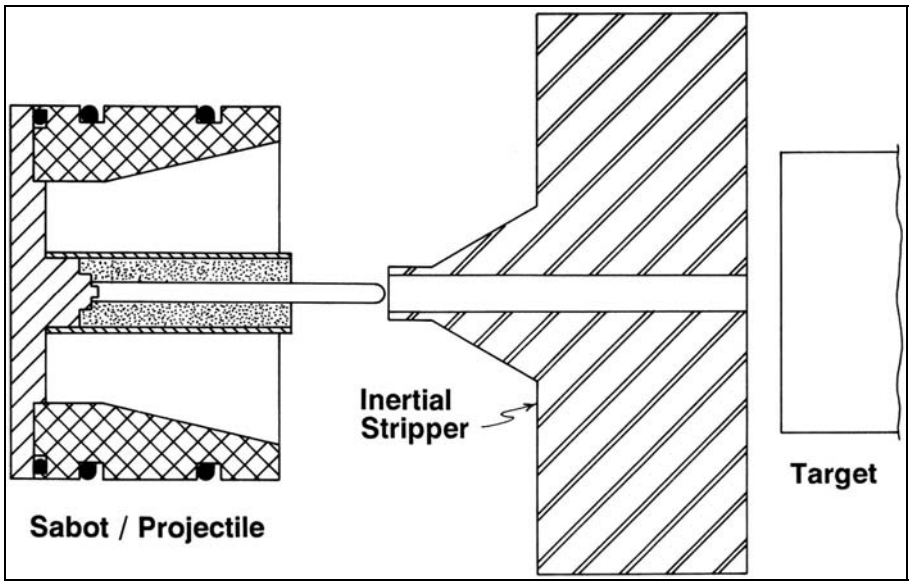

Figure 35. Sabot configuration used to launch long-rod projectiles with 100-mm bore light-gas gun.

clearly directed across the weak interface layer. However, by 7.9 μs (in a subsequent experiment), flow into the interface layer has improved. This suggests that the shear failure of DU results in more efficient flow into the weak layer intended to accommodate it. Although penetration into the SiC-B is occurring, the DOP is significantly less than the DOP by a WHA rod at nearly the same time. This behavior is consistent with a lower central stress which should result from the less impeded flow of DU erosion products.

5.1.4 Ebon A Ceramic Attacked Obliquely by a DU Rod

Any practical application of interface defeat would undoubtedly involve oblique attacks. A final experiment in the series with aluminum confinement was conducted as an introduction to behavior during an oblique attack. The experimental target was assembled from readily available components. The ceramic was Ebon A, 102 × 152 × 25 mm thick. Front confinement of AA7075-T6 aluminum had the same dimensions. A recess, 75 mm in diameter and 1.57 mm deep, was machined into the rear surface of the front plate to accommodate a weak layer of graphite. A plate of RHA, 102 × 152 × 50 mm thick, served as rear support for the Ebon A. An attenuator, similar to the one shown in figure 32, was bonded to the front of the target. Layers of the target were held together only by interface bonds of epoxy. The ceramic layer was not confined at the side, which precluded any long-term resistance to penetration. This target was inclined at 45° and attacked by a long DU rod launched at a velocity of 1632 m/s. Previously (see figure 29), the interface flow of WHA erosion products at Ebon A was found to be more poorly directed than the flow at SiC. DU was selected as the projectile material for the oblique attack because its flow characteristics were found to be superior to those of WHA.

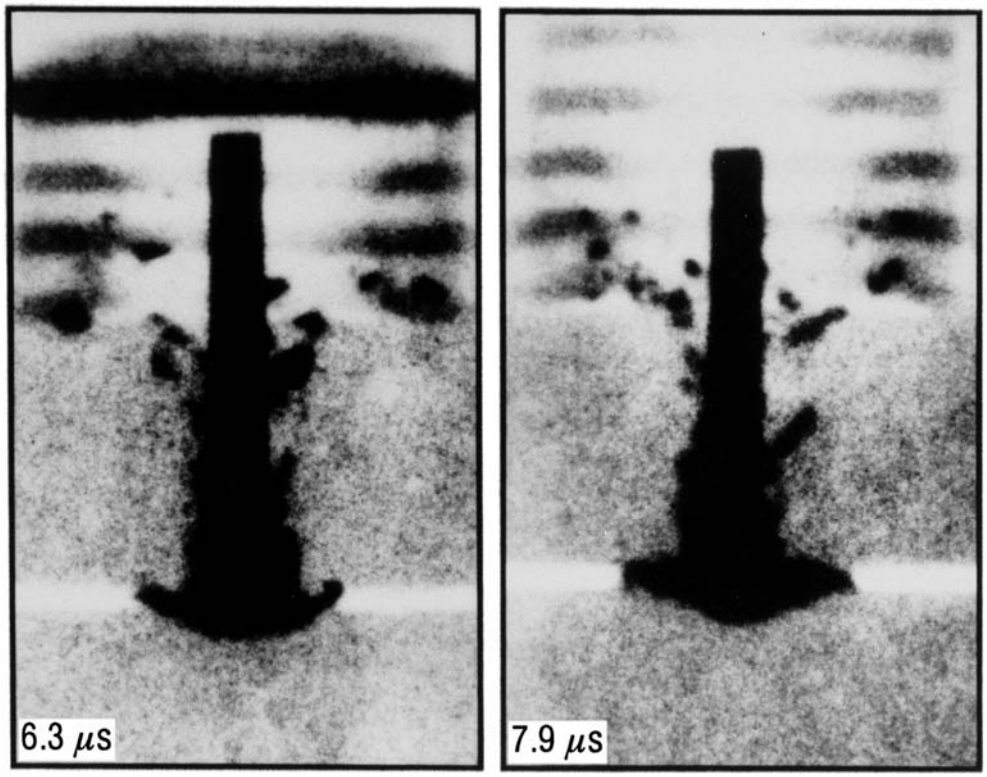

Figure 36. Flash-radiographic observations of the flow of a DU rod projectile attacking a SiC-B ceramic with Al confinement.

The flash radiograph from the experiment at 45° obliquity, taken 19.5 μs after the DU rod arrived at the ceramic, is shown in figure 37. A casual inspection suggests total defeat at the interface, but this is not the true behavior. A slight darkening under the impingement area is actually penetration into the ceramic. Two obvious factors could contribute to penetration. First, the location of eroded penetrator material indicates a large gap around the penetrator on the upper (downstream) side, where microdamaged ceramic could be displaced. Second, radial cracks could arrive at the unconfined side boundary of the ceramic 5 μs before the time of the radiograph in figure 37, and this could contribute to degradation of the ceramic and subsequent penetration. In addition, the system was held together only by epoxy bonds which provided no significant constraint. Despite these problems, there is a major branch of flow into the interface layer at the surface of the ceramic. Ebon A, which previously displayed marginal interface defeat during an attack at normal incidence, displays unusually good short-term performance during the attack at 45° obliquity. The excellent flow characteristics of DU undoubtedly contributed to the good short-term performance. In addition, there is the tendency for erosion products to be directed preferentially to the specific area of the ceramic where stress is needed for support. The reason for this remains to be investigated.

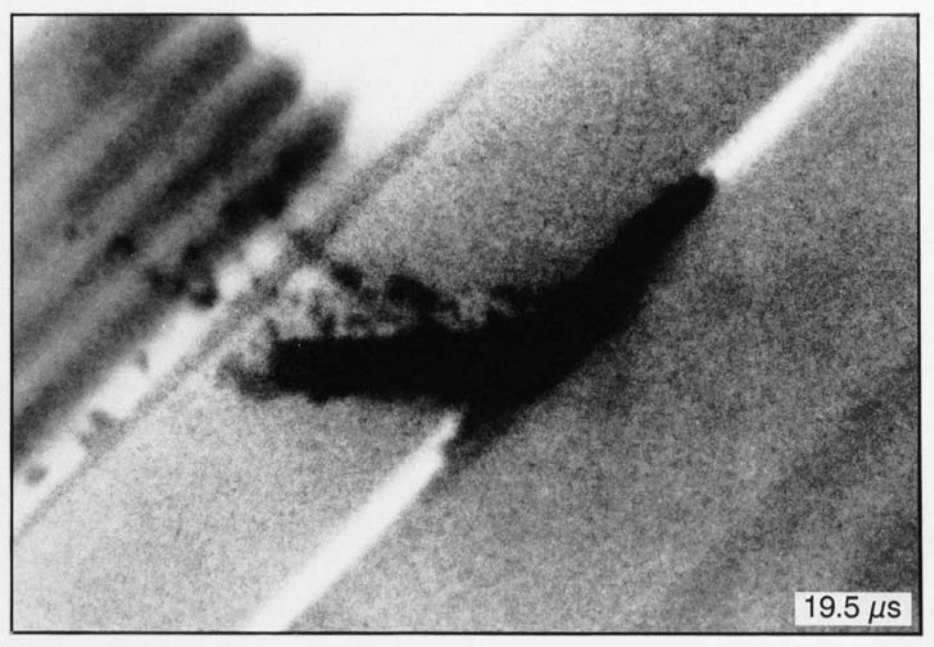

Figure 37. Flash-radiographic observations of the flow of a DU rod projectile attacking a Ebon A Al_2O_3 ceramic with Al confinement.

5.1.5 Influence of Obliquity on Microdamage

Two recovery experiments were also conducted to explore the benefits of obliquity on the performance of a ceramic. The targets for these experiments provided improved support for the ceramic and were similar to the target configuration in figure 23, but with a modified front to permit unobstructed attack at obliquities of 45° and 60°. The ceramic for these experiments was SiC-B, which provided the assessment of damage at normal incidence for SiC-N shown in figure 24. Impact velocities were nominally 1600 m/s, and the attenuator and front confinement were modified at each obliquity to maintain a constant line-of-sight areal density, providing essentially the same impact velocity as the attacking WHA rod arrived at the ceramic. Comparisons of internal damage at obliquities 0°, 45°, and 60° are shown in figure 38. The volume of microdamage is significantly reduced at 45°, and no microdamage is detected at 60°. It is apparent that microdamage diminishes as the normal component of velocity decreases with increasing obliquity. This suggests that penetration, which can depend on the displacement of microdamaged ceramic, becomes more difficult at higher obliquities. This also implies that obliquity could contribute to the interface defeat of long-rod projectiles arriving with velocities higher than 1600 m/s.

5.2 Light Targets With Titanium Confinement

Aluminum confinement permitted flash-radiographic studies but lacked the strength needed for adequate support of a ceramic. Steel confinement offered the strength needed for adequate confinement but did not permit flash-radiographic observations of behavior during interface

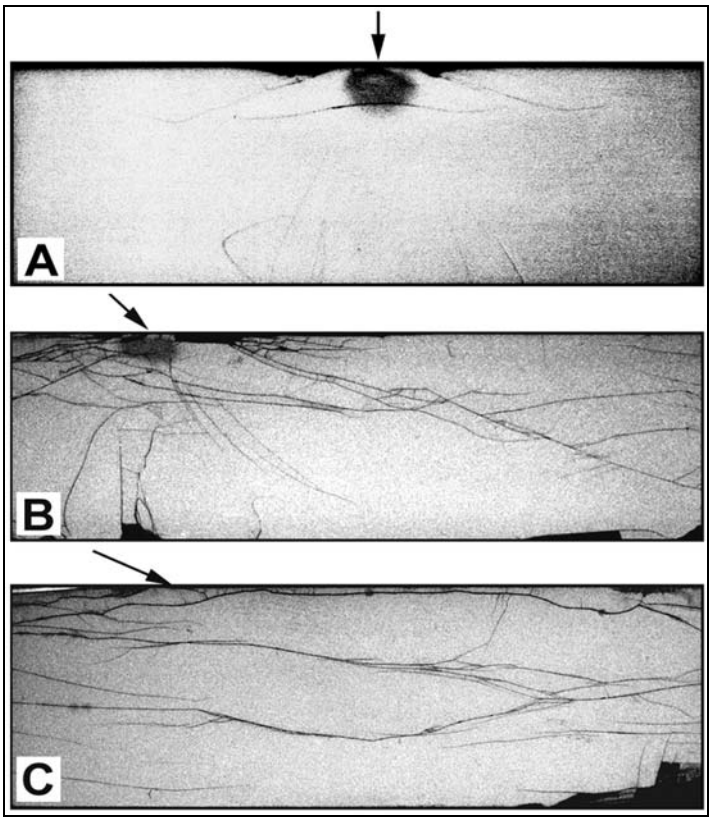

Figure 38. Influence of impact obliquity on microdamage in SiC. NATO angles of obliquity are (a) 0°, (b) 45°, and (c) 60°.

defeat at the scale of interest. Titanium offered the strength needed to confine a ceramic, and preliminary tests established the usefulness of megavolt flash radiography. With Kodak Lanex Fast-Back Intensifying Screens and TMH Film, megavolt flash radiography permitted observations through 115–125 mm of titanium alloy (Ti-6Al-4V) which confined TiB_2 ceramic with a diameter of 72 mm.

5.2.1 The Support Gap as a Design Consideration

Evidence suggested that the support gap (section 4.6) should be influenced by the diameter of the penetration path through the front confinement. Figure 39 presents data for (path diameter /projectile diameter) as a function of the attack velocity. Data for RHA (Silsby, 1984) serve as a reference. Data from interface defeat experiments, with AISI 4340 steel (HRC45) as the front confinement, lie below the reference curve. Data for front confinement of AA7075-T6 aluminum lie above the reference curve. The relative locations probably explain why a marginal ceramic such as SiC-B resists penetration with AISI4340 steel as front confinement, while it is penetrated when the front confinement is aluminum. A single datum point for Ti-6Al-4V lies close to the curve for AISI 4340 steel, which makes it a promising candidate for front confinement in ceramic targets.

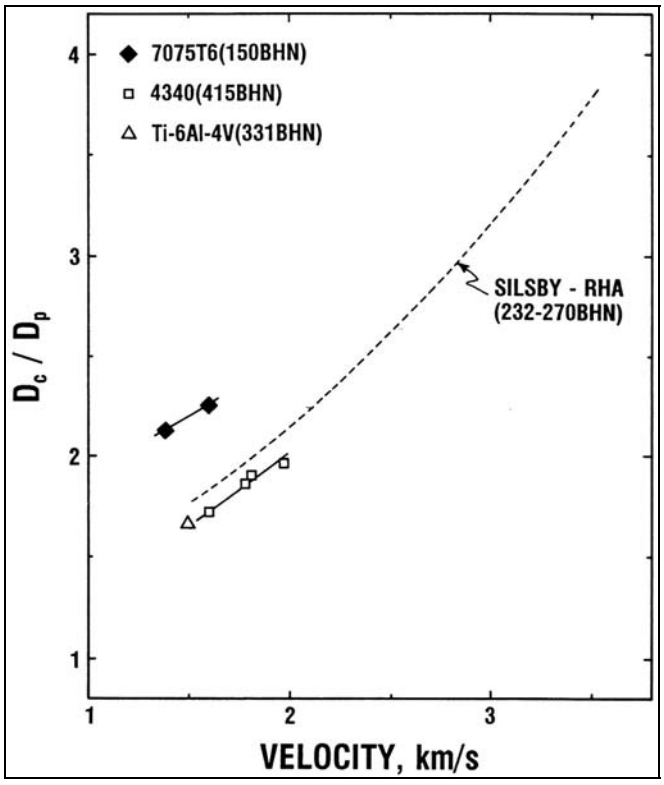

Figure 39. Penetration path diameter normalized by penetrator diameter as a function of impact velocity.

5.2.2 Influence of Attack Velocity

The trend of available data suggests that the gap in support at the front of a ceramic should increase as the attack velocity increases, making it more difficult to achieve interface defeat at high velocities. Also, more advanced levels of microdamage would be anticipated at higher velocities, and an increased gap width should make it easier for the microdamaged material to be displaced. However, the possibility of compensating response by titanium should be explored. For example, flash-radiographic studies and recovered targets suggest that titanium alloy may offer support for a ceramic which is superior to the support offered by steel. As shown in figure 40, Ti-6Al-4V tends to undergo shear failure at the maximum gradient in the velocity field that surrounds a penetrating long-rod projectile. Even with incipient shear, as shown in figure 40a, material enclosed by the somewhat irregular boundary of primary shear is observed to undergo secondary shear failure and displacement, producing closure of the penetration path.

The secondary shear and path closure are shown more clearly in figure 40b, where primary shear is fully developed. In this example, some of the blocks formed by secondary shear were lost from the target during the recovery process. At velocities of 1500 to 1600 m/s, path closure should be a relatively slow process. However, even at these velocities, there is evidence that the

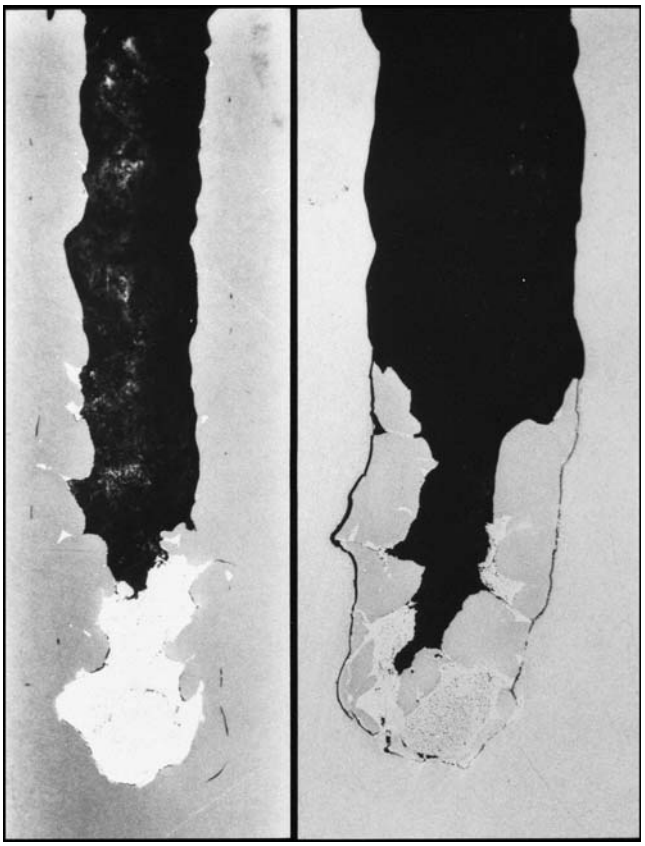

Figure 40. Ti-6Al-4V targets cross-sectioned to show (a) incipient shear, and (b) fully-developed shear with interior blocks formed by secondary shear.

primary shear occurs quickly enough for some influence within a few microseconds. For example, with relatively thin (12.7-mm thickness) front confinement of Ti-6Al-4V, figure 41 shows that primary shear occurs quickly enough to block the lateral flow of erosion products on one side of the penetration path. This blockage was observed only with a weak layer which had a thickness in the order of 0.1 mm, and such blockage would not occur with the thicker interface layer used for interface defeat. However, the example does offer guidance to the time at which shear would begin to influence closure. At higher velocities, the penetration path in Ti-6Al-4V should widen, but the shear process that produces closure of the penetration path should occur more quickly, possibly compensating and minimizing the gap in support at the front surface of a confined ceramic. This is an area that should benefit from further study.

5.2.3 Initial Light Target With Titanium Confinement

Figure 42 shows the initial target configuration for flash-radiographic studies of interface defeat using titanium confinement. The Ti-6Al-4V front plate had a nominal thickness of 50 mm, but machining operations to accommodate the ceramic and the weak interface layer reduced the front confinement to an actual thickness of 19–20 mm. The thickness of the Ti-6Al-4V back plate

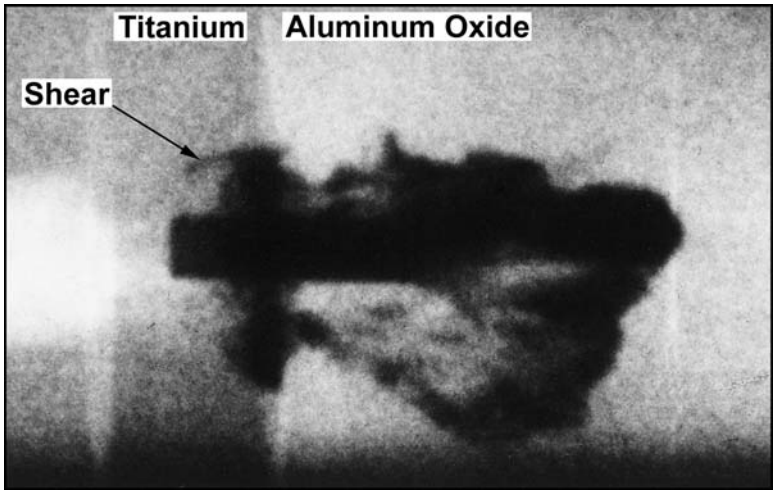

Figure 41. Flash radiograph that shows the radial flow of eroded projectile material impeded by primary shear in the Ti-6Al-4V front confinement.

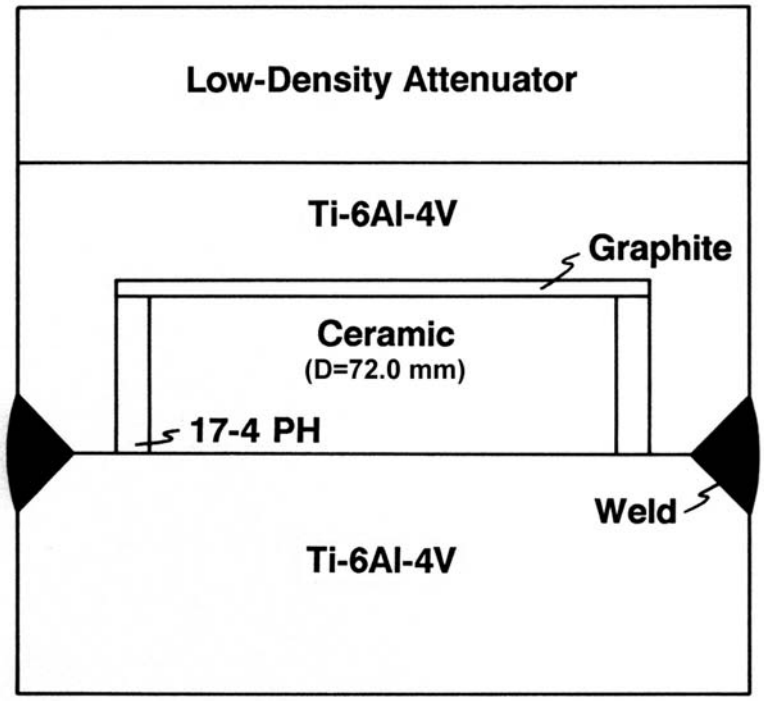

Figure 42. Light ceramic target utilizing Ti-6Al-4V confinement that was introduced for flash-radiographic studies of interface flow.

was varied from 25 to 57 mm in different experiments. TiB_2 ceramic, used in most of the experiments, was 72 mm in diameter and ~25 mm in thickness. The ceramic was prestressed by a tube of 17−4 PH steel with a wall thickness of 5 mm and an inside diameter initially 0.13 mm less than the diameter of the ceramic. The steel sleeve was heated to 480° C to accommodate the ceramic. Next, the graphite interface layer was placed in the Ti-6Al-4V front plate and the

prestressed ceramic was installed using a second shrink fit. For this installation, the titanium was heated in argon (Ar) to the aging temperature of 538° C. The interface layer between the titanium front and the ceramic was varied in several experiments. These variations indicated that with graphite as the weak layer; a layer thickness of 2.38 mm resulted in less ceramic damage than the initial layer thickness of 1.59 mm. Experiments also confirmed that it is not necessary to include a second interface layer; such as Cu, to prevent shear failure of the front confinement from impeding the flow of eroded projectile material into the weak layer. The two parts of the Ti-6Al-4V confinement were joined by standard metal-inert-gas (mig) welding, using Ti welding wire, and Ar as the shielding gas. Finally, a layered attenuator was installed at the front surface. The design of this attenuator differed from the previous design. It was composed of a 6.3 mm-thick Coors Porous Plate and 31 alternating layers of low-density polyethylene (LDPE) and Al, all joined by interface layers of 3M "Scotch" Brand 568 Positionable Mounting Adhesive. The LDPE layers each had a thickness of 0.57 mm, and the Al layers each had a thickness of 0.52 mm.

5.2.4 Interface-Defeat Experiment at 45° Obliquity

Figure 43 is a flash radiograph that shows the target in figure 42 as it was attacked at 45° obliquity by the standard X21 WHA projectile, 4.93 mm in diameter, with L/D = 20, launched at a velocity of 1600 m/s. Thin lead (Pb) radiation filters were added at the side of targets in an effort to equalize the film exposure from different levels of radiation through different target layers. Three film/intensifying-screen units were also sandwiched into each cassette, providing three levels of film exposure. Eventually, two or three of the film records from an experiment were stacked in registration to increase the contrast of radiographic images. The stacked films were used to make a photographic print with high contrast, further improving the image. Finally, the printed image was digitally scanned, and an image processing program was used to enhance image areas for greater clarity. The radiograph in figure 43 is a typical result of this image treatment, and it shows the projectile when it was 78% consumed. At this time, the tip of the interface flow is just beyond the limit of the image area. Unlike the radiograph in figure 37, the location of erosion products in the front confinement indicates a very narrow gap between the cavity wall and the top (downstream) side of the projectile. Also, there is no evidence of either penetration or loss of any material from the ceramic surface. After later experiments with thinner back plates, the excellent interface flow in this experiment was recognized to correlate with the thick (57-mm thickness) Ti-6Al-4V backing.

5.2.5 Ceramic Damage

The recovered target of figure 43 was radiographed to provide an initial assessment of the internal condition; this radiograph is shown in figure 44. The loss of damaged ceramic is evident, as is the full accumulation of eroded projectile material at the far right side of the interface. Damage to the ceramic is a consequence of internal stress associated with the flow of

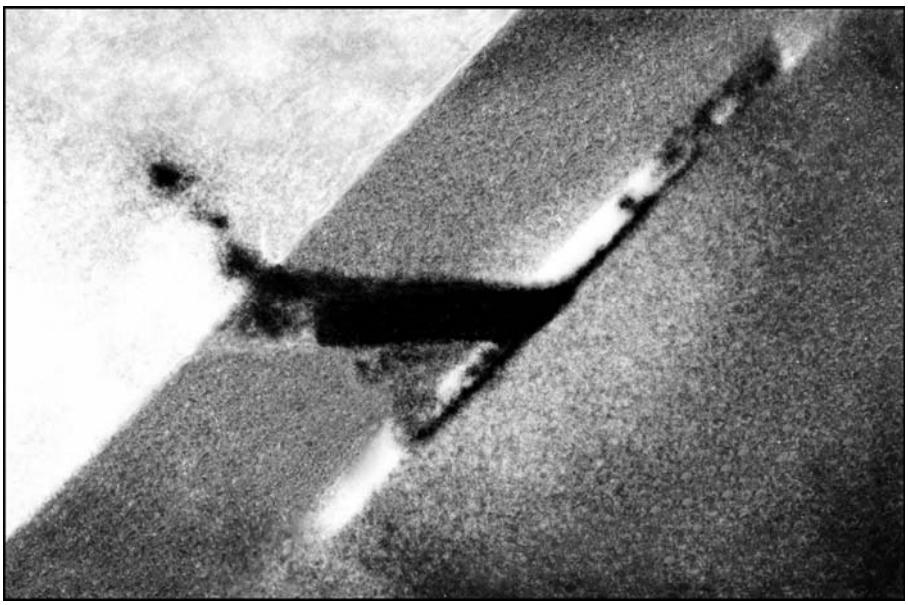

Figure 43. Flash radiograph that shows interface defeat of WHA rod projectile obliquely attacking TiB_2 ceramic confined by Ti-6Al-4V.

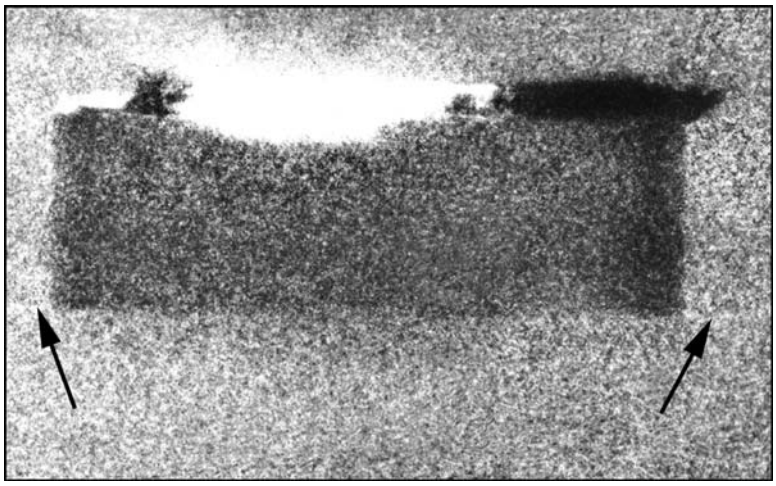

Figure 44. Post-test (static) radiograph revealing damage in TiB_2 ceramic that only becomes evident after the projectile is fully consumed; that is, after front surface support has ceased.

erosion products which compress the weak layer. As interface stress increases, the front and back plates of the target bulge. The front plate, which is much thinner, bulges more than the back plate. The ceramic, held in the front plate by a shrink fit, is lifted away from the back plate as the front plate bulges. Arrows in figure 44 point to the small gap that is faintly visible between the front and back plates of Ti-6Al-4V. On the upstream side of the entrance hole, where interface stress is a minimum, the ceramic remains separated from the back plate. On the downstream side of the entrance hole, the flow of erosion products increases stress in the weak

interface layer and the ceramic is forced back into contact with the back plate. This action bends and damages the ceramic. With TiB_2 ceramic, used in most of the experiments, damage is never apparent while eroded projectile material flows into the graphite layer, maintaining an interface stress that supports the damaged ceramic. After an experiment, when the interface stress has been relieved, damaged, fully-comminuted ceramic can be poured from the entrance hole, leaving the void evident in the post-test radiograph.

5.2.6 Influence of the Ceramic

The target configuration in figure 42 was tolerated differently by different ceramics. For example, a 13-mm thickness of WC was severely degraded by macrodamage and penetrated. In the target configuration of figure 23, where macrodamage was negligible, WC was judged to be the ceramic most resistant to penetration because no microdamage was found and there seemed to be no mechanism for penetration at an attack velocity of 1600 m/s. Such conflicting results raise concern about some experiments conducted to "rank" the ballistic performance of ceramics. A ranking may not be reliable if the target configuration for ranking provides support for the ceramic that is different from the support that will eventually be present in a practical armor configuration.

5.3 Improved Light Target With Titanium Alloy Confinement

Macrodamage encountered with the light target configuration in figure 42 was reduced by moving the ceramic to the back part of the target, as shown in figure 45. In this location, interface stress always presses the ceramic against its rear support. Ceramic in the improved configuration was usually prestressed in either of two ways: (1) by shrink-fitting into a 5-mm-thick tube of 17−4PH steel, which subsequently was shrink-fitted into the Ti-6Al-4V, or (2) by shrink-fitting directly into the Ti-6Al-4V. The choice had little, if any, influence on the ballistic performance, but an intermediate tube of 17−4PH steel facilitated removal of the ceramic from a recovered target. The weak layer of graphite initially had a thickness of 2.38 mm, and this layer remained recessed in the front confinement. In this location, stress that developed within the graphite layer could not effectively act against the lateral confinement to relieve the initial prestressed state of the ceramic. Thickness of the front Ti-6Al-4V confinement was initially 23 mm, while the thickness of rear Ti-6Al-4V confinement in different experiments was varied from 38 to 19 mm. In later experiments, thickness of the front confinement was also reduced. Experiments were again conducted with the standard X21 WHA projectile, 4.93 mm in diameter, with L/D = 20, launched at a velocity of ~1600 m/s.

5.3.1 Initial Experiment With the Improved Light Target

Figure 46 shows the flash radiograph from the initial experiment in which the improved target configuration was attacked at 45° obliquity. In this target, the 25-mm thickness of TiB_2 was supported at the rear by a 9.5-mm thickness of AISI4340 steel. The steel was ground to provide

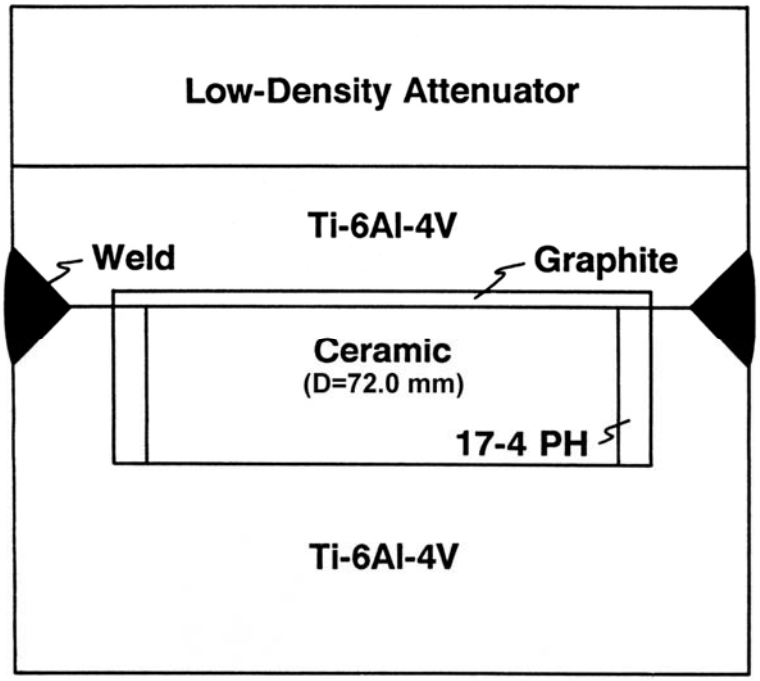

Figure 45. Improved light ceramic target utilizing Ti-6Al-4V confinement.

better coupling than was possible with the machined finish on the bottom of the cavity in the rear plate of Ti-6Al-4V. However, the presence of the steel reduced the back titanium to a thickness of ~22 mm. The interface flow in figure 46 is actually inferior to the flow observed in figure 43. In the downstream direction, the flows are equivalent, but on the upstream side, flow from the impingement area invades the family of cone cracks (labeled *CU*). The upstream and downstream cone cracks (labeled *CU* and *CD*, respectively) are identified in figure 47, which shows the cross section of a ceramic with stiffer support which was essential for the experiment which was intended to recover ceramic for post-test examination. Later, it will be apparent that the ability of erosion products to invade the upstream cone cracks correlates with thickness of the back titanium. (A 57-mm thickness of Ti-6Al-4V backing explains the excellent upstream flow observed in the weak layer of figure 43.) The surface of the recovered ceramic is shown in figure 48. Here, a vertical arrow identifies the downstream direction of flow from the impingement area. Label *D* identifies the 5-mm-deep excavation of ceramic from the invaded cone cracks on the upstream side of the impingement area. Label *L* identifies the limits to which the flow spreads and scours the surface of the ceramic. Areas of surface flaking (label *F*) are also identified. The absence of surface markings and perturbed flow at the areas of flaking in figure 48 suggests that these areas were supported and remained in place until the completion of interface defeat. Figure 49 shows a corresponding view of the graphite cavity in the front confinement, with residual graphite removed. Interface flow has sheared away the wall of the cavity on the downstream side, and areas of complete shear (labed *CS*) and partial shear

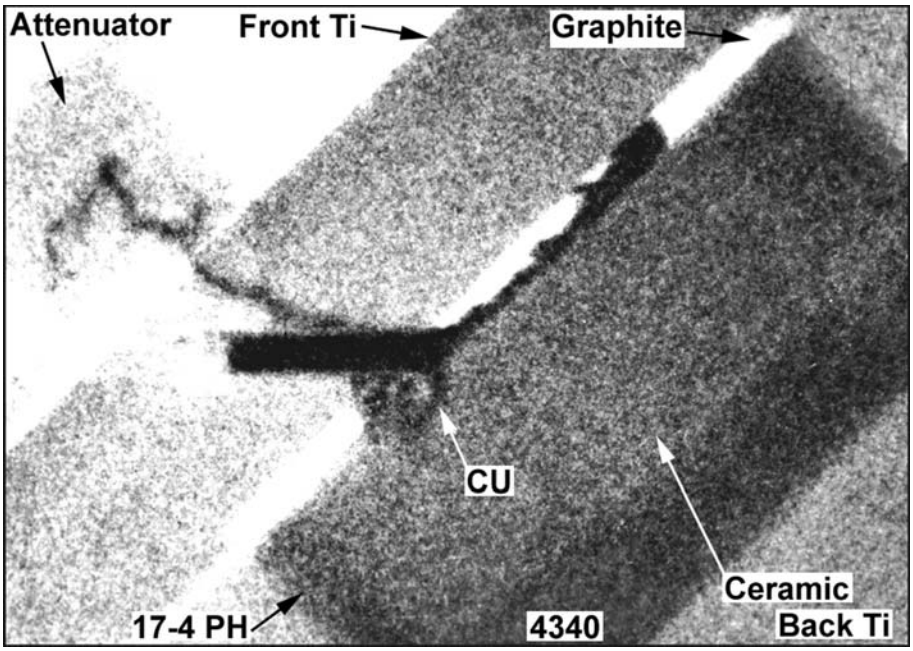

Figure 46. Flash radiograph of an experiment in which TiB_2 ceramic with AISI4340 steel backing was shrink-fitted into the general target configuration of figure 45, but where the Ti-6Al-4V thickness was reduced by the steel thickness.

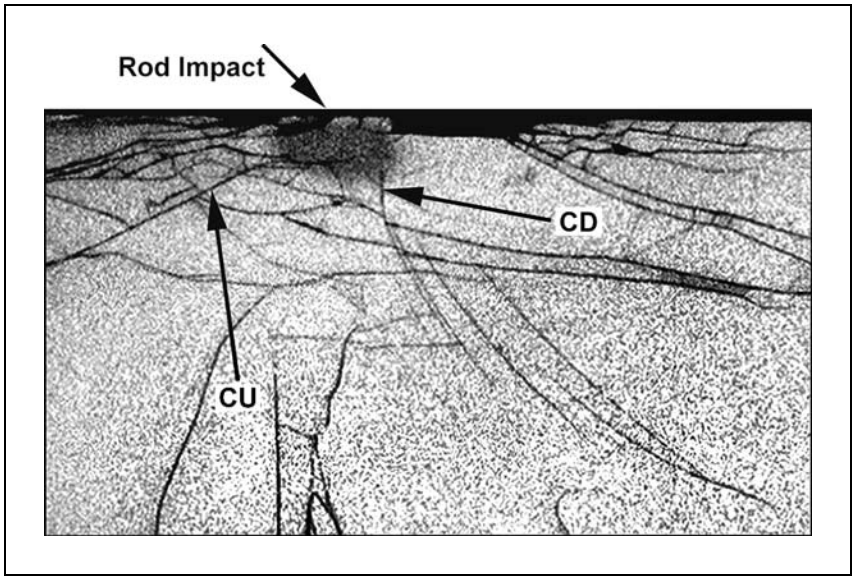

Figure 47. A portion of figure 38(b) showing cracks that influence the flow of erosion products from the impingement area.

(label *PS*) are identified. Deposits of fused erosion products have accumulated in the constricted area where the metal-metal (Ti-alloy) interface and the weld had to be forced apart to allow further flow of the erosion products.

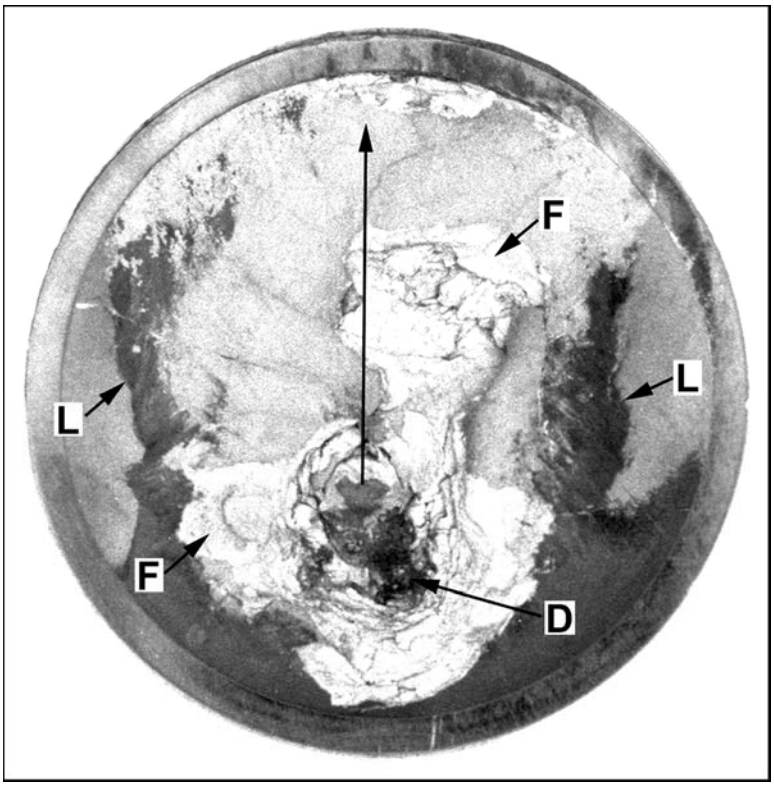

Figure 48. Surface of the ceramic tile recovered from the experiment depicted in figure 46.

5.3.2 Light Target Variations

Variations of the light target configuration in figure 45 were examined to determine the influence on interface defeat. When the AISI4340 steel was removed from behind the TiB_2 ceramic, the thickness of the titanium backing was increased to ~32 mm and interface flow improved in the upstream direction, as shown by the radiograph in figure 50. The surface of the ceramic, pictured in figure 51, shows that flow at the upstream side of the impingement area has invaded cone cracks and excavated ceramic to a depth of only 1 mm. With well-directed flow away from the impingement area, the flow pattern has spread to wider limits than the flow pattern in figure 48. The flash radiograph in figure 52 shows that no significant change in the character of interface flow results from eliminating the tube of 17-4 PH steel and shrink-fitting the TiB_2 ceramic directly into the rear Ti-6Al-4V. The flash radiograph in figure 53 shows that the depth to which erosion products invade the cone cracks on the upstream side of the impingement area increases when the thickness of the rear Ti-6Al-4V is reduced from 32 to 19 mm. Recovered ceramic from the target with 19-mm-thick Ti-6Al-4V backing is shown in figure 54. Erosion products were found to a depth of ~6.5 mm on the upstream side. However, as internal stress increased with downstream flow into the graphite, the backing bulged, which damaged the ceramic. The comminuted material fell from the recovered target when it was opened, resulting in a maximum downstream excavation of 11 mm.

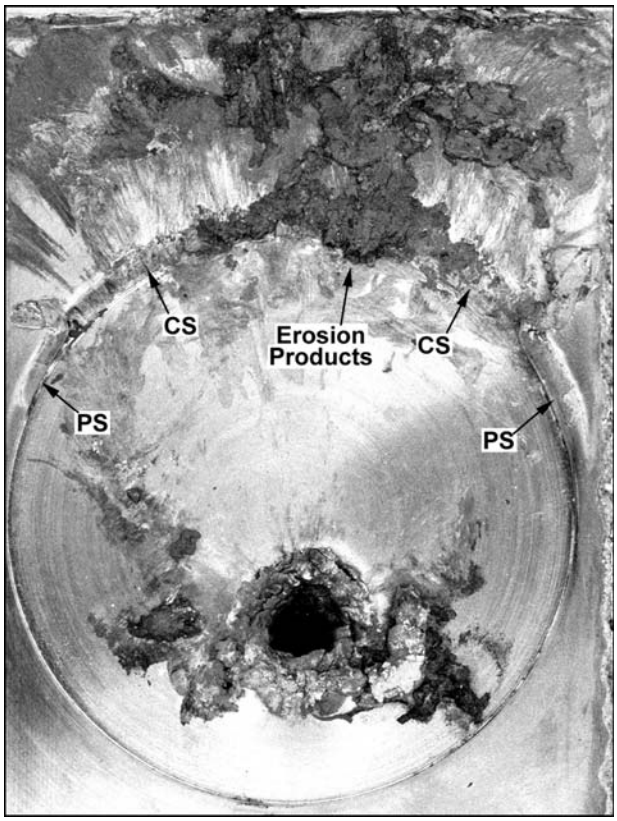

Figure 49. Graphite weak layer cavity recovered from the experiment depicted in figure 46.

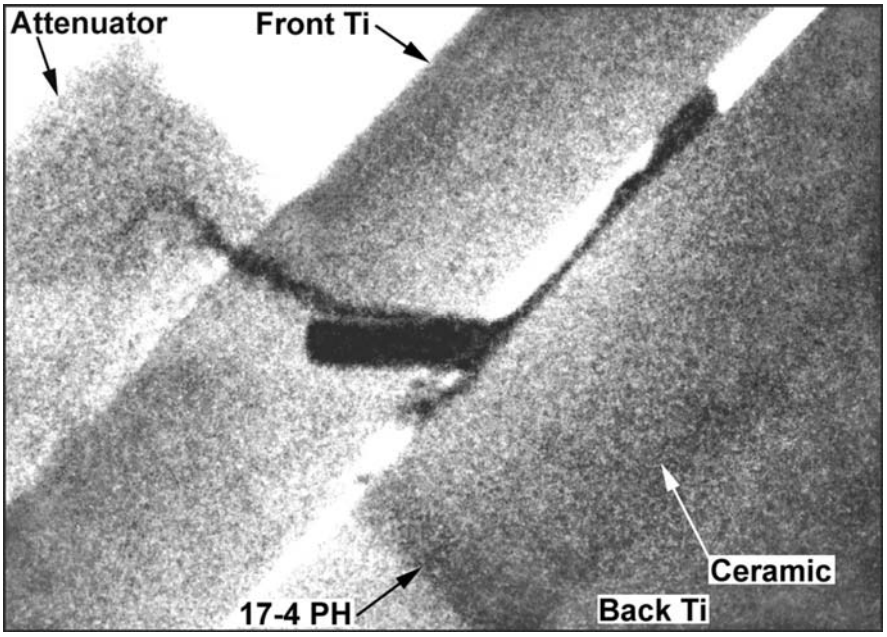

Figure 50. Flash radiograph of an experiment in which TiB_2 ceramic was shrink-fitted into the target configuration of figure 45.

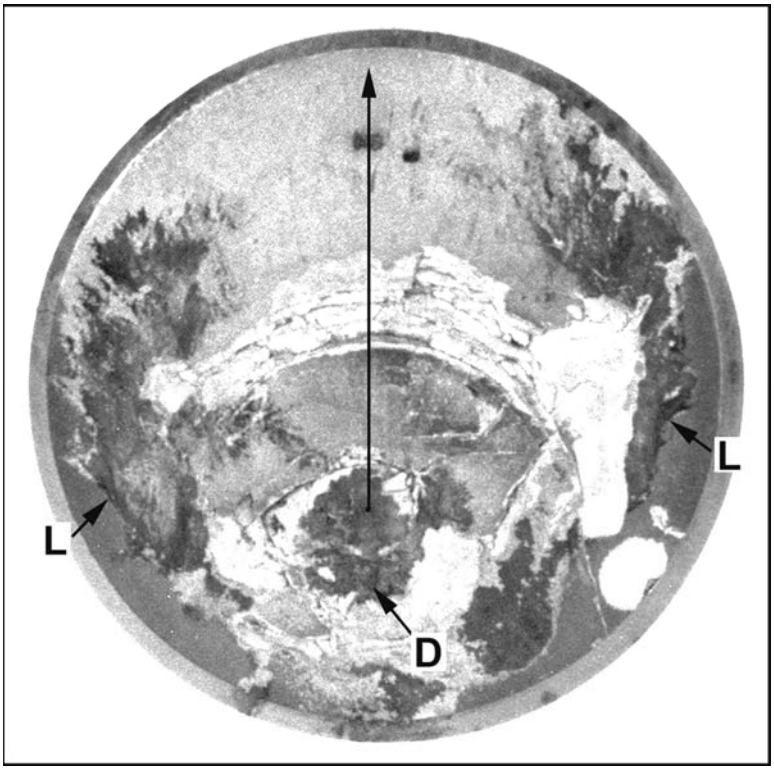

Figure 51. Surface of the ceramic tile recovered from the experiment depicted in figure 50.

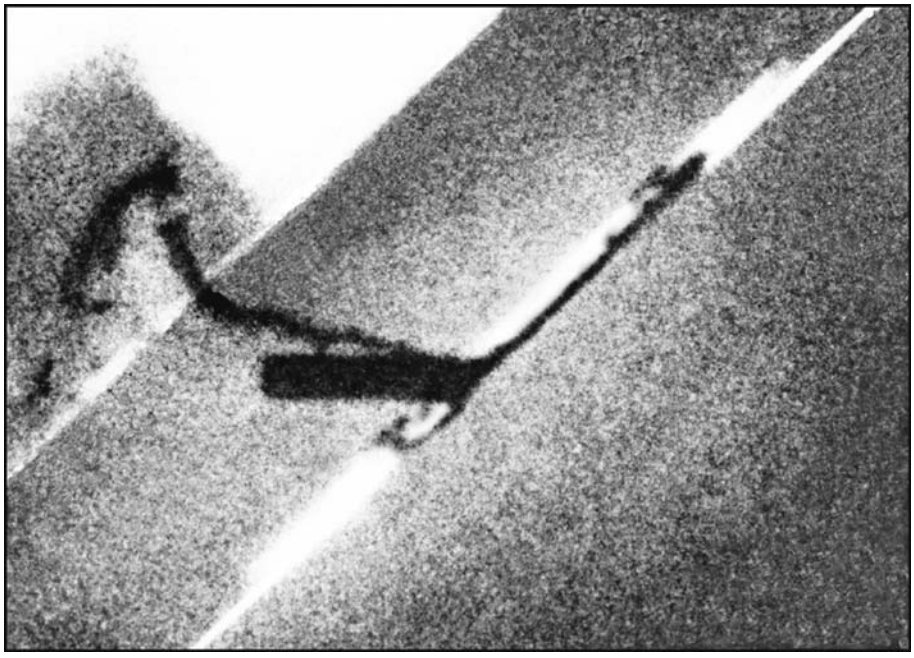

Figure 52. Flash radiograph of an experiment in which TiB_2 ceramic was shrink-fitted directly into Ti-6Al-4V, in the target configuration of figure 45.

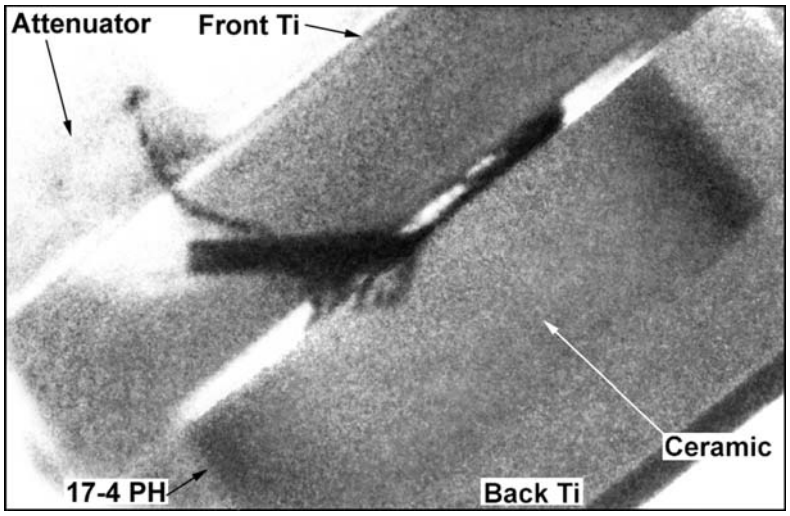

Figure 53. Flash radiograph of an experiment in which TiB_2 ceramic was shrink-fitted into the general target configuration of figure 45, but with reduced thickness of rear confinement.

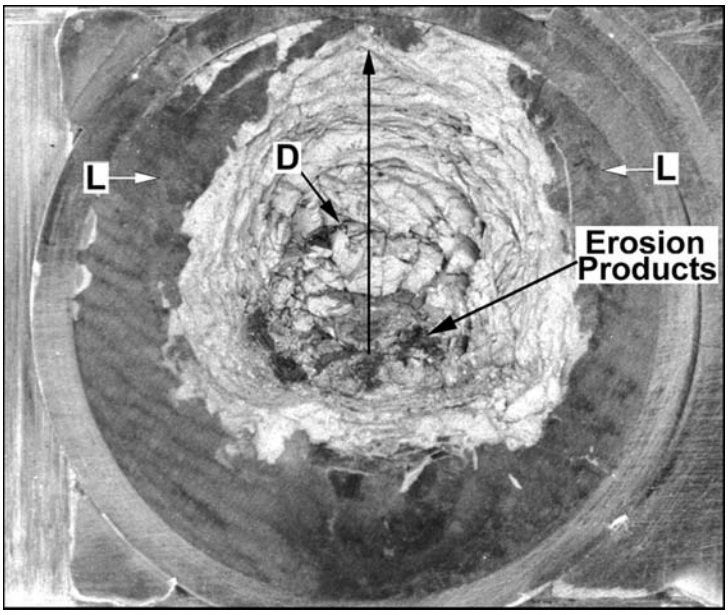

Figure 54. Ceramic tile recovered from the experiment depicted in figure 53.

In one final variation of the initial series of experiments, the thickness of TiB_2 was reduced from 25 to 19 mm, and it was shrink-fitted directly into Ti-6Al-4V, which provided back support with a thickness of 19 mm. In this experiment, the thickness of front Ti-6Al-4V was reduced from 23 to 10 mm, which reduced the maximum interface stress by allowing more bulging of the front confinement. This experiment produced the degraded interface flow shown in the radiograph of figure 55. However, an inspection of the radiograph that preceded the experiment, shown in figure 56, revealed a gap between the ceramic and the back titanium. Stress in the graphite layer quickly displaced the ceramic to close the gap. The resulting damage to the ceramic, and

additional damage from subsequent bulging of the titanium back support, accounts for the loss of ceramic shown in figure 57. The greatest loss of ceramic was to a depth of 15 mm. However, the deepest invasion of erosion products was to a depth of 7 mm, or 2 mm beyond the depth at the time of the radiograph in figure 55. The pretest gap has closed by the time of the radiograph, which means that this contribution to the damage has already occurred. From the radiograph, it is apparent that interface stress supports the damaged ceramic, allowing full-term interface defeat. Figure 58 shows the graphite cavity of the recovered target, with residual graphite removed for a better view of the flow pattern. The flow has not been influenced significantly by the misdirected flow shown in figure 55. However, there is a full accumulation of erosion products within the cavity area, with only minor invasion into the Ti-Ti interface near the edge. This degree of containment is explained by increased deformation of the thinner front confinement, as shown in figure 59. There is progressive bulging as interface stress increases in the downstream direction, terminating at a shear failure with a maximum offset of 5 mm. It is evident that the interface defeat mechanism is very tolerant of damage to the ceramic because interface stress supports the damaged ceramic. The obvious goal is to identify the minimum stress needed for effective support, and to provide front confinement that does not fail catastrophically at this stress. This, in turn, should allow the rear support to be minimized. The final target of this short series, with a line-of-sight areal density of 35.3 g/cm^2, was suspected to be close to the optimum for this threat projectile. However, a target with a 20% lower areal density and no gap behind the ceramic easily defeated the standard long-rod projectile launched at 1590 m/s. There is a clear requirement for systematic experiments to optimize the design of armor systems for interface defeat.

5.3.3 Asymmetrical Rod Erosion at Obliquity

When Ti-6Al-4V is penetrated at normal incidence, the erosion products tend to surround and obscure a penetrating long-rod projectile of WHA, as shown by the radiograph in figure 60. However, at 45° obliquity the early flow of erosion products in Ti-6Al-4V front confinement is from the downstream/downslope side of the rod tip, as shown in figures 45, 46, 50, 52, 53, and 55. As a consequence, the entire length of rod is unusually visible in megavolt radiographs. During oblique penetration into thicker Ti-6Al-4V, figure 61 shows that tip erosion begins to regain symmetry after penetration of about 4.5 rod-diameters DOP. However, flow from the downstream side persists for thicknesses of Ti-6Al-4V that are practical for front confinement of a ceramic target. In practical ceramic armor modules, this implies a negligible gap between the rod and the cavity wall on the upstream side. A relatively narrow gap on the downstream side is also apparent from the location of erosion products within the front-plate thickness of targets tested at obliquity. The preferential erosion favors an efficient transition of flow into the weak interface layer, and flow moves toward the interface area where support is most needed to keep damaged ceramic from being displaced. Flow behavior, together with reduced microdamage at obliquity, seem to explain the benefit of obliquity in interface defeat at the ceramic layer of a target.

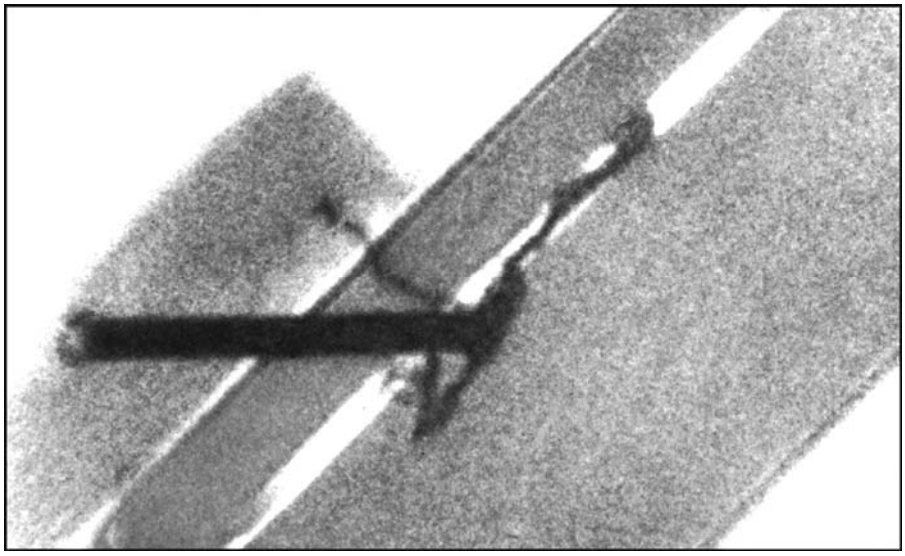

Figure 55. Flash radiograph of an experiment in which TiB_2 ceramic had reduced Ti-6Al-4V confinement at both front and rear.

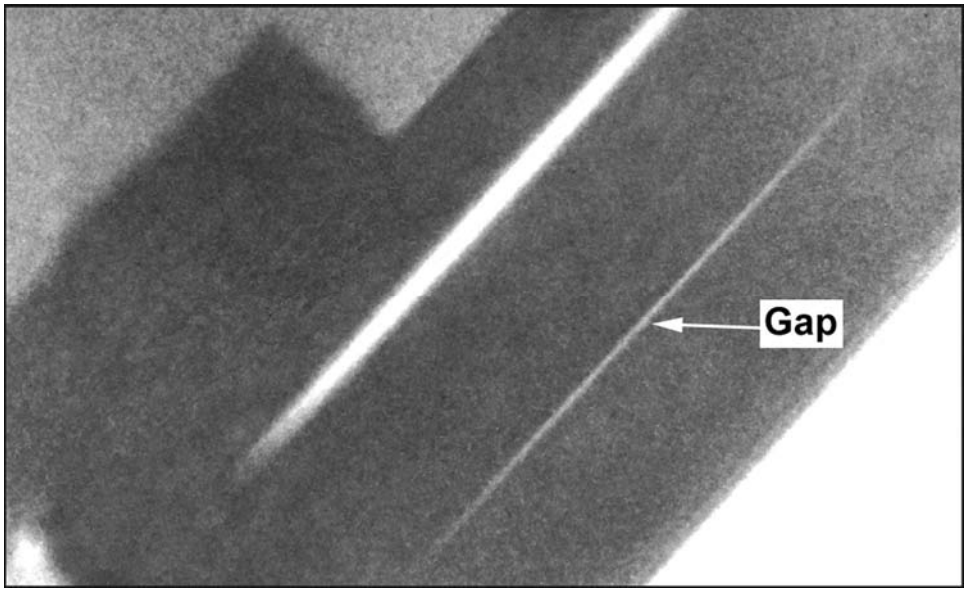

Figure 56. Pre-test (static) radiograph of the target depicted in figure 55 revealing the presence of a gap at the rear of the TiB_2 ceramic that reduced the rear support which contributed to the damage of the ceramic.

5.3.4 Influence of Scale on Interface Defeat at Obliquity

Ceramic targets with Ti-6Al-4V confinement performed well in the initial laboratory experiments at obliquity. However, it was important to establish the effectiveness of interface defeat at a scale where the mechanism might find practical applications. A scaled-up version (nominally 2X geometric scaling) of the target in figure 45 is shown in figure 62. The

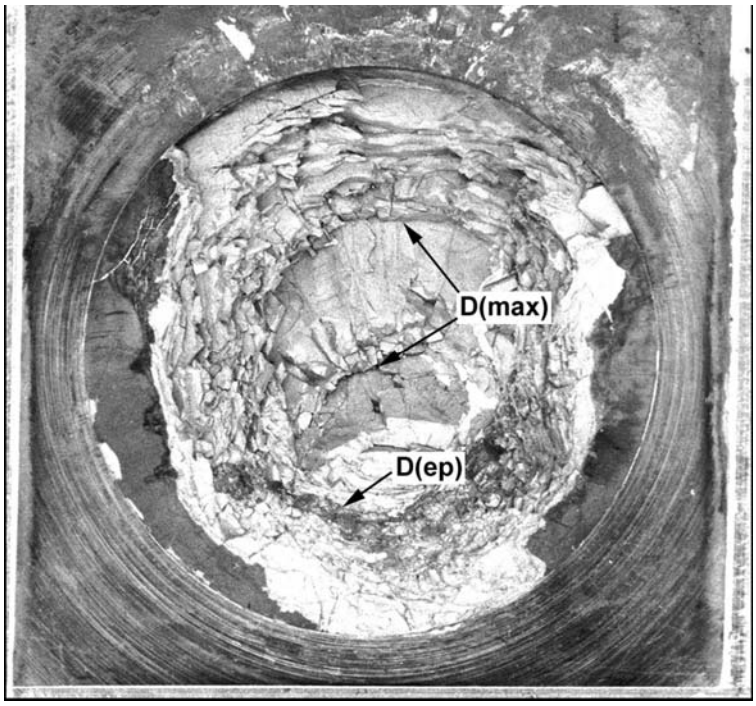

Figure 57. Ceramic tile recovered from the experiment depicted in figure 55.

Figure 58. Graphite weak layer cavity recovered from the experiment depicted in figure 55, showing that reduced frontal support and increased ceramic damage did not significantly alter the flow of erosion products.

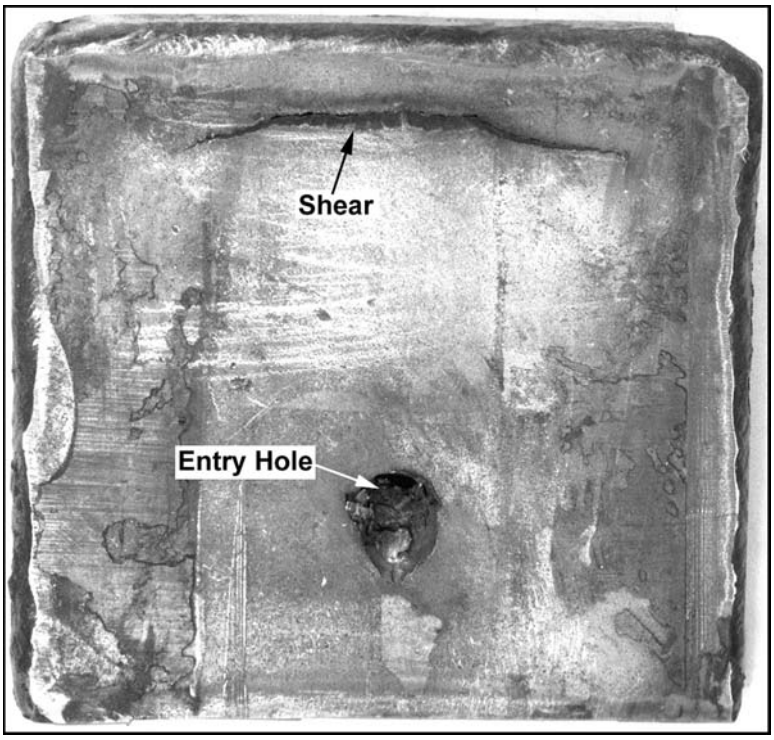

Figure 59. Ti-6Al-4V front confinement from the experiment depicted in figure 55, showing the shear failure that accommodated the erosion products depicted in figure 58.

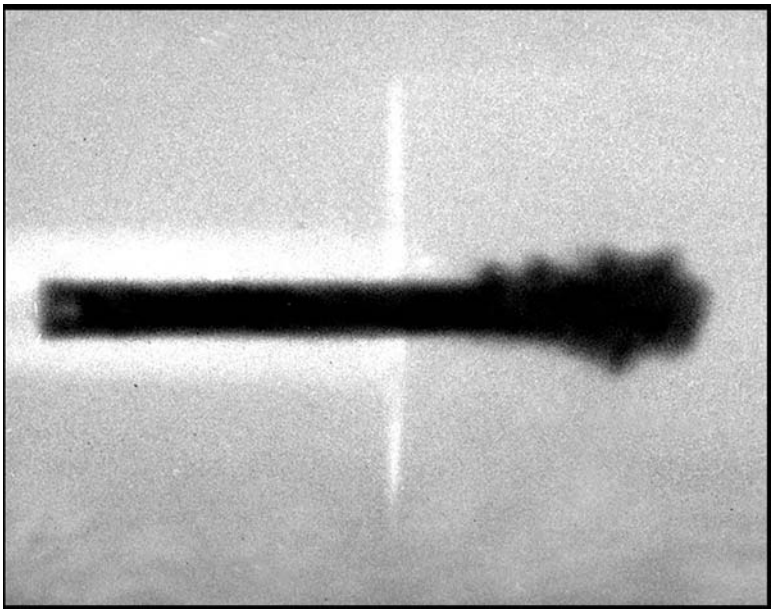

Figure 60. Flash radiograph showing the symmetrical flow of erosion products from a WHA rod projectile attacking thick Ti-6Al-4V at normal incidence.

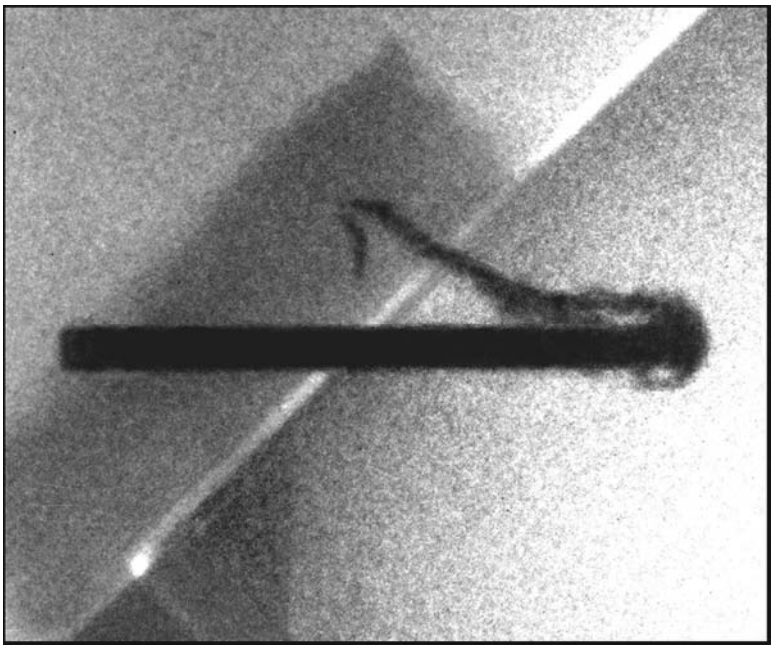

Figure 61. Flash radiograph showing the asymmetrical flow of erosion products from a WHA rod projectile attacking thick Ti-6Al-4V at 45° obliquity.

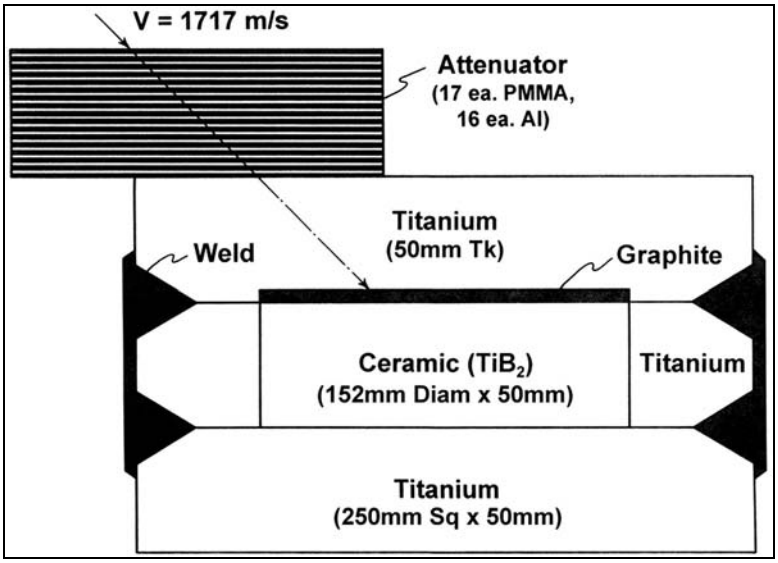

Figure 62. Larger-scale target configuration for oblique impact interface defeat.

configuration in figure 62, with three layers and two welds, is inherently weaker than the configuration in figure 45. However, variations of the smaller target showed insensitivity to ceramic damage, so the larger target was judged to have a good chance of performing well. The scaled-up target was built and then tested with a 263-g WHA rod (L/D = 20, L = 190.5 mm) launched at a velocity of 1717 m/s. The target easily defeated the rod which attacked at an

obliquity of 45°. The recovered target, shown in figures 63–67, displayed response similar to that of the smaller targets tested at the nominal velocity near 1600 m/s. Figure 63 shows the full target, as recovered. The graphite cavity, shown in figure 64, displayed flow and shearing at the cavity wall that is similar to what was observed with smaller targets. The downstream end of the target, shown in figure 65, displays similar bulging of the front plate, caused by erosion products forcing open the Ti-Ti interface. The loss of damaged material from the surface of the ceramic in figure 66 is similar to the loss of damaged ceramic in figure 54. The 18 mm-deep excavation on the upstream side of the impingement area is slightly deeper than the scaled loss from smaller targets, and this may relate either to the higher attack velocity or to the repetitive impacts of buttress threads present only on the larger projectile. Ceramic on the downstream side of the impingement area would have remained in place during the interface defeat, judging by radiographs at the smaller scale and the similarity of recovered target components. In figure 67, the pattern of macrocracking at the back surface of the ceramic is observed by the coined pattern on the back plate of titanium alloy. This pattern is typical and is not a factor in the defeat mechanism. A strong similarity to the performance of smaller targets supports the continued use of smaller and less expensive targets to optimize designs for the defeat of long-rod threats. Moreover, the performance can be achieved in targets scaled up to defeat realistic ballistic threats.

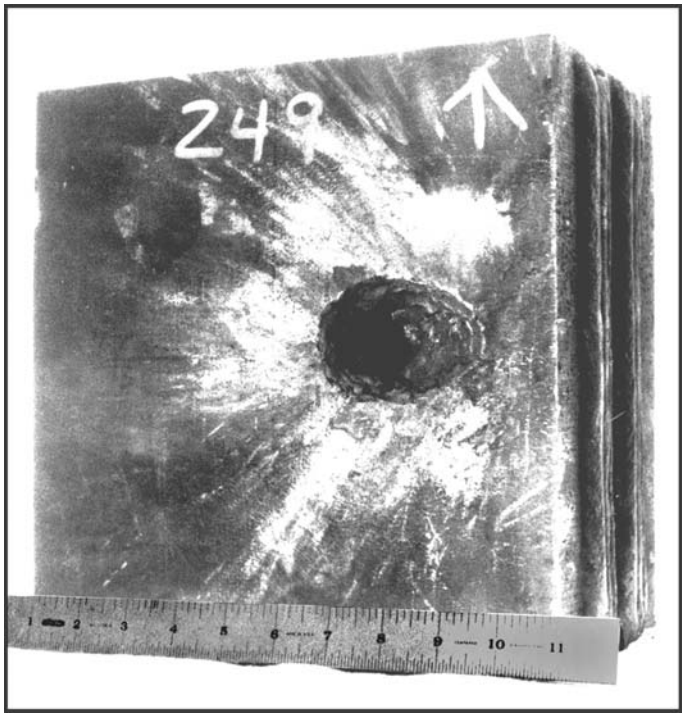

Figure 63. Recovered target from the experiment conducted with the larger scale target configuration depicted in figure 62.

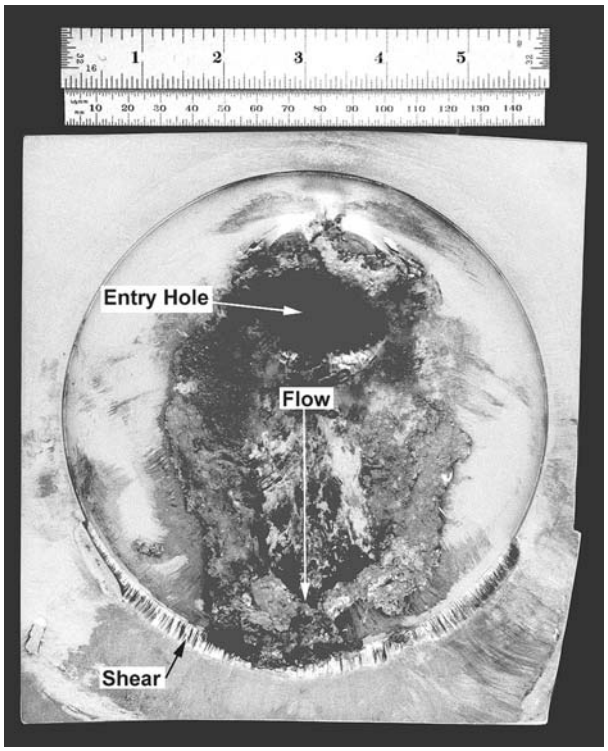

Figure 64. Graphite weak layer cavity of recovered target from the experiment conducted with the larger scale target configuration depicted in figure 62.

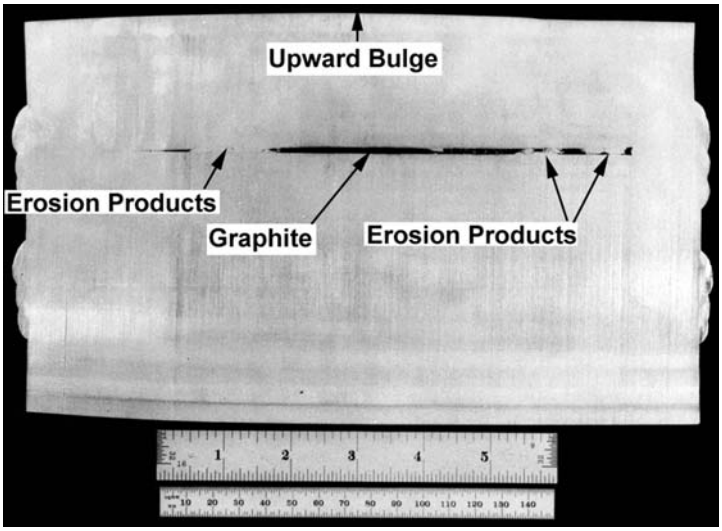

Figure 65. Cross-sectioned recovered target from the experiment conducted with the larger scale target configuration depicted in figure 62. This downstream end of the target shows how the front confinement has been forced away from the ceramic to accommodate the flow of erosion products and the graphite weak layer.

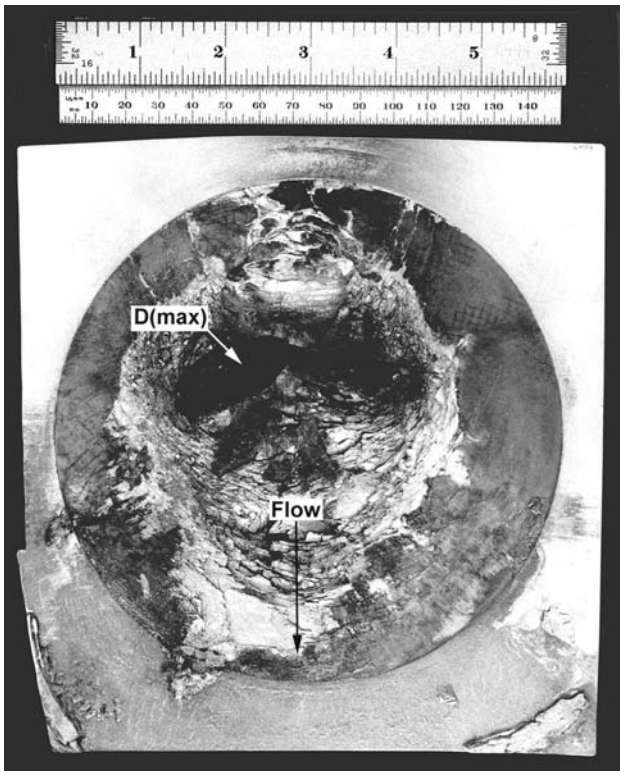

Figure 66. Ceramic layer of recovered target from the experiment conducted with the larger scale target configuration depicted in figure 62. Most of the loss of damaged ceramic occurred after the conclusion of interface defeat.

6. Preliminary Exploration to Optimize Armor Design

Weight, cost, and ease of construction are concerns in the development of practical ceramic armor. As part of the preliminary exploration into this area, substitutions and simplifications have been introduced and target layers have been minimized or eliminated to examine influences on the projectile defeat process. Some experiments have also addressed the nature of the attack. This phase of the investigation has not progressed far, but this section of the report includes the preliminary results and some brief discussion which may be of value for continuing efforts to exploit this armor phenomenon.

6.1 Influence of the Ceramic Species on Interface Defeat at Obliquity

The ceramic in nearly all experiments was hot-pressed TiB_2. This choice was based on both performance and economy. TiB_2 has had a history of high ballistic performance, beginning with the small reverse-ballistic experiments. Although this ceramic is relatively expensive, it is electrically conducting and relatively inexpensive to machine quickly and precisely using wire

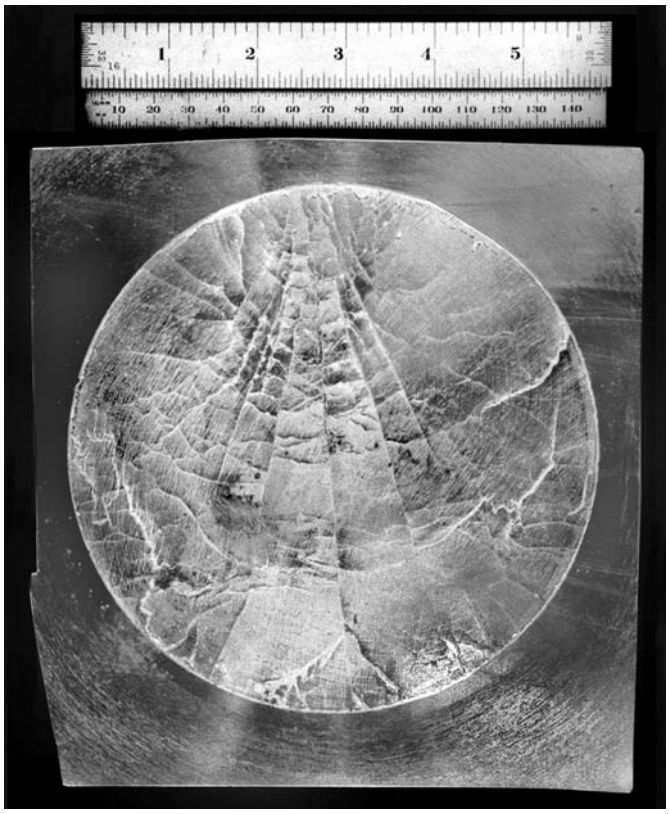

Figure 67. Pattern of macrocracking of ceramic rear surface, observed as a pattern coined into the rear Ti-6Al-4V plate recovered from the target configuration depicted in figure 62.

electric discharge machining. For these reasons, it has been the preferred ceramic for recent studies of interface defeat. Only two other ceramics have been evaluated in the target configuration of figure 45: Ebon A Al_2O_3 and B_4C. A flash radiograph of interface defeat with Ebon A is shown in figure 68. The interface flow is nearly identical to that observed with TiB_2 in figure 50, and this is consistent with the nearly identical target dimensions. Ebon A sustained greater unloading damage at the conclusion of interface defeat, but this was not unexpected since it also occurred in an earlier experiment with a heavy target, reported in section 4.4. B_4C, even at an obliquity of 45^o, was easily penetrated at the usual attack velocity of 1600 m/s. The flash radiograph from this experiment is shown in figure 69 and indicates only a brief interval of dwell. Again, this result is similar to an earlier result, reported in section 4.4, with B_4C in a heavy target attacked at normal incidence.

6.2 Value of Prestress in Interface Defeat at Obliquity

The role of prestress in interface defeat is not well understood. In the small-scale, reverse-ballistic experiments, interface defeat was always achieved without the benefits of prestress. However, impact velocities in those experiments were always below 1450 m/s. In interface-

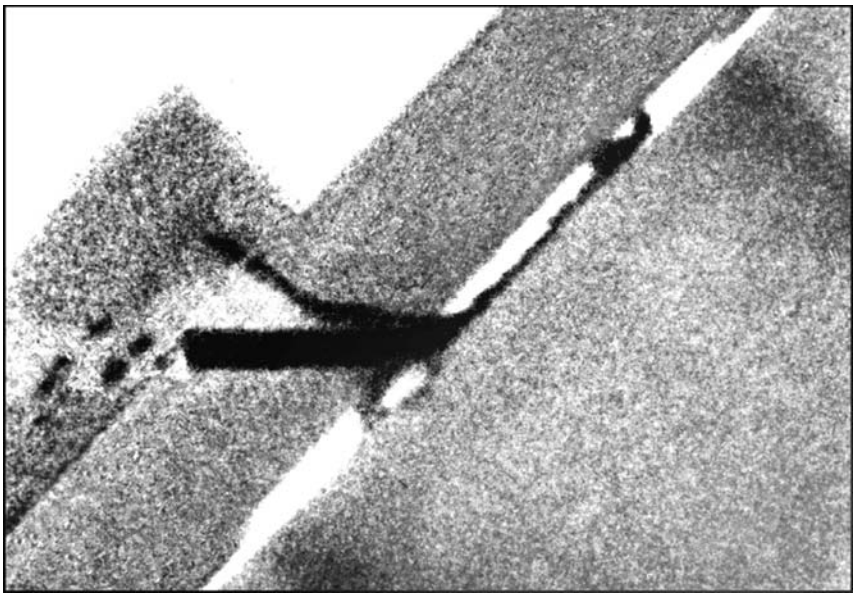

Figure 68. Flash radiograph showing interface defeat with Ebon A Al_2O_3 ceramic in the target configuration depicted in figure 45.

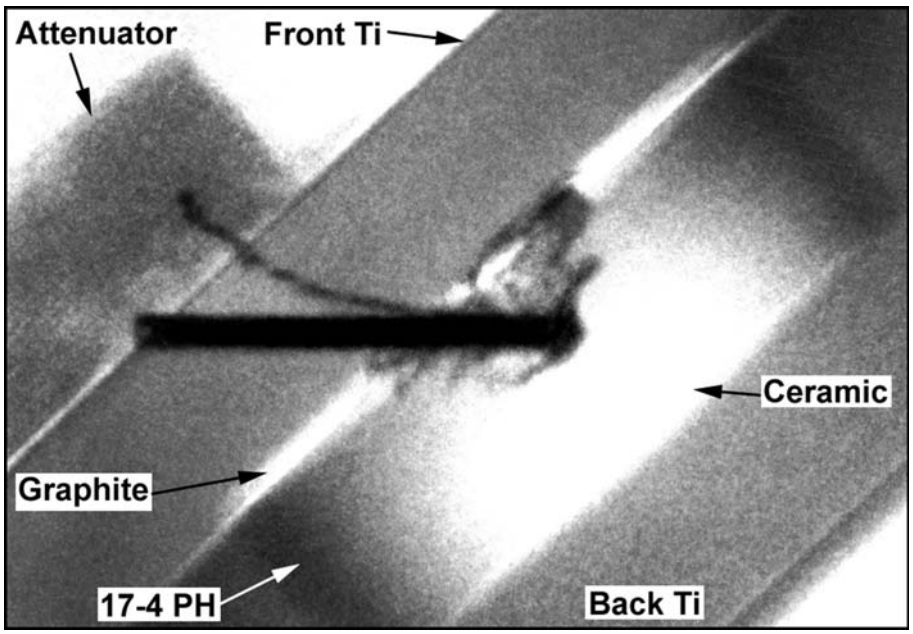

Figure 69. Flash radiograph showing penetration of B_4C ceramic with little evidence of dwell.

defeat experiments at larger scale, the necessity of prestress was strongly influenced by two experiments which may have been flawed. In one experiment, the alternative to prestress was an epoxy interface bond between the ceramic and its lateral confinement. The epoxy interface bond could have contributed to poor ballistic performance as a consequence of either wave damage (from the impedance mismatch) or weak mechanical support. In the other experiment, the weak interface layer was located, together with the ceramic, within the steel tube that prestressed the

ceramic. In that experiment, the flow of erosion products into the weak layer produced a stress which acted against the interior of the steel tube and opposed the prestress. In fact, stress produced by erosion products flowing into the weak layer could have exceeded the prestress by a significant amount, leaving the ceramic with no lateral support. Such a loss of support could explain the damage that allowed penetration.

The target shown in figure 70 was introduced for an experiment at 45° obliquity to determine if interface defeat could occur if the ceramic target had substantial lateral support, but minimal prestress, and reduced symmetry. Bars of Ti-6Al-4V were pressed against the edges of a TiB_2 tile, 76 mm × 76 mm and 25 mm thick. This layer was then sandwiched between back and front Ti-6Al-4V plates with thicknesses of 25 and 12.7 mm, respectively. The weak layer of graphite was accommodated by a 3.2-mm-deep cavity in the front plate. The three target layers were assembled by intermittent welding, with intervals for cooling. The ceramic experiences some prestress after the final cooling to room temperature, but less than produced by the usual shrink fit after preheating the confinement to 538^{o} C. In any case, the simplified construction achieved excellent interface flow, as shown by the flash radiograph in figure 71. The target was opened (albeit, with difficulty) to reveal that flow was retained within the area over the ceramic. A "chunky" type of failure occurred within the top 6 mm of the ceramic, but underlying ceramic was relatively intact. This damage could have resulted from either or both the defeat process or efforts to disassemble the target.

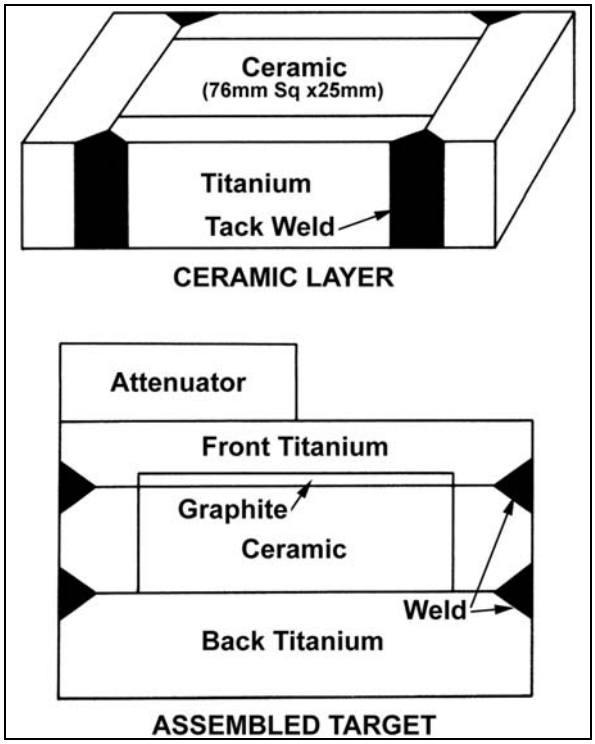

Figure 70. Target configuration used to support a square ceramic tile with minimum prestress.

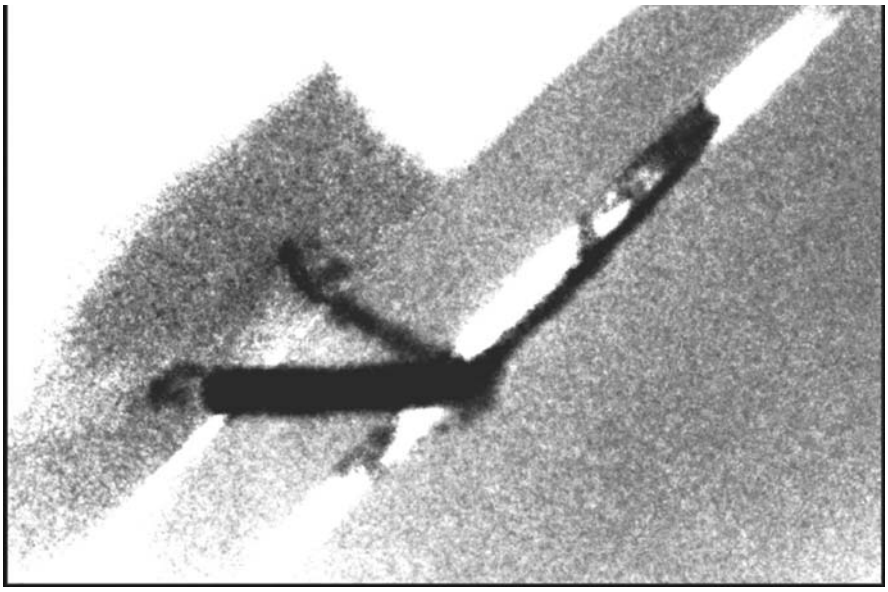

Figure 71. Flash radiograph of interface defeat at TiB_2 ceramic surface using the target configuration depicted in figure 70.

6.3 Graphoil as a Substitute for Graphite

One experiment with the target configuration of figure 45 was conducted with Graphoil (Grade GTA, Union Carbide, Cleveland, OH) as a convenient substitute for graphite. This Graphoil had a density which was only 63% of the usual graphite density of 1.67 Mg/m^3. To compensate, Graphoil sheets with a total thickness greater than the desired thickness of the weak layer were compressed into the cavity in the front Ti-6Al-4V plate. In principle, this achieved the density of the usual graphite. In reality, the Graphoil became embrittled and characteristics of the usual graphite were not duplicated. The flash radiograph from this experiment is shown in figure 72. The tip of the interface flow is more compacted than usual, suggesting more flow resistance than usual. Also, there is more extensive invasion of erosion products into the microdamaged region beneath the impingement area, suggesting higher stress in the impingement area, which is consistent with increased resistance to flow in the weak layer. Finally, the weld of the target failed catastrophically, indicating a higher interface stress than usual. Although the recovered target displayed a 5-mm-deep invasion of the microdamaged region, there was a notable absence of the extended macrocracking evident in the recovered ceramic of figure 51, for example. The experiment with Graphoil produced both promising and discouraging results that merit further consideration.

6.4 Behavior of Marginal Target Designs

After interface defeat was encountered in small-scale, reverse-ballistic experiments, sustained dwell was not observed again until TiB_2 ceramic was tested in the target configuration of figure 13. The front steel plate in that experiment was 6.35-mm-thick AISI4340 steel with a hardness of 415 BHN. This target was attacked at normal incidence by the standard X21 WHA

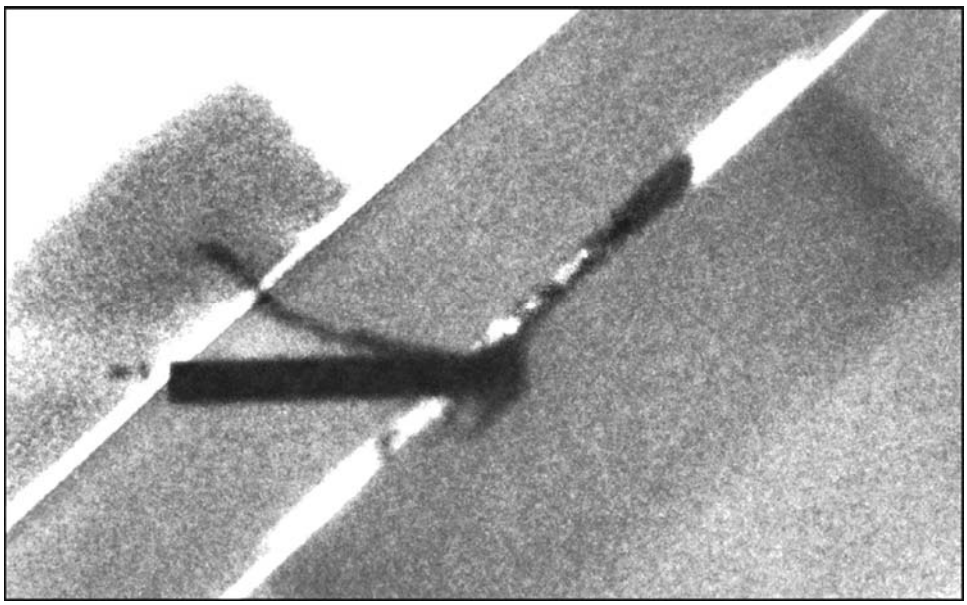

Figure 72. Flash radiograph of an experiment where the graphite weak layer was replaced by Graphoil.

long-rod projectile launched at 1590 m/s. The recovered target displayed clear evidence of sustained dwell, despite catastrophic failure of the thin front confinement. It was assumed that rapid bulging of the front plate accommodated the lateral flow of erosion products at the ceramic. This behavior was not investigated further at that time because a weak target layer was soon introduced. The weak layer prevented shear-blockage of lateral flow under thicker front confinement which did not fail catastrophically. Later, after the introduction of titanium confinement permitted flash-radiographic observations in the larger targets, experiments were again conducted to examine behavior of ceramic targets with thin front confinement. However, targets in the later experiments were attacked at an obliquity of 45° rather than at the special case, most severe condition of normal incidence.

Figure 73 is a flash radiograph which shows the flow of erosion products at a TiB_2 surface covered by a 6.35-mm-thick front plate of Ti-6Al-4V. The ceramic was shrink fitted into a tube of 17-4 PH steel, which was subsequently shrink fitted into a cavity machined in the back plate of Ti-6Al-4V, which then provided back support with a thickness of 19 mm of the Ti-alloy. The radiograph clearly shows a small displacement of damaged ceramic and flow which returns to the interface. This observation is consistent with the behavior inferred from the earlier target with steel confinement. It is assumed that this behavior by TiB_2 results from its increasing shear strength with increasing compressive stress (Dandekar and Benfanti, 1993).

Figure 74 is the flash radiograph from another experiment in which the front confinement of TiB_2 was a 6.35-mm-thick plate of Ti-6Al-4V. The method of construction was unchanged, but the ceramic thickness was reduced to 12.7 mm and the Ti-6Al-4V back support was increased to

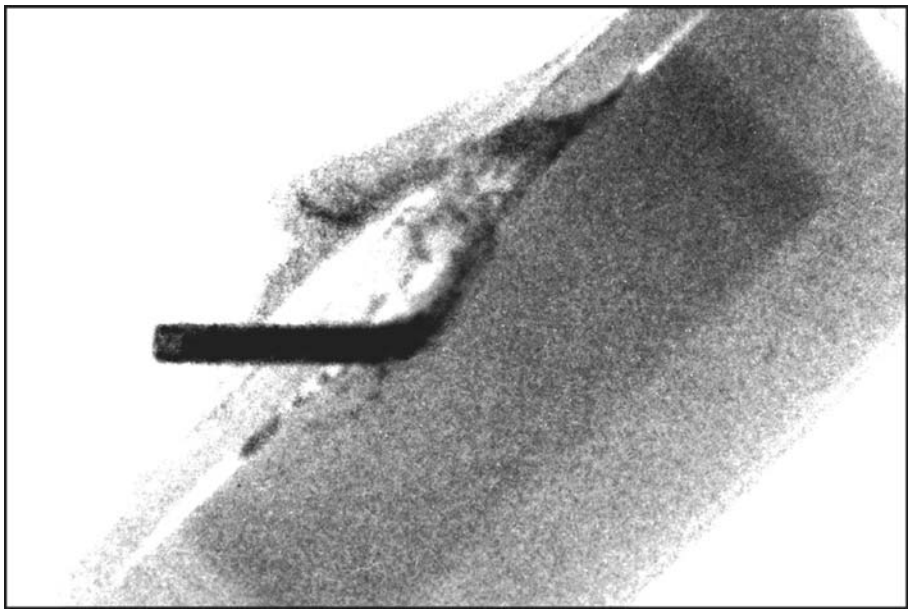

Figure 73. Flash radiograph that shows interface defeat of WHA rod projectile obliquely attacking TiB_2 ceramic confined by Ti-6Al-4V, but without a shock attenuator or weak accommodating layer.

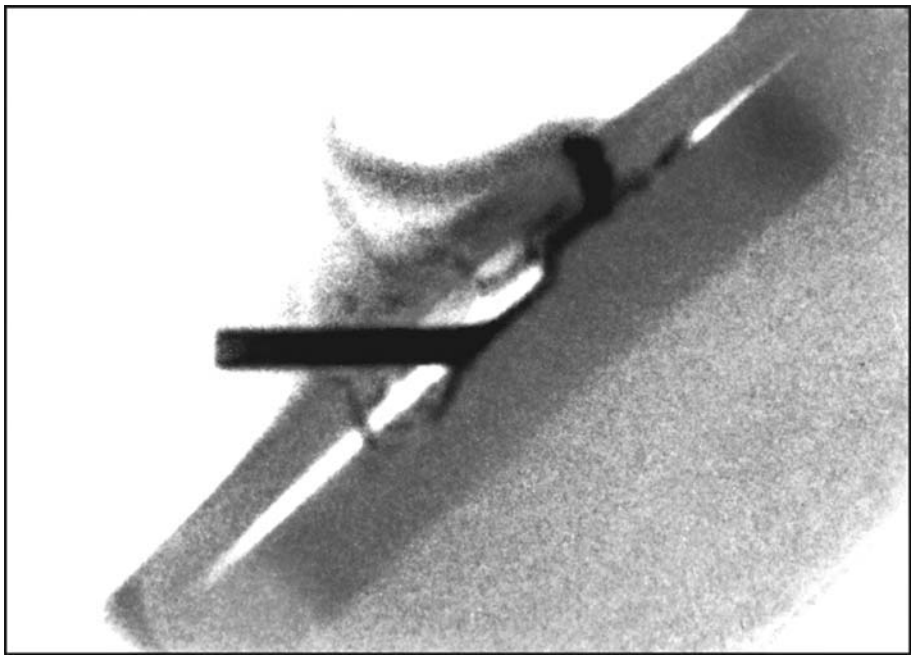

Figure 74. Flash radiograph of revised target configuration that shows interface defeat of WHA rod projectile obliquely attacking TiB_2 ceramic confined by Ti-6Al-4V, but without a shock attenuator or weak accommodating layer.

a thickness of 38 mm. The radiograph suggests less displacement of damaged ceramic and a slight improvement in flow behavior, which probably is a consequence of increased support at the back of the ceramic. Figures 73 and 74 both show catastrophic failure of the thin front plate.

Catastrophic failure of the thin front plate is not observed in the radiograph of figure 75 because that target contained a weak layer of graphite. The weak layer delays catastrophic failure of the thin front plate until later when stress increases in the downstream portion of the compressed graphite, well-separated from the entry hole through the front plate. The addition of graphite clearly modifies the internal stress and the flow of erosion products. This may mean that the thickness of back support can be reduced when a weak layer is present. The optimization of modules containing TiB_2 is an area that requires further investigation.

Marginal target configurations containing SiC were also examined by a brief series of experiments. Figure 76 shows the flash radiograph from the initial experiment in which a 25.4 mm-thick tile of SiC-N was laterally supported by a shrink fit; front and back plates of Ti-6Al-4V had thicknesses of 6.35 and 19 mm, respectively. Figure 76 shows catastrophic failure of the thin front plate in the vicinity of the entrance hole. There is evidence of brief dwell, followed by penetration into the ceramic. The radiograph and the recovered target provided data that permitted an analysis based on the Tate Model of long-rod penetration. The radiograph established DOP at a known time, and the recovered target established that penetration ended almost precisely at the back interface of the ceramic. Data by Anderson et al. (1992) provided a penetration resistance for the front Ti-6Al-4V. With the assumption of a constant penetration resistance for the SiC-N ceramic, the analysis established a dwell-duration of 7 μs and a penetration resistance of 11.3 GPa after dwell. This penetration resistance of the ceramic is nearly twice the penetration resistance of titanium during deep penetration. In optimizing an armor module of SiC-N and Ti-6Al-4V, it should be beneficial to minimize the metallic component which has the higher density and the lower penetration resistance. This conclusion tends to be supported by the flash-radiographic observations in figures 77 and 78, but it should be noted that those experiments used SiC-B rather than SiC-N, and it is presently inconclusive which SiC variant is best suited for interface defeat applications. In the experiment of figure 77, the ceramic thickness was reduced to 12.7 mm and the back Ti-6Al-4V thickness was increased to 38 mm. In the experiment of figure 78, a weak layer of graphite was added between the 6.35-mm-thick titanium and the ceramic. The weak layer prevented catastrophic failure of the front plate, but had no detectable influence on performance. Both targets were perforated, which precluded a meaningful analysis. However, it should be noted that a line-of-sight areal density of 27.0 g/cm^2 defeated the rod in figure 76, while line-of-sight areal densities near 34 g/cm^2 were perforated in the experiments of figures 77 and 78.

Results with SiC should be considered preliminary and subjects for additional study and evaluation. For example, the ballistic performance of SiC has seemed somewhat erratic, and the reason is unknown. There is some suspicion that the erratic electrical conductance of SiC might be associated with erratic ballistic performance. It can vary from tile to tile, and within a tile. In some early experiments with successful interface defeat, electrical conductance was essentially absent at the impacted surface. The source of variable electrical conductance is not established,

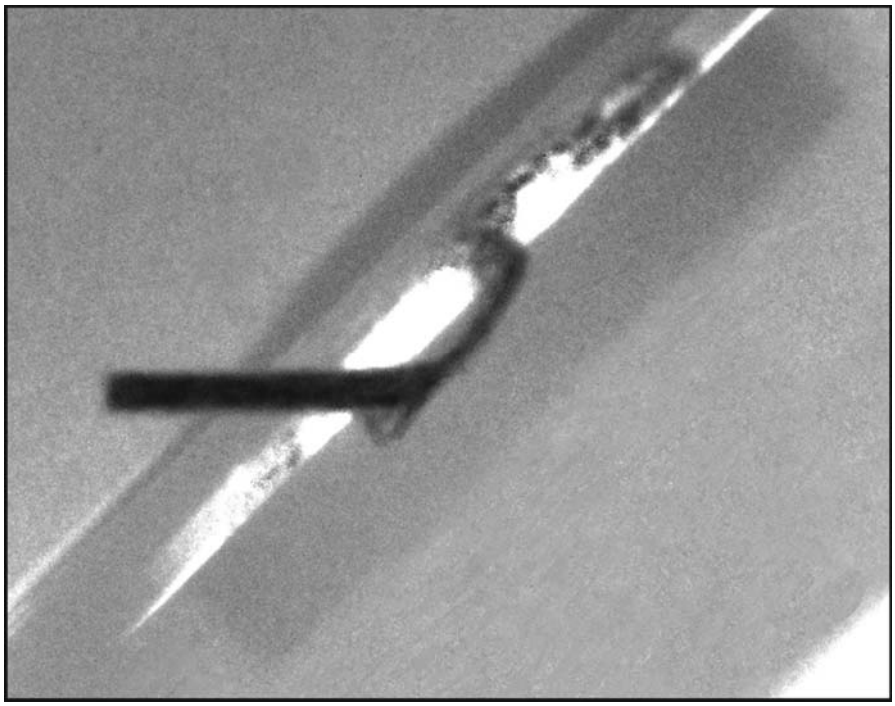

Figure 75. Flash radiograph that shows interface defeat of WHA rod projectile obliquely attacking TiB_2 ceramic confined by Ti-6Al-4V, but front confinement is thin, and without a shock attenuator.

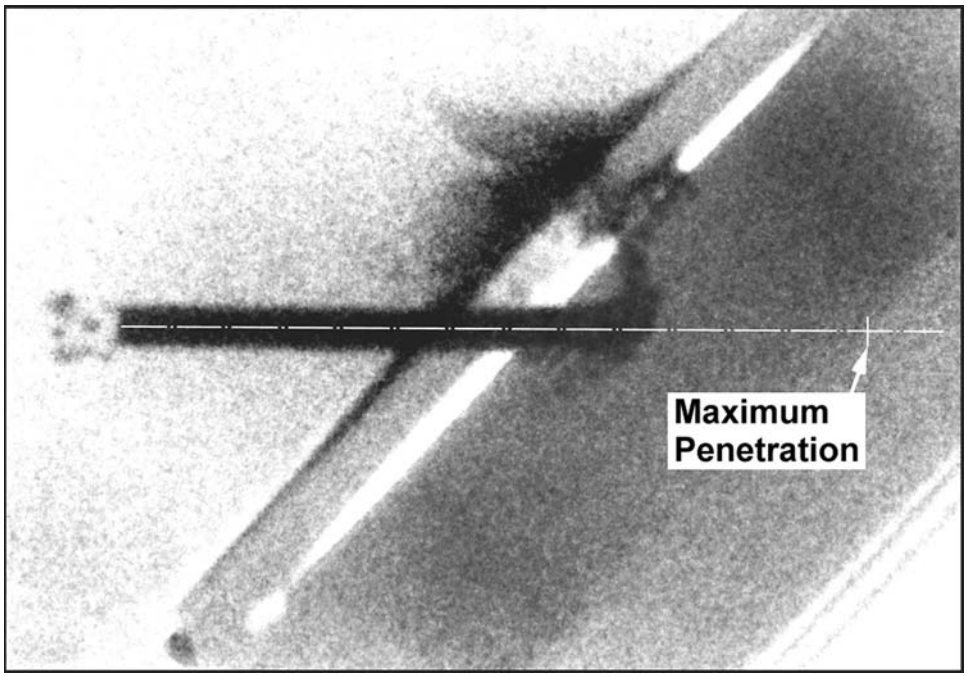

Figure 76. Flash radiograph that shows brief period of dwell followed by penetration into the SiC-N ceramic in a target configuration with thin Ti-6Al-4V front confinement, but without a shock attenuator or weak accommodating layer.

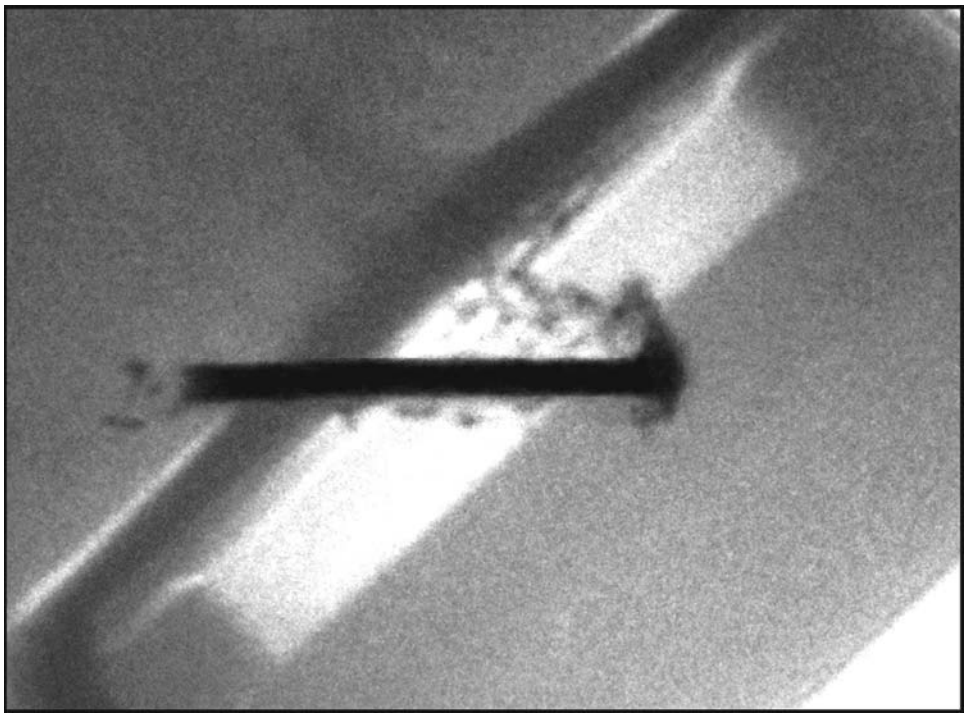

Figure 77. Flash radiograph of revised target configuration (thin Ti-6Al-4V front confinement) that shows brief dwell followed by penetration of WHA rod projectile obliquely attacking SiC-B ceramic confined by Ti-6Al-4V, but without a shock attenuator or weak accommodating layer.

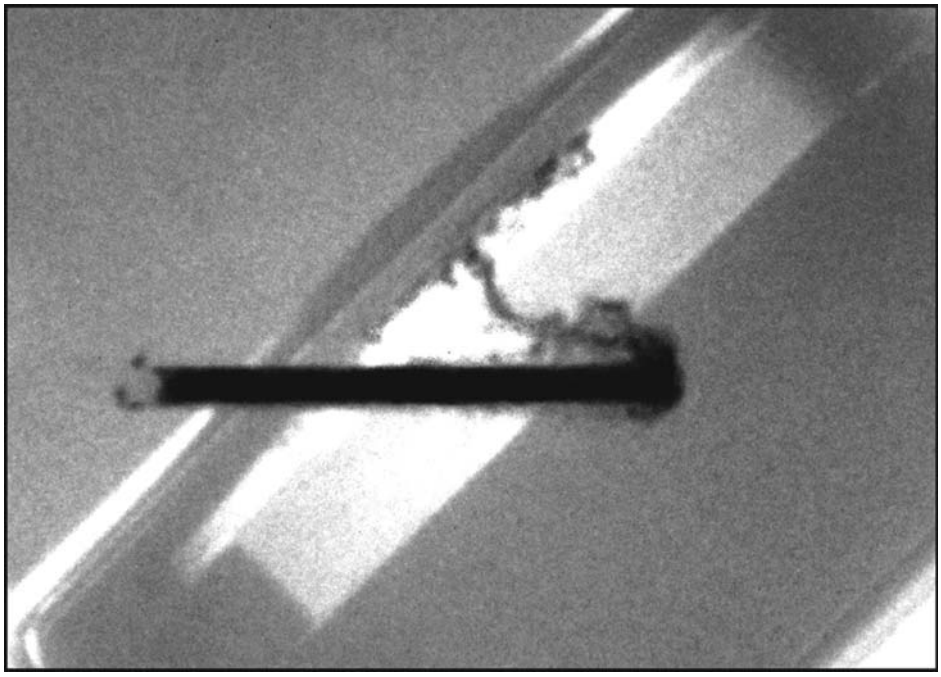

Figure 78. Flash radiograph of revised target configuration (thin Ti-6Al-4V front confinement) that shows brief dwell followed by penetration of WHA rod projectile obliquely attacking SiC-B ceramic confined by Ti-6Al-4V, without a shock attenuator, but with a weak accommodating layer.

but it may result from contamination by graphite tooling used to process tiles of SiC. It is conceivable that the presence of graphite contamination might reduce the ability of microdamaged ceramic to "lock-up" the resultant grains under the compressive load of an attacking long-rod projectile. Since SiC is a potential candidate for armor applications, it may be appropriate to investigate interface defeat with SiC tiles carefully selected on the basis of electrical conductance.

6.5 Normal Impact as an Extreme Condition

Ceramic targets with Ti-6Al-4V confinement have usually been tested at obliquity. Although it is easier for lighter-weight target configurations to achieve interface defeat at obliquity, they can also achieve interface defeat at normal incidence. However, a module intended for protection against attack at normal incidence would require thicker rear support for the ceramic. Figures 79 and 80 show a target recovered after interface defeat at normal incidence. In this experiment, a 25-mm-thick tile of TiB_2 (72 mm diameter) was supported at the front and back by Ti-6Al-4V plates with thicknesses of 19.5 and 52 mm, respectively. The ceramic defeated a standard WHA long-rod projectile, launched at a velocity 1600 m/s. Figure 79 shows the final state of flow into the graphite layer, with some of the graphite still present. Figure 80 shows the surface of the

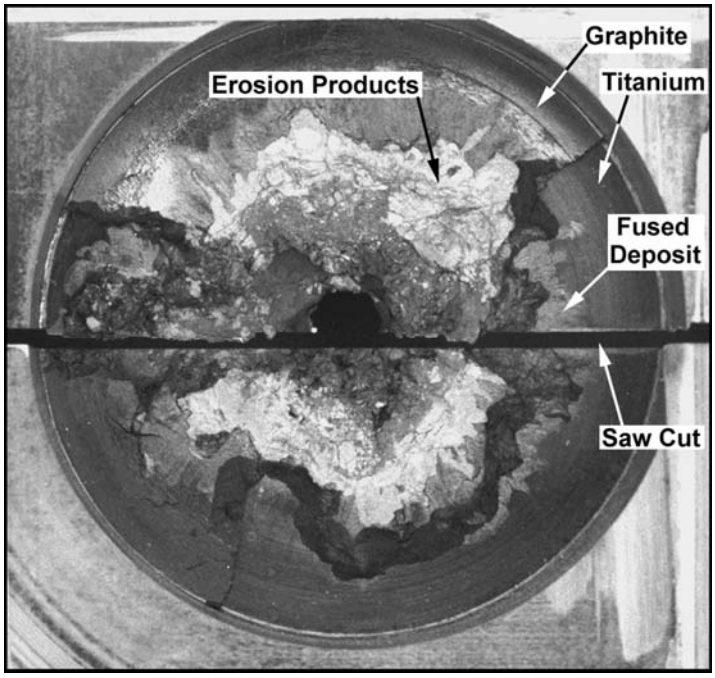

Figure 79. Graphite weak layer cavity of the target configuration depicted in figure 42. The interface accumulation of erosion products from the defeat of a WHA rod projectile attacking at normal incidence is illustrated.

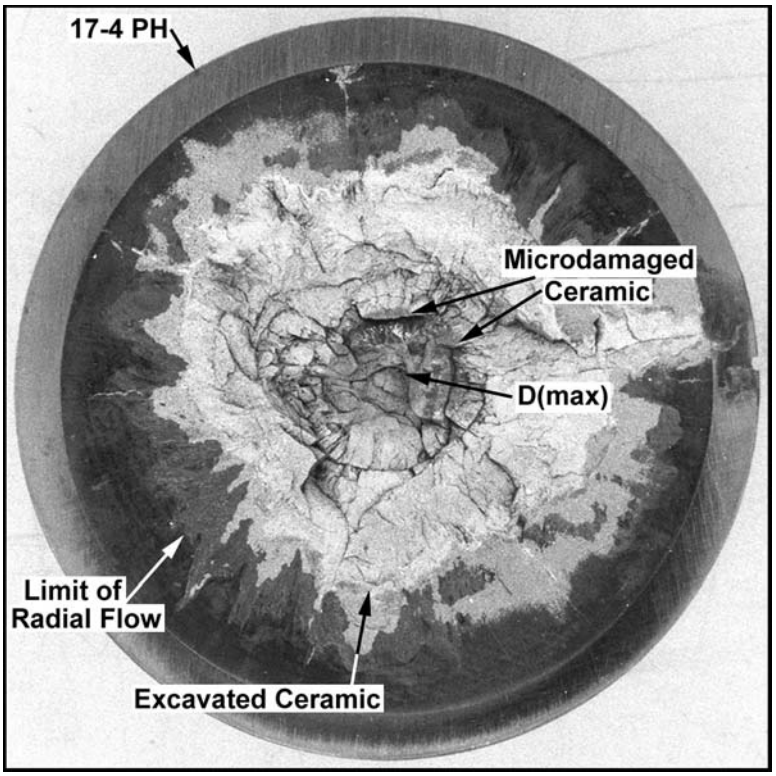

Figure 80. Recovered TiB_2 ceramic tile that was in contact with the graphite layer depicted in figure 79.

ceramic which was invaded by erosion products to a maximum depth of nearly 5 mm. This invasion into the microdamaged ceramic occurred early in the attack and did not increase at later times. For comparison, the recovered ceramic in figure 51, with only a 32-mm thickness of Ti-6Al-4V back support, experienced no invasion into the microdamage ceramic during an attack at 45° obliquity. This further illustrates the benefit of mounting ceramic armor modules to favor an oblique impact encounter.

6.6 Comparison of Titanium Alloy and Steel Confinement

The cost of fabricating light titanium alloy targets makes it tempting to substitute steel for the Ti-alloy in optimization experiments that can be evaluated by an examination of recovered targets. However, a preliminary comparison of RHA and Ti-6Al-4V confinements in attacks at 45° obliquity indicated a reduced interface flow and an increased tendency to displace ceramic when the confinement was RHA steel. It is suspected that shear failure at the back of the Ti-6Al-4V front plate may facilitate the flow of erosion products into the weak layer of graphite and minimize stress in the impingement area. In contrast, ductile bulging at the back of an RHA front plate may tend to inhibit the transition to interface flow, which slightly elevates the stress in the impingement area, while slightly depressing the supporting stress downstream of the impingement area. The interpretation of this behavior is tentative; further study is required for confirmation.

6.7 Nose Shape of the Attacking Rod

The influence of projectile nose shape was identified soon after the influence of a support gap was identified (section 6.6). It was noted that a support gap might be minimized or eliminated by introducing a long-rod projectile with an ogival nose which was capable of penetrating in rigid-body mode. The first experiment demonstrated that the eroding-rod mode of penetration is necessary to initiate interface defeat. Consequently, it was necessary to add a front target layer that was capable of degrading the ogival nose during the initial impact phase of the ballistic encounter. A degraded ogival nose penetrated in the eroding mode and was defeated at the ceramic.

7. Conclusions

The interaction of a long-rod projectile with a ceramic target involves behavior that is only partially understood. Experimental studies and limited modeling have provided some insight, but characteristics of the projectile, the ceramic, and the system that supports the ceramic introduce complex problems that must be resolved to approach the goal of practical ceramic armor designs which take advantage of the strength and density of structural ceramics.

The role of the projectile is to damage the ceramic so it can be displaced and perforated. Without a supporting system, a ceramic tile is damaged and can be defeated easily by a high-velocity rod. The shock wave from impact propagates to the near surface at the rear of the tile where it may produce tensile damage. At lateral boundaries, unloading waves can return and interact to produce tensile damage in the central region of the tile. Cone cracks propagate from around the impingement area and separate a reduced volume of ceramic that can be driven forward by the projectile. Microdamage can result from shear stress beneath the impingement area, and particles of ceramic can be displaced from the microdamaged volume to allow penetration. As the tip of the projectile penetrates into the ceramic, the flow of eroded projectile material changes direction, which increases stress in the contact area and further promotes damage and penetration. As the tip of the projectile invades the ceramic, force is transmitted more effectively in the lateral direction, promoting the propagation of radial cracks. Arrival of radial cracks at the lateral boundaries subdivides the ceramic into independent wedge-shaped blocks that are displaced laterally, contributing further to easy perforation of the ceramic.

The role of the ceramic, with help from its supporting system, is either to stop or to divert the projectile. From energy considerations, it is easier to divert the projectile. The supporting system for the ceramic involves complex considerations. It must counter behavior that degrades a bare ceramic tile, but it must not add excessive parasitic weight to preclude application as practical armor. In other words, support must be carefully optimized and compromises will certainly be necessary. An illustration is the heavy laboratory target initially introduced to study

interface defeat. This target could defeat a long-rod projectile, but it placed a priority on recovery of the ceramic with minimum damage. This made the target too heavy for practical armor applications. The primary function of practical armor is defeat of the projectile with minimum target weight. With only the requirement for defeat, weight can be significantly reduced. Minimum weight can be achieved by careful selection of materials and designs, and correct identification of critical dynamic behavior. Time resolved observations were found to provide more reliable guidance to dynamic behavior than post-test examinations of recovered target components.

Design of the supporting system for a ceramic tile was guided by considerations of wave damage, microdamage, macrodamage, static support, dynamic support, and stress. A structure was introduced to attenuate the shock wave produced at impact, and front confinement was selected to provide optimum support (including a minimized support gap) around the microdamaged region. Lateral prestress was introduced for its possible contribution to the control of microdamage and macrodamage. However, a few experiments have raised doubt about its contribution to interface defeat and further study is needed. The requirement for static rear support was relaxed, resulting in reduced weight, but increased macrodamage of the ceramic. However, with confirmed interface flow into a weak accommodating layer of graphite, interface stress contributed dynamic front support for the ceramic and the reduced rear support could be tolerated. The weak layer, which promotes interface flow and helps to control the level of support at the front of the ceramic, also assures minimum stress in the impingement area and minimum microdamage. Optimizing all of these design features should minimize the weight. However, as noted earlier, the response can be complex. In the case of TiB_2, the response is different from that of the few other ceramics that have currently been evaluated. This ceramic is able to produce a version of interface defeat without the benefit of an attenuator or a weak interface layer. In comparison, SiC is more conventional, defeating a long-rod projectile by brief dwell followed by eroding-rod penetration. The alternative system components that produce interface defeat with TiB_2 must each be optimized to determine which can defeat an attacking long-rod projectile with the lower weight of ceramic and supporting structure.

A number of areas must be considered in future studies. Ceramic properties are clearly a major influence on the defeat process. TiB_2 offers excellent ballistic performance, but other, lower density ceramics should be evaluated, with attention to the reasons for good or poor performance. Obliquity is another area that needs expanded study. Obliquity minimizes impingement stress and microdamage, so is an important consideration in practical applications. In principle, increased obliquity should also compensate for increased threat velocity, and this is an area for future study. The influence of impact location and how to optimize area coverage is a very important area which presently has received little consideration. Finally, conventional long-rod projectiles of WHA, DU, and steel do not seem to offer an unusual challenge. However,

unconventional projectiles such as rods with a noncircular cross section, segmented rods, and rods with a hard core or ogival tip could present a difficult challenge and should be included for future study and evaluation.

8. References

Anderson, C. E.; Walker, J. D.; Hauver, G. E. Target Resistance for Long-Rod Penetration into Semi-Infinite Targets. *Nuclear Engineering and Design* **1992**, *138*, 93−104.

Bless, S. J.; Benyami, M.; Apgar, L. S.; Eylon D. Impenetrable Ceramic Targets Struck by High Velocity Tungsten Long Rods. *Proceedings of the Second International Conference on Structures Under Shock and Impact*, Portsmouth, UK, 16−18 June 1992.

Dandekar, D. P.; Bartkowski, P. Strength of AD-995 Alumina under Impact Loading. *Proceedings of the 19th Army Science Conference*, Orlando, FL, 20−23 June 1994.

Dandekar, D. P.; Benfanti, D. C. Strength of Titanium Diboride under Shock Wave Loading. *Journal of Applied Physics* **1993**, *73* (2), 673−679.

Dehn, J. Modeling Armor that Uses Interface Defeat. *Proceedings of the 6th Annual TARDEC Combat Vehicle Survivability Symposium*, Monterey, CA, March 28–30 (1995a); Vol. 1, pp 443−448.

Dehn, J. U.S. Army Research Laboratory, Aberdeen Proving Ground, MD. Private communication, 1995b.

Fischer-Cripps, A. C.; Lawn, B. R. Stress Analysis of Contact Deformation in Quasi-Plastic Ceramics. *Journal of the American Ceramic Society* **1996**, *79*, (10), 2609−2618.

Franz, R. E.; Leighton, K. T. *Investigation of Stress Waves and Failure Phenomenology in Aluminum Metal Matrix Composite and Titanium Diboride Laminated Armor*; SBIR Phase I Final Report − DARPA Topic 91−150, Lanxide Armor Products: Newark, DE, 1992.

Hauver, G. E.; Melani, A. Behavior During Penetration by Long Rods (U). *Proceedings of the Second BRL Topical Symposium: Experimental Research and Modeling Support*, U.S. Army Ballistic Research Laboratory, Aberdeen Proving Ground, MD, 24 May 1988; pp 149−160.

Hauver, G. E.; Netherwood, P. H.; Benck, R. F.; Gooch, W. A.; Perciballi, W. J.; Burkins; M. S. Variation of Target Resistance During Long-Rod Penetration into Ceramics. *Proceedings of the 13th International Symposium on Ballistics*, National Defence Establishment, S−172 90, Sundyberg, Sweden, 1992; Vol. 3, pp 257−264.

Hauver, G. E.; Netherwood, P. H.; Benck, R. F.; Kecskes, L. J. Ballistic Performance of Ceramic Targets. *Proceedings of the 13th Army Symposium on Solid Mechanics*, Plymouth, MA, 17–19 August 1993; pp 23−34.

Hauver, G. E.; Netherwood, P. H.; Benck, R. F.; Kecskes, L. J. Enhanced Ballistic Performance of Ceramics. *Proceedings of the 19th Army Science Conference*, Orlando, FL, 20−24 June 1994.

Kolsky, H. *Stress Waves in Solids*; Dover: New York, 1963.

Lawn, B. R.; Padture, N. P.; Cai, H.; Guiberteau, F. Making Ceramics Ductile. *Science* **1994,** *263*, 1114−1116.

Netherwood, P. H. *Nucleation and Growth of Fractures in Plexiglas*; BRL−IMR−57; U.S. Army Ballistic Research Laboratory: Aberdeen Proving Ground, MD, August 1972.

Shockey, D. A.; Marchand, A. H.; Skaggs, S. R.; Cort, G. E.; Burkett, M. W.; Parker, R. Failure Phenomenology of Confined Ceramic Targets and Impacting Rods. *International Journal of Impact Engineering* **1990**, *9*, (3), 263−275.

Silsby, G. F. Penetration of Semi-Infinite Steel Targets by Tungsten Long Rods at 1.3 to 4.5 km/s. *Proceedings of the Eighth International Symposium on Ballistics*, Orlando, FL, 1984.

Tate, A. A Theory for the Deceleration of Long Rods After Impact. *Journal of the Mechanics and Physics of Solids* **1967**, *15*, 387−399.

Tate, A. Further Results in the Theory of Long Rod Penetration. *Journal of the Mechanics and Physics of Solids* **1969**, *17*, 141−150.

Woolsey, P.; Mariano, S.; Kokidko, D. Alternative Test Methodology for Ballistic Performance Ranking of Ceramics. *Proceedings of the 5th Annual TACOM Armor Coordinating Conference*, Monterey, CA, 1989.

NO. OF
COPIES ORGANIZATION

1 (PDF ONLY) DEFENSE TECHNICAL INFORMATION CTR
DTIC OCA
8725 JOHN J KINGMAN RD
STE 0944
FORT BELVOIR VA 22060-6218

1 US ARMY RSRCH DEV & ENGRG CMD
SYSTEMS OF SYSTEMS INTEGRATION
AMSRD SS T
6000 6TH ST STE 100
FORT BELVOIR VA 22060-5608

1 INST FOR ADVNCD TCHNLGY
THE UNIV OF TEXAS
AT AUSTIN
3925 W BRAKER LN STE 400
AUSTIN TX 78759-5316

1 DIRECTOR
US ARMY RESEARCH LAB
IMNE ALC IMS
2800 POWDER MILL RD
ADELPHI MD 20783-1197

3 DIRECTOR
US ARMY RESEARCH LAB
AMSRD ARL CI OK TL
2800 POWDER MILL RD
ADELPHI MD 20783-1197

3 DIRECTOR
US ARMY RESEARCH LAB
AMSRD ARL CS IS T
2800 POWDER MILL RD
ADELPHI MD 20783-1197

ABERDEEN PROVING GROUND

1 DIR USARL
AMSRD ARL CI OK TP (BLDG 4600)

NO. OF
COPIES ORGANIZATION

3 DIRECTOR
USARL
AMSRD ARL RO EM
D MANN
J PRATER
D STEPP
PO BOX 12211
RSCH TRIANGLE PARK
NC 27709

3 DIRECTOR
USARL
AMSRD ARL RO EN
T DOLIGALSKI
B LAMATTINA
A RAJENDRAN
PO BOX 12211
RSCH TRIANGLE PARK
NC 27709

17 SANDIA NATL LABS
MAIL SERVICES MS-0100
P YARRINGTON MS0316
D FREW MS0325
M E KIPP MS0370 9232
S A SILLING MS0376 9232
M FORRESTAL MS0482
823/LIBRARY MS0731 6850
MS0751
A F FOSSUM 6117
D R BRONOWSK 6117
M Y LEE 6117
R M BRANNON 6117
MS0836
E S HERTEL 9116
J V COX MS0893 9123
TECHNICAL LIBRARY MS0899 9616
V LUK MS1160
MS1181
L C CHHABILDAS 1647
T J VOGLER 1647
W D REINHART 1647
PO BOX 5800
ALBUQUERQUE NM 87185-0100

1 APPLIED RSCH ASSOC INC
D E GRADY
4300 SAN MATEO BLVD NE
SUITE A-220
ALBUQUERQUE NM 87110

NO. OF
COPIES ORGANIZATION

2 BROWN UNIV
DIV OF ENGR
R CLIFTON
L B FREUND
PROVIDENCE RI 02912

4 CALIFORNIA INST OF TECH
GRADUATE AERONAUTICAL LABS
J E SHEPHERD
G RAVICHANDRAN
N LAPUSTO
A ROSAKIS
MS 105-50
PASADENA CA 91125

1 CALIFORNIA INST OF TECH
SEISMOLOGICAL LAB 252-21
T J AHRENS
PASADENA CA 91125

3 CERCOM INC
R PALICKA
G NELSON
B CHEN
1960 WATSON WAY
PO BOX 70
VISTA CA 92083

1 DOMINCA
N WINFREE
1211 RANCHITOS RD NE
ALBUQUERQUE NM 87122

3 GEORGIA INST TECH
SCHOOL OF MTRLS SCI & ENGR
K V LOGAN
N THADHANI
M ZHOU
ATLANTA GA 30332-0245

1 INTERNATIONAL RSCH ASSOC
D ORPHAL
4450 BLACK AVE
SUITE E
PLEASANTON CA 94566

1 KERLEY TECHNICAL SVCS
G KERLEY
PO BOX 709
APPOMATTOX VA 24522-0709

NO. OF
COPIES ORGANIZATION

2 NETWORK COMPUTING SVC INC
AHPCRC
T HOLMQUIST
G R JOHNSON
1200 WASHINGTON AVE S
MINNEAPOLIS MN 55415

4 THE JOHNS HOPKINS UNIV
G W C WHITING SCHOOL
OF ENGR CTR FOR ADVANCED
METALLIC AND CERAMIC SYS
LATROBE HALL
K HEMKER
T HUFNAGEL
J F MOLINARI
K T RAMESH
3400 N CHARLES ST
BALTIMORE MD 21218

1 PM COMBAT SYSTEMS
SFAE GCS CS
J ROWE
6501 EAST ELEVEN MILE RD
WARREN MI 48397-5000

1 S SKAGGS
ROUTE 11 BOX 81E
SANTA FE NM 87501

4 SOUTHWEST RSCH INST
C E ANDERSON
J LANKFORD
S MULLIN
J WALKER
PO DRAWER 28510
SAN ANTONIO TX 78228-0510

3 US ARMY TARDEC
AMSRD TAR R MS 263
D P TEMPLETON
L P FRANKS
K D BISHNOI
6501 E 11 MILE RD
WARREN MI 48397-5000

4 UNIV OF CALIF AT SAN DIEGO
DEPT OF MECH & AEROSPACE ENGR
J ISAACS
M MEYER
S NEMAT-NASSER
V NESTERENKO
LA JOLLA CA 92093-0416

NO. OF
COPIES ORGANIZATION

4 THE UNIV OF TEXAS AT AUSTIN
INST FOR ADVANCED TECHNOLOGY
S J BLESS
H FAIR
D LITTLEFIELD
B PEDERSEN
3925 W BRAKER LN SUITE 400
AUSTIN TX 78759-5316

1 OAK RIDGE NATIONAL LAB
METALS AND CERAMICS DIVISION
CERAMICS SCI AND TECH GROUP
A WERESZCZAK
PO BOX 2008
OAK RIDGE TN 37831-6068

2 WASHINGTON STATE UNIV
INST FOR SHOCK PHYSICS
Y M GUPTA
J R ASAY
BOX 642816
PULLMAN WA 99164-2816

1 SAIC
CW KITCHENS
CV-55 RM 15A14
7990 SCIENCE APPLICATIONS CT
VIENNA VA 22182

1 JET PROPULSION LAB
M ADAMS
4800 OAK GROVE DR
BLDG 122-B3
PASADENA CA 91109

2 THE UNIV OF ARIZONA
W CHEN
B SONG
TUCSON AZ 85721-0119

1 NORTHWESTERN UNIV
MCCORMICK SCH OF ENGR &
APPLIED SCIENCES DEPT OF
MECH ENGR
H ESPINOSA
2145 SHERIDAN RD
EVANSTON IL 60208-3111

NO. OF
COPIES ORGANIZATION

4 SRI INTL POULTER LAB
D SHOCKEY
A MARCHAND
R KLOPP
L SEAMAN
333 RAVENSWOOD AVE
MENLO PARK CA 94025

2 RUTGERS ST UNIV OF NJ
MALCOLM G MCLAREN CTR
FOR CERAMIC RSCH
D NIESZ
V GREENHUT
607 TAYLOR RD
PISCATAWAY NJ 08854

4 US ARMY SBCCOM
NATICK SOLDIER CTR
P CUNNIFF
M MAFEO
M SENNETT
J WARD
KANSAS ST
NATICK MA 01760-5012

2 UNIV OF HAWAII AT
MANOA MINERALS PHYSICS
GROUP HAWAII INST OF
GEOPHYSICS & PLANETOLOGY
M MANGHNANI
G AMULELE
1680 EAST-WEST RD
HONOLULU HI 96822

4 LOS ALAMOS NATL LAB
DX-2 MATERIALS DYNAMICS
MS P952
D DATTELBAUM
D MANDELL
D ROBBINS
S SHEFFIELD
PO BOX 1663
LOS ALAMOS NM 87545

2 UNIV OF DAYTON RSCH INST
N BRAR
A PIEKUTOWSKI
300 COLLEGE PARK
DAYTON OH 45469-0182

1 R J EICHELBERGER
409 W CATHERINE ST
BEL AIR MD 21014-3613

NO. OF
COPIES ORGANIZATION

1 K FRANK
1312 MONTREAL DR
ABERDEEN MD 21001

3 G E HAUVER
303 BALD EAGLE WAY
BELCAMP MD 21017

3 P H NETHERWOOD
1502 SINGER RD
JOPPA MD 21085

4 GENERAL DYNAMICS LAND SYS
W BURKE (MZ436 21 24)
D DEBUSSCHER (MZ436 20 29)
J ERIDON (MZ436 21 24)
W HERMANN (MZ435 01 24)
38500 MOUND RD
STERLING HEIGHTS MI 48310-3200

1 ZERNOW TECHNICAL SVCS INC
L ZERNOW
425 W BONITA AVE SUITE 208
SAN DIMAS CA 91773

1 UNIV OF NEBRASKA LINCOLN
DEPT OF ENGR MECH
R FENG
LINCOLN NE 68588-0526

3 BAE SYSTEMS
M LAM
M MIDDIONE
R MUSANTE
1205 COLEMAN AVE
SANTA CLARA CA 95050

2 NSWC CARDEROCK DIV
R PETERSON CODE 2120
M MILLER CODE 2120
9500 MACARTHUR BLVD
WEST BETHESDA MD 20817-5700

1 OFC OF NAVAL RSCH
J BRADEL
875 N RANDOLPH ST
SUITE 1425
ARLINGTON VA 22203-1995

2 CERADYNE INC
M NORMANDIA
J SHIH
3169 RED HILL AVE
COSTA MESA CA 92626

NO. OF
COPIES ORGANIZATION

1 OUSD(AT&L) DEFENSE SYS
LAND WARFARE AND MUNITIONS
D BAUM
THE PENTAGON SUITE 3B1060
WASHINGTON DC 20301-3090

1 ARMOR WORKS
W PERCIBALLI
1701 W 10TH ST SUITE 5
TEMPE AZ 85281

1 APPLIED RSCH ASSO INC
J YATTEAU
5941 S MIDDLEFIELD RD SUITE 100
LITTLETON CO 80123

1 NATIONAL INST OF STANDARDS
AND TECHNOLOGY CERAMICS DIV
BLDG 223
G QUINN (STOP 8529)
GAITHERSBURG MD 20899

ABERDEEN PROVING GROUND

116 DIR USARL
AMSRD ARL CI HC
D GROVE
AMSRD ARL SL BB
A DIETRICH
M ENDERLEIN
P FEDELE
E HUNT
S JUARASCIO
J PLOSKONKA
J ROBERTSON
AMSRD ARL SL BE
W BRUCHEY
L P SCOTT
AMSRD ARL WM B
R COATES
J NEWILL
M ZOLTOSKI
AMSRD ARL WM BC
M BUNDY
AMSRD ARL WM M
J MCCAULEY
S MCKNIGHT
AMSRD ARL WM MA
C HUBBARD
P MOY
S TREVINO
AMSRD ARL WM MB
T BOGETTI
W DE ROSSET

NO. OF
COPIES ORGANIZATION

L KECSKES
J SWAB
M STAKER
AMSRD ARL WM MC
R ADLER
D GRANVILLE
AMSRD ARL WM MD
J ADAMS
B CHEESEMAN
E CHIN
J CHINELLA
P DEHMER
D DOHERTY
G GAZONAS
G GILDE
W GREEN
J LASALVIA
M MOTYKA
P PATEL
W ROY
B SCOTT
S WALSH
J WINTER
S WOLF
AMSRD ARL WM T
B BURNS
A CARDAMONE
D HACKBARTH
T WRIGHT
AMSRD ARL WM TA
P BARTKOWSKI
M BURKINS
B DONEY
G FILBEY
R FREY
W GILLICH
N GNIAZDOWSKI
W GOOCH
T HAVEL
C HOPPEL
E HORWATH
T JONES
M KEELE
D KLEPONIS
C KRAUTHAUSER
B LEAVY
S MARTIN
W ROWE
J RUNYEON
N RUPERT
D RUSIN
S SCHOENFELD
D SHOWALTER
G SILSBY

NO. OF COPIES ORGANIZATION

A STANDIFORD
K STOFFEL
AMSRD ARL WM TB
P BAKER
R SKAGGS
AMSRD ARL WM TC
J BARB
T FARRAND
M FERMEN-COKER
E KENNEDY
K KIMSEY
L MAGNESS
R MUDD
D SCHEFFLER
S SCHRAML
B SCHUSTER
B SORENSEN
R SUMMERS
W WALTERS
C WILLIAMS
AMSRD ARL WM TD
S BILYK
T BJERKE
M BLOUNT
D CASEM
J CLAYTON
D DANDEKAR
M GREENFIELD
Y HAUNG
K IYER
B LOVE
H MEYER
M RAFTENBERG
E RAPACKI (5 CPS)
M SCHEIDLER
S SEGLETES
T WEERASOORIYA
AMSRD ARL WM TE
P BERNING
C HUMMER
T KOTTKE
A NIILER
J POWELL
B RINGERS
G THOMSON

NO. OF COPIES ORGANIZATION

1 DIRECTOR
USARL
EUROPEAN RSCH OFC
AMSRD ARL RO ER
S SAMPATH
PSC 802 BOX 15
FPO AE 09499-1500

1 ADVANCED MTRLS LAB
NATIONAL INST FOR MTRLS SCI
T SEKINE
1-1 NAMIKI
TSUKUBA 305-0044
JAPAN

3 CAVENDISH LAB
PHYSICS AND CHEMISTRY
OF SOLIDS
J E FIELD
W G PROUD
K TSEMBELIS
MADINGLEY RD
CAMBRIDGE CB3 0HE
UNITED KINGDOM

2 RAFAEL BALLISTICS CTR
R MAYSLES
Z ROSENBERG
PO BOX 2250
HAIFA ISRAEL

1 ROYAL MILITARY COLLEGE
OF SCIENCE CRANFIELD UNIV
J MILLETT
SHRIVENHAM SWINDON
WILTSHIRE SN6 8LA
UNITED KINGDOM

1 KUMAMOTO UNIV
SHOCK WAVE AND CONDENSED
MATTER RSCH CTR
T MASHIMO
KUMAMOTO 860-8555
JAPAN

4 FRENCH-GERMAN RSCH INST OF
ST LOUIS (ISL)
P Y CHANTERET
H J ERNST
T MERKEL
V SCHIRM
PO BOX 34 F-68301
SAINT LOUIS FRANCE

NO. OF COPIES ORGANIZATION

2 DEFENCE SCIENCE AND
TECHNOLOGIES LAB (DSTL)
B JAMES
I PICKUP
CHOBHAM LANE
CHERTSEY SURREY KT 16 0EE
UNITED KINGDOM

3 ETABLISSEMENT TECHNIQUE
DE BOURGES
P BARNIER
B GAILLY
P F PERON
ROUTE DE GUERRY
18021 BOURGES CEDEX
FRANCE

2 RUAG LAND SYSTEMS
W LANZ
W ODERMATT
ALLMENDSTRASSE 86
CH 3602 THUN
SWITZERLAND

3 FRANTSEVICH INST FOR PROBLEMS
IN MATERIALS SCIENCE
NATIONAL ACADEMY OF SCIENCES
OF UKRAINE
B A GALANOV
V KARTUZOV
Y MILMAN
3 KRZHYZHANOVSKY ST
KYIV 03142
UKRAINE

7 FRAUNHOFER INSTITUT FUR
KURZEITDYNAMIK
ERNST MACH INSTITUT (EMI)
V HOHLER
B LEXOW
E STRASSBURGER
K THOMA
K WEBER
M WICKERT
M WICKLEIN
ECKERSTRASSE 4
D 7800 FREIBURG 1 BR 791 4
GERMANY

1 UNIVERSITY OF MANCHESTER
N BOURNE
MANCHESTER M60 1QD
UNITED KINGDOM

NO. OF COPIES ORGANIZATION

6 SWEDISH DEFENCE RSCH AGNCY
(FOI) WEAPONS AND PROTECTION
L HOLMBERG
E LIDEN
P LUNDBERG
R RENSTROM
P SKOGLUND
L WESTERLING
GRINDSJÖN
SE 147 25 TUMBA
SWEDEN

2 INSTITUTE FOR HIGH ENERGY
DENSITIES OF RUSSIAN
ACADEMY OF SCIENCES
G I KANEL
V E FORTOV
IZHORSKAYA 13/19
MOSCOW 125412
RUSSIA

1 KOREA ADVANCED INSTITUTE
OF SCIENCE AND TECHNOLOGY
DEPT OF MATERIALS SCIENCE AND
ENGINEERING
D K KIM
TAEJON
KOREA

1 DSTO AERONAUTICAL AND
MARITIME RSCH LAB
AMRL
S CIMPOERU
PO BOX 4331
MELBOURNE 3001
AUSTRALIA

1 SPART DIRECTION BP 19
E WARINGHEM
10 PLACE GEORGES CLEMENCEAU
92211 SAINT CLOUD CEDEX
FRANCE

1 BUNDESAMT FUR WEHRTECHNIK
UND BESCHAFFUNG K1 1
R QUIDDE
FERDINAND SAUERBRUCH
STRASSE 1
56073 KOBLENZ
GERMANY

NO. OF COPIES ORGANIZATION

2 UNIV OF CHEMNITZ
L MEYER
F PURSCHE
ERFENSCHLAGER STRASSE 73
09125 CHEMNITZ
GERMANY

1 EADS LFK
LENKFLUGKÖRPERSYSTEME
GMBH
M HELD
HAGENAUER FORST 27
86529 SCHROBENHAUSEN
GERMANY

1 DEFENCE RSCH ESTABLISHMENT
VALCARTIER ARMAMENTS DIV
R DELAGRAVE
2459 PIE XI BLVD N
PO BOX 8800
CORCELETTE
QUEBEC GOA 1R0
CANADA

1 INSTITUTE FOR PROBLEMS
OF STRENGTH
G STEPANOV
TIMIRYAZEVSKAYA STR 2
252014 KIEV
UKRAINE

2 CENTRE D'ETUDES GRAMAT
J CAGNOUX
J Y TRANCHET
46500 GRAMAT
FRANCE

INTENTIONALLY LEFT BLANK.